2016

Los Alamos Space Weather Summer School Research Reports

Misa M. Cowee *(Editor)*

Cover image: NASA image of the aurora taken by the Expedition 29 crew aboard the International Space Station (http://visibleearth.nasa.gov)

2016

Los Alamos Space Weather Summer School Research Reports

Misa M. Cowee *(Editor)*

2016

Los Alamos Space Weather Summer School
Research Reports

Preface

The sixth Los Alamos Space Weather Summer School was held June 6th – July 29th, 2016, at Los Alamos National Laboratory (LANL). With renewed support from the Center for Space and Earth Sciences (CSES), formerly the Institute of Geophysics, Planetary Physics, and Signatures (IGPPS), we hosted a new class of eight students from various U.S. and foreign research institutions. The summer school curriculum includes a series of structured lectures as well as mentored research and practicum opportunities. Lecture topics including general and specialized topics in the field of space weather were given by a number of researchers affiliated with LANL. This year's summer school included a short-course on the Autoplot software package.

Students were given the opportunity to engage in research projects through a mentored practicum experience. Each student works with one or more LANL-affiliated mentors to execute a collaborative research project, typically linked with a larger on-going research effort at LANL and/or the student's PhD thesis research. This model provides a valuable learning experience for the student while developing the opportunity for future collaboration.

This report includes a summary of the research efforts fostered and facilitated by the Space Weather Summer School. These reports should be viewed as work-in-progress as the short session typically only offers sufficient time for preliminary results. At the close of the summer school session, students present a summary of their research efforts.

It has been a pleasure for me to serve again as the director of the Los Alamos Space Weather Summer School. I am very proud of the work done by the students, mentors and lecturers—your dedicated effort and professionalism are key to a successful program. I am grateful for all the administrative and logistical help I have received in organizing the program.

Los Alamos, NM
November 2016

Dr. Misa Cowee
Summer School Director

2016

Los Alamos Space Weather Summer School
Research Reports

New students

Shantanab Debchoudhury	*Virginia Polytechnic Institute and State University*
Rosie Hood	*University College London, UK*
Lilla Juhász	*Eötvös Loránd University, Hungary*
Oleksandr Koshkarov	*University of Saskatchewan, Canada*
Vivien Loridan	*École normale supérieure de Cachan, France*
Anthony Saikin	*University of New Hampshire*
Yuguang Tong	*University of California Berkeley*
Kateryna Yakymenko	*University of Saskatchewan, Canada*

2016

Los Alamos Space Weather Summer School
Research Reports

Project Reports

2016

Los Alamos Space Weather Summer School
Research Reports

2016

Los Alamos Space Weather Summer School
Research Reports

Pictures

Class of 2016 Students and Mentors
(Students indicated in bold. Left to right, back row: ***Kateryna Yakymenko****,* ***Oleksandr Koshkarov****, Jesse Woodroffe,* ***Rosie Hood****,* ***Vivien Loridan****, Reiner Friedel, Greg Cunningham, John Steinberg; middle row: Lynea Koshar,* ***Lilla Juhász****,* ***Yuguang Tong****; front row:* ***Shantanab Debchoudhury****,* ***Anthony Saikin****, Erin Lay, Mary Wubbena, Vania Jordanova, Misa Cowee. Not pictured: Joe Borovsky, Gian Luca Delzanno, Steve Morley.*

2016

Los Alamos Space Weather Summer School
Research Reports

Lectures

- Introduction to the Magnetosphere ..... *Joe Borovsky*
- Introduction to the Solar Wind ..... *Joe Borovsky*
- Solar Eruptive Events and the Acceleration of High-Energy Particles ..... *Tom Vestrand*
- Autoplot Short Course ..... *Jeremy Faden*
- Introduction to the Ionosphere ..... *Erin Lay*
- History of the Term 'Space Weather' ..... *Trey Cade*
- Introduction to Detectors for High Energy Particles, X-rays, and Gamma rays ..... *Richard Schirato*
- Magnetosphere-Ionosphere Coupling ..... *Yiqun Yu*
- Adiabatic particle motion, Drift shells, and Radiation belt ..... *Mike Henderson*
- Geomagnetic Storms, Ring Current, and Plasmasphere ..... *Vania Jordanova*
- Overview of LANL's Space Program and National Security Mission ..... *Brian Larsen*
- Kinetic Plasma Instabilities ..... *Peter Gary*
- Data Assimilation ..... *Humberto Godinez*
- Electromagnetic Waves ..... *Max Light*
- PIC Simulation Technique ..... *Xiangrong Fu*
- Radiation Belt Diffusion ..... *Greg Cunningham*
- The Earth's Plasma Sheet ..... *Mick Denton*
- Energetic Electron Pitch-Angle Distributions in the Radiation Belts: Pitfalls ..... *Reiner Friedel*
- Introduction to Magnetic Reconnection ..... *Ari Le*
- NASA Genesis Mission: Search for Origins ..... *Fan Guo*

2016

Los Alamos Space Weather Summer School
Research Reports

Sponsors

- Center for Space and Earth Sciences (CSES) at LANL [formerly the Institute of Geophysics, Planetary Physics, and Signatures (IGPPS)]

Contact Information

Dr. Misa Cowee
Los Alamos Space Weather Summer School
P.O. Box 1663, MS D466
Los Alamos National Lab, NM 87545

http://www.swx-school.lanl.gov/

Publication Release

LA-UR 16-29471

Spatio-temporal fluctuations in GPS TEC data to estimate length scales of ionospheric perturbations

Shantanab Debchoudhury

Virginia Polytechnic Institute and State University, Blacksburg, VA 24061.

Erin H. Lay

Los Alamos National Laboratory, Los Alamos, NM 87545

Peter Parker

Los Alamos National Laboratory, Los Alamos, NM 87545

Max Light

Los Alamos National Laboratory, Los Alamos, NM 87545

Abstract

Irregularities in the ionosphere can cause radio waves to scintillate resulting in degradation of signal quality. Proper estimation of the length scales of these perturbations can help understand the magnitude and characterization of scintillation. Conventional power spectra models for length scales have been used to develop scintillation models. In this project, we make use of total electron content (TEC) data from dual-frequency Global Positioning System (GPS) satellites to measure the spatial spectrum scales of ionospheric fluctuations. High frequency GPS data (15sec) have been obtained from dense GPS receiver networks in the mid-latitude PBO network in California region for a given day of high geomagnetic activity. The processed data reveal time-varying fluctuations in the kilometer scales of interest and provide a test case for the broader problem of estimating the scales which affect scintillation.

Keywords: GPS TEC, scintillation, ionosphere perturbations

1. Introduction

Rapid amplitude and phase fluctuations in a received radio wave [Hey et al., 1982; Aarons and Basu, 1994] are termed ”scintillation”. Small-scale variations in electron density changes the refractive index of the medium causing scintillation of passing radio waves. The very dynamic low-latitude ionosphere plays a prominent role in scintillation with phenomena like equatorial spread-F (ESF) contributing to plasma density depletions over varying scale length regimes [Anderson and Haerendel, 1979; Aarons et al., 1983; Basu et al., 2001]. Individual patches of irregularities with short lifespan may even disrupt radio wave propagation for hours. Fluctuations in Total Electron Content (TEC) measurements from navigation systems like the Global Positioning System (GPS) play a key role in studying the irregularities in the ionosphere that cause degradation of radio wave signal quality. TEC [Ya'acob et al., 2010] is given by integrating the electron density along a unit square-meter column along a transmission path from the receiver to the satellite.

$$TEC = \int_S^R N_e dl \tag{1}$$

Email addresses: sdch10@vt.edu (Shantanab Debchoudhury), elay@lanl.gov (Erin H. Lay), Peter.parker@lanl.gov (Peter Parker), mlight@lanl.gov (Max Light)

where N_e is the local electron density, S and R respectively are the satellite and the receiver.

TEC measurements over a dense regional network offer a validation of power-law estimate models of spatial scale spectral densities that have been widely used to study scintillation [Rino et al.; Rino, 1979; Singleton, 1974]. Previous works have used TEC measurements to study the ionospheric fluctuations occurring due to geomagnetic and atmospheric forcing varying over different time and length scales. In particular ionospheric effects of geomagnetic storms have been studied in detail with GPS TEC data since such events induce patches of irregularities that cause scintillation [Thomas, 2016].

2. Purpose of our study

In this work, our primary objective is to use GPS TEC measurements to make a better empirical estimation of scintillation scale sizes. Data from a high density cluster of GPS receivers are used for this purpose. In order to study scintillation scale sizes, data from these receivers are collected for a day of geomagnetic storm since these storms are known to cause spatial and temporal variations in electron density structures. The ionosphere, for this purpose, is generally modeled as a thin uniform horizontal layer at an altitude of 350 km, where the electron density is at its peak in the F-region. The intersection of the line of sight joining the receiver and the satellite intersects this thin ionospheric shell at the Ionospheric Pierce Point (IPP). Incident radio wave suffer delay in phase and degradation in amplitude at this layer due to small scale variations in density structures and thereby affects communication systems which make use of the positioning system.

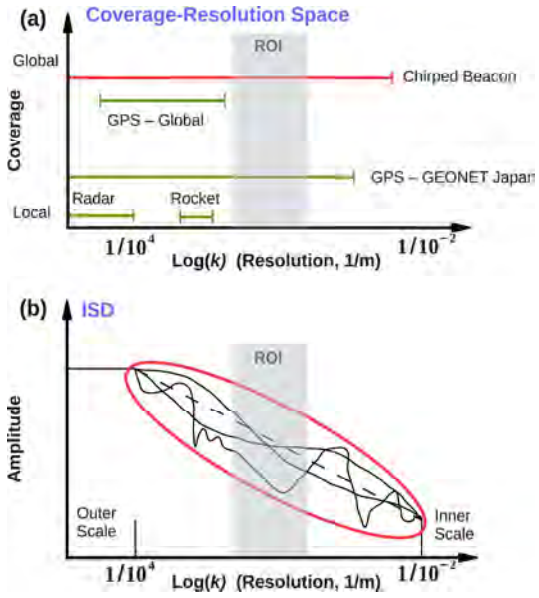

Figure 1: Spatial resolution associated with the region of interest (ROI) and associated coverage plots (a) of different systems and amplitude (b) degradation of signal

Figure 1 describes the range of length scales of density fluctuations that we are interested in for this problem in general. In Figure 1(a) the coverage of different systems is plotted against resolution. The region of interest is highlighted and the desired resolution is in the order of 10s of kilometers. The figure shows that radars and sounding rockets have regional coverage and resolution. Global GPS, on the other hand, has more global coverage albeit at low spatial resolution. Thus only dense regional systems like the Earth observation network at Japan (GEONET) [Imakiire and Nakahori, 2001] can provide the desired resolution. Chirped beacon is a proposed LEO satellite alternative which has a greater coverage and resolution. The irregularity spectral density (ISD) shows the power spectrum of density fluctuations as a function of spatial size. Typically, a power law estimate is used for the ISD (dashed line, Figure 1(b)), but the goal of this study is to provide an empirical measurement of the spectral shape which most likely does

not follow a true power law (random solid lines in Figure 1(b) show hypothetical empirical spectra). This is shown in Figure 1(b) where the amplitude is plotted against logarithmic spatial resolution.

3. Approach

3.1. Data Processing

Total electron content (TEC) measurements are obtained from dual frequency GPS signals. Pseudoranges P_1 and P_2 are used to calculate TEC as shown below

$$P_1 - P_2 = 40.3TEC(\frac{1}{f_1^2} - \frac{1}{f_2^2}) \tag{2}$$

where f_1 and f_2 correspond to the L1 and L2 frequencies at 1.23GHz and 1.58GHz respectively. The TEC data derived from pseudorange calculations although accurate suffer from lack of precision due to timing uncertainty. Thus the pseudorange data is generally used to level the carrier phase differential measurements which are more precise and less accurate.

TEC observations from a range of satellites are collected as recorded by a group of closely located ground based receivers. The many observation lines of sight give an ionospheric snapshot for every time instance as shown in Figure 2. The ionospheric pierce point (IPP) is assumed to be at 350 km.

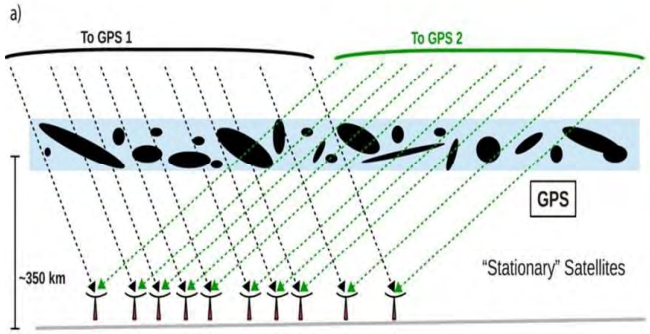

Figure 2: TEC observations as recorded from "stationary satellites" at a given time. Black shapes represnt electron density fluctuations in the ionosphere.

Thus for sufficiently dense data, the differential TEC measurements measure ionospheric irregularities with spatial resolution at the length scales on the order of the receiver spacing.

The TEC data from differential phase measurements are uncalibrated and along a slant column (slant TEC or sTEC) and thus need to be leveled to get better accuracy. However, our objective is to observe the differential variation in TEC observations and thus the use of this uncalibrated sTEC data from phase differential measurements is sufficient for our purpose. The process flow includes selecting a cluster of receivers located within a short geographical expanse. A certain day is selected with known geomagnetic activity sufficient to produce the irregularities of interest. Ideally all the receivers have GPS observations from the satellites on that day. The phase differential data is now processed for each station within the network chosen. The available data, however, suffers from contamination which should be eliminated before further processing. A major source of contamination is the effect due to multipath and thus below a certain elevation angle of the satellite with respect to the receiver when these effects become very prominent, it is practically infeasible to interpret the data correctly. Also severe scintillation causes cycle slips resulting from losses of phase lock. The multipath effects are removed by setting a threshold on the satellite elevation angle with respect to the receiver. In other words, whenever the elevation angle goes down below the threshold (chosen to be 30 degrees for this step of processing), the section of data is rejected for the chosen day. Similarly the data points for a satellite-receiver pair, in which cycle slips are observed to have occurred, are not considered for further processing. Thus we end up with discontinuous chunks of available sTEC data for every satellite-receiver pair for a given day.

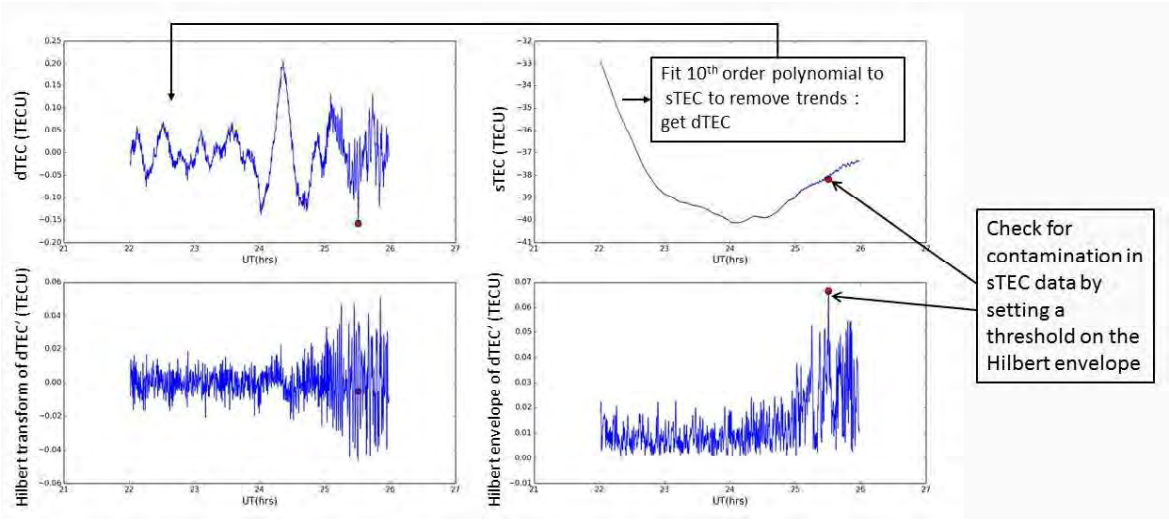

Figure 3: Steps to obtain a continuous arc of quality-controlled data after initial level of processing. From top right in anti-clockwise direction, sTEC is detrended to obtain differential TEC (dTEC). The dTEC arc is processed to identify any irregular gradient (contamination) through Hilbert transformation of the derivative. Data points where the envelope exceeds a threshold are contaminated and hence not usable.

Figure 3 describes the next steps in the data processing routine. In the time periods of interest within the selected day (usually a few hours), we select the available continuous chunk of sTEC data for a satellite-receiver pair (shown in the top right of Figure 3). Provided we have sufficient samples of data within this time window, we remove the long term trends associated with this arc. This is implemented by fitting a tenth order polynomial to the sTEC arc and obtaining the deviation as a function of time. This is shown in the top left of Figure 3. We call this obtained detrended sTEC data as differential TEC (dTEC). Irregular gradients may be present in the sTEC data which are manifested by sudden jumps in the dTEC data (red sample dots in Figure 3). These contaminations are mostly results of erroneous measurements by the receiver and thus pass through the previous checks of multipath and cycle slips. Thus, the obtained dTEC profile is scrutinized to remove contamination. For this purpose, we identify the regions of sudden jumps by implementing a Hilbert transformation on the gradient of the dTEC arc. The result is shown in the left bottom of Figure 3 and the right bottom of the figure shows the envelope corresponding to this arc. Any point on this latter envelope which exceeds a threshold (chosen to be 0.06) is a potentially contaminated data point where the sTEC and hence the dTEC data deviates from the general profile. A continuous arc is selected by avoiding these data points encompassing as much of the time window as possible. The process is repeated for the data from all the receivers in the network for the chosen time window.

Once quality is ensured, the subsequent step is to obtain a spatio-temporal map of the dTEC observations at the IPP point (350 km). This is obtained by assembling all the calculated dTEC values for a time period of interest for all the receivers looking at a particular satellite. Due to the quality control measures implemented, the data within the broad time frame may be unequal in length for each receiver. However, it is desirable that a sufficiently high number of data samples are still available for a large duration of time (usually a few hours). A 2-D spatial FFT is performed to observe the wave amplitudes and frequencies within the spatial domain and how these irregularities propagate in time. This essentially corresponds to the spectrum that is needed as input to a scintillation model as the ISD.

3.2. Dataset used

As a test case for this study, a group of about 363 stations in the PBO network in the mid-latitude California-Nevada-Arizona region in western United States has been considered. The receivers span a radius of 500 km and offer high rate of 15sec which is useful to capture the small duration fluctuations in the ionosphere. The average distance between all the pairs of stations within this dense network is ideal to capture the small scale variations and irregularities in each ionospheric snapshot.

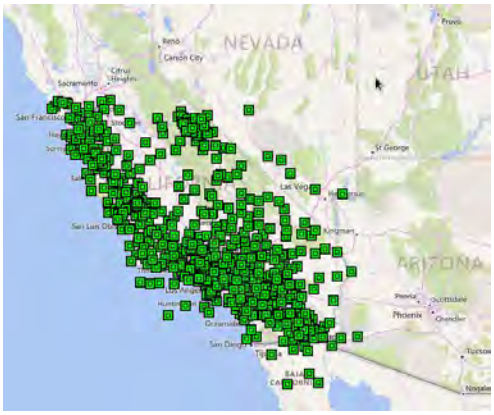

Figure 4: Test case receivers used in the study

GPS TEC data are obtained from RINEX files (Receiver Independent Network Exchange) corresponding to a particular day for these stations. The day of interest has been chosen to be that of the Mother's Day storm in 2016 (May 8-9) when significantly high kp values were observed. The local time window chosen is 15:30 to 18:25 (22:30 UT - 1:25 UT) when the storm activity was high, as shown in the plot of kp vs. time in Figure 5.

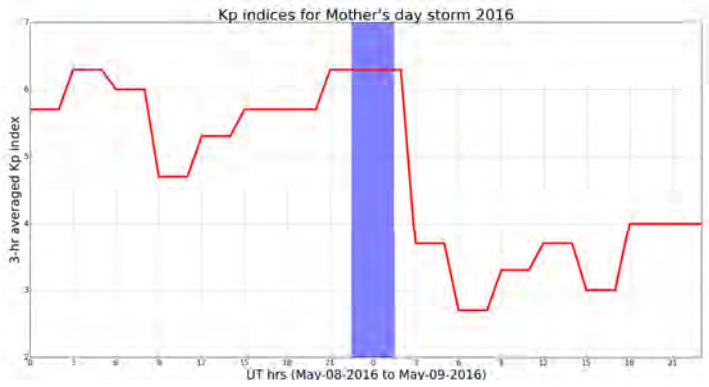

Figure 5: 3-hour averaged Kp index corresponding to the time window chosen for the study (22:30 UT - 1:25 UT) on Mother's Day storm 2016

4. Results

The results from the test study are presented in this section. Figure 6 shows fluctuations in dTEC data for a sample set of 20 stations that were selected for analysis. After processing and quality control data only remained from 10 of these stations.

The fluctuations in TEC data show waves of varying frequencies which indicate perturbations in the ionosphere. Figure 6 however is only depicting temporal fluctuations of dTEC for a subset of the entire set of stations for which data has been processed. A better understanding of the dynamics of the ionosphere is obtained if we look at the spatial scales associated with each temporal snapshot. For this we perform the 2-D FFT of the processed and quality controlled dTEC data for all the receivers looking at a particular satellite at different time points.

Figures 7(a) to 7(f) show the evolution of the waves of different spatial frequencies with time. Each figure of a given time snapshot has two panels. The one on the right is a plot of the dTEC values recorded by the stations on a

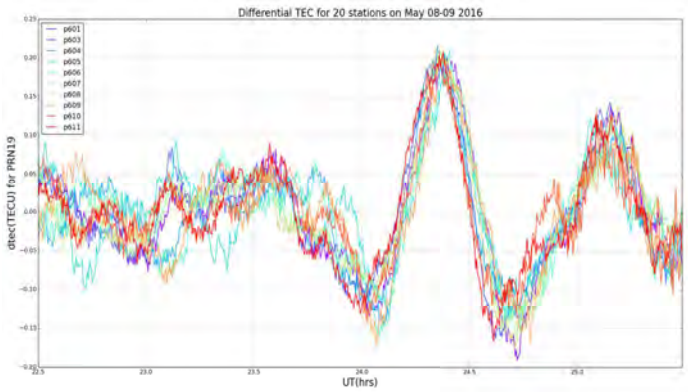

Figure 6: Differential TEC for a subset of stations in PBO network obtained from GPS satellite PRN19

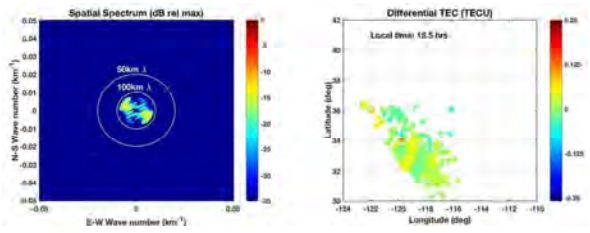

(a) Spatial spectrum at 15:30 LT

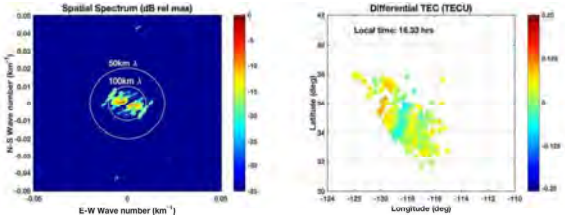

(b) Spatial spectrum at 16:20 LT

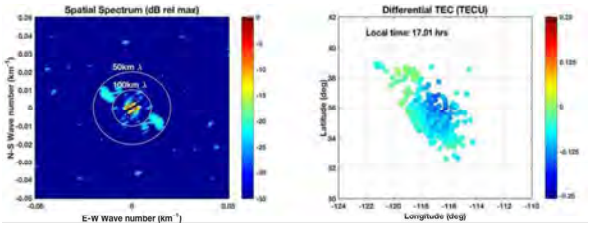

(c) Spatial spectrum at 17:00 LT

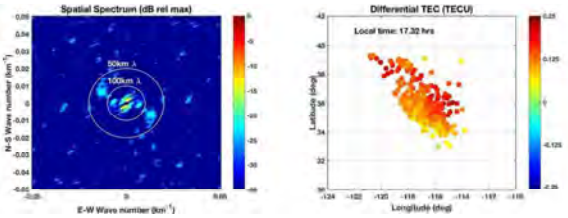

(d) Spatial spectrum at 17:20 LT

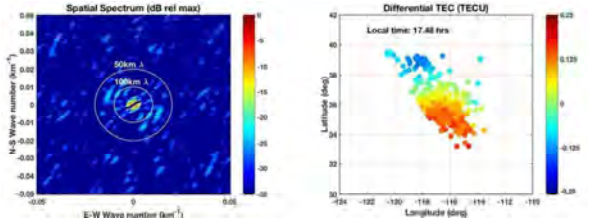

(e) Spatial spectrum at 17:29 LT

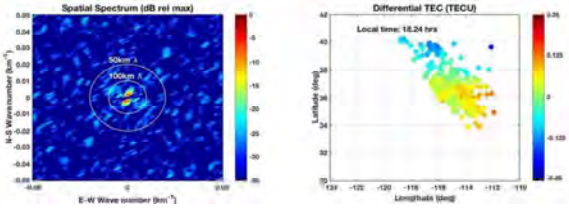

(f) Spatial spectrum at 18:15 LT

Figure 7: (a) to (f) shows temporal variations of the spatial spectrum (left) corresponding to the dTEC data (right) for 363 PBO stations on Mother's Day storm 2016. The spatial spectra are shown as function of the horizontal and vertical wave numbers.

latitude-longitude grid at the IPP (350 km) where the color of the point is a measure of the dTEC value for a station in TECU (1×10^{16} el/m^2). The panel on the left is a 2-D spatial DFT of the dTEC values for all the stations at the given time point, which gives the associated frequencies and amplitudes of the waves in the system. The E-W wave number is plotted on the horizontal axis while the N-S wave number is given in the vertical axis, both in km^{-1} units. The color of the spectrum indicates the amplitude (in dB) of the wave relative to the maximum observed in the entire time window of study. Thus the colorbar for both the panels is fixed for all the temporal snapshots. The spectrogram also shows, in two concentric circles, the associated wavelengths of 50 km (outer circle with larger radius) and 100 km (inner circle with smaller radius) as a measure of reference. Therefore, features inside the innermost circle have scale sizes larger than 100 km, and features outside the outer circle have scale sizes smaller than 50 km.The entire space in the spectrogram shows a maximum resolution of 1 km in both E-W and N-S directions. For the region of interest for this project, we are interested in scale sizes on the tens of kilometers to kilometers, which is the regime in Figure 7 starting between the two while circles, and extending to the outer edges of the plot.

Figure 7(a) shows the presence of low amplitude waves with spatial wavelengths more than 100 km. About an hour later around 16:20 LT (Figure 7(b) we see higher amplitude perturbations that span smaller spatial scales. However around 17:00 LT - 17:30 LT (Figures 7(c) - 7(e)) the associated amplitude increases rapidly and the wave spans few hundreds of kilometers in wavelengths. These very low frequency components correspond to the dTEC peak observed from Figure 6 around 24:15 UT (17:20 LT). Ionospheric disturbances are known to take a few hours to propagate to the mid-latitudes. Thus the sudden disturbances hint at possible storm injection in the polar regions that propagate to the mid-latitude California region which give rise to these irregularities in the wave pattern. The high kp value around this time as indicated by Figure 5 corroborates this theory and the rapid increment of spatial wave amplitudes is likely to be a manifestation of the storm onset around these latitudes. In Figure 7(f) the spatial structures are smaller than those immediately after the storm injection (Figure 7(e)), but still larger than 100 km. In other words, the irregularity is still is within the 100 km innermost circle, but closer to its boundary.

5. Conclusions and future works

The study focuses on processing TEC data from a dense cluster of GPS receivers and how the same can be used to study temporal variations of spatial irregularities in the ionosphere. The small scale variations affect scintillation of radio waves and the results show that TEC data can measure irregularities up to length scales of 10s of kilometers. The empirical spectrum obtained can be used as an input of a scintillation model which is the next step of our work. Further investigations need to be performed to analyse more datasets like the Japanese GPS network GEONET on St. Patrick's Day storm. A major challenge remains in identifying networks of sufficient high density and data rates with data available throughout for a given day. More future endeavors include implementing leveling procedures to calibrate the TEC data to greater accuracies which may improve the understanding and interpretation of the results in general.

REFERENCES

Aarons, J., Basu, S., 1994. Ionospheric amplitude and phase fluctuations at the gps frequencies, in: ION GPS-94, pp. 1569–1578.

Aarons, J., Klobuchar, J., Whitney, H., Austen, J., Johnson, A., Rino, C., 1983. Gigahertz scintillations associated with equatorial patches. Radio science 18, 421–434.

Anderson, D., Haerendel, G., 1979. The motion of depleted plasma regions in the equatorial ionosphere. Journal of Geophysical Research: Space Physics 84, 4251–4256.

Basu, S., Basu, S., Valladares, C., Yeh, H.C., Su, S.Y., MacKenzie, E., Sultan, P., Aarons, J., Rich, F., Doherty, P., et al., 2001. Ionospheric effects of major magnetic storms during the international space weather period of september and october 1999: Gps observations, vhf/uhf scintillations, and in situ density structures at middle and equatorial latitudes. Journal of Geophysical Research: Space Physics 106, 30389–30413.

Hey, J., Parsons, S., Phillips, J., 1982. 1946, fluctuations in cosmic radiation at radio-frequencies. Classics in Radio Astronomy 1, 228.

Imakiire, T., Nakahori, Y., 2001. 1gps earth observation network (geonet) of japan .

Rino, C., 1979. A power law phase screen model for ionospheric scintillation: 1. weak scatter. Radio Science 14, 1135–1145.

Rino, C.L., Carrano, C.S., Groves, K.M., Roddy, P., . Reconciling two# component power spectra .

Singleton, D., 1974. Power spectra of ionospheric scintillations. Journal of Atmospheric and Terrestrial Physics 36, 113–133.

Thomas, E.G., 2016. Morphology and dynamics of storm-time ionospheric density structures .

Ya'acob, N., Ismail, M., Abdullah, M., 2010. GPS total electron content (TEC) prediction at ionosphere layer over the Equatorial region. INTECH Open Access Publisher.

Understanding and Assessing the Effects of Geomagnetic Preconditioning on the Severity of Ground-Level Geomagnetic Disturbances during the 22-29 July 2004 Geomagnetic Storm

Rosie Hood

University College London, Gower St, London WC1E 6BT, UK

Jesse Woodroffe

Los Alamos National Laboratory, Los Alamos, New Mexico, 87545, USA

Steve Morley

Los Alamos National Laboratory, Los Alamos, New Mexico, 87545, USA

Abstract

The 22-29 July 2004 geomagnetic storm resulted in ground-level geomagnetic disturbances (GMDs) twice the magnitude of previous storms of similar Dst intensities. Here the state of the magnetosphere and its corresponding influence on the ground via field-aligned currents (FACs) is assessed using the CHAllenging Mini-satellite Payload (CHAMP) fluxgate magnetometer to derive the latter and magnetospheric indices to infer the former. Several relations are realised, including a strong correlation between dayside FAC magnetic latitudes and IMF Bz, corresponding to magnetopause reconnection, as well as trends with the Sym-H and Auroral Electrojet indices. The most equatorward FACs occur on the nightside and are shown to depend on storm intensity as defined by the Sym-H index. Finally, time lags, representative of propagation and response, are introduced to the indices to improve correlations.

Keywords: ground-level GMDs, geomagnetic storms, field-aligned currents, CHAMP

1. Introduction and Motivation

Space weather is one of the most significant natural hazards of the 21st century, posing a risk to both space and ground infrastructure and modern day civilisation as we know it (see for example: National Research Council (2008); Royal Academy of Engineering (2013). A key part of this vulnerability are ground effects, where long man-made framework such as gas pipelines and wiring used in the electrical grid system can conduct induced ground currents during geomagnetic storms causing pipelines to crack and transformers to overload and melt (Viljanen et al., 2014; Lloyds, 2013). The impact of such ground geomagnetic disturbances (GMDs) can be fatal and financially damaging; an example of the latter is the Quebec power grid failure in 1989 resulting in a 9-hour blackout and $2 billion of estimated losses (Riswadkar and Dobbins, 2010). It is therefore vital that the ground effects of geomagnetic storms and their role in space weather are well-understood.

Four geomagnetic storms in 1986, 1991, 1992 and 2004 all had similar values of minimum Dst, an indication of the storm intensity, but the latter event produced ground GMDs twice the magnitude of the others. A notable difference between these events is the location of the minimum Dst (or Sym-H) intensity during each multi-dip storm, defined as a storm where Dst decreases several times over an interval of a few days. Of these four storms, only the 2004 event was comprised of storms of increasing intensity. By assessing the state of the magnetosphere we hope to

Email addresses: rosie.hood.13@ucl.ac.uk (Rosie Hood), jwoodroffe@lanl.gov (Jesse Woodroffe), smorley@lanl.gov (Steve Morley)

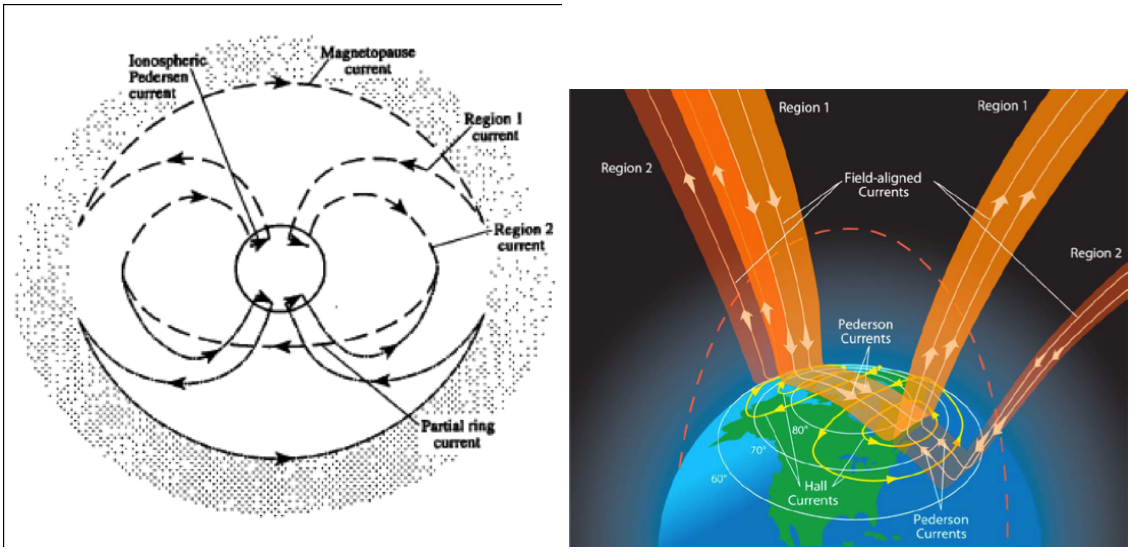

(a) (b)

Figure 1: FACs defined in the (a) Magnetospheric system (Cowley, 2013), and (b) Ionospheric current system (credit: AGU).

explain this behaviour and its role in dictating the severity of GMDs; for example the 2004 storm was a result of three sequential coronal mass ejections (CMEs) (Zhang et al., 2007) which may have preconditioned the magnetosphere to drive larger GMDs in comparison to the other storms. For the purposes of this report we focus on comparing the three individual storms within the period of July 2004 to assess the significance of a sequence and its potential for preconditioning the magnetosphere. To do this, we looked at indices indicative of the solar wind and magnetosphere configuration of the July 2004 storm, and therefore markers of this preconditioning, and compared this to the location and magnitude of the field-aligned currents (FACs) generating the ionospheric currents and, in turn, the ground GMDs, where magnitude indicates the magnitude of this driver and location how effective it is. The FACs were calculated using the CHAllenging Mini-satellite Payload (CHAMP) magnetic field data, as outlined in Wang et al. (2006) and in Section 2 of this report.

1.1. Current systems: GMDs and FACs

GMDs are part of a complex global and magnetospheric current system, and can be driven by several sources such as the ring current, electrojets and Chapman-Ferraro currents on the magnetopause. Here we outline their generation via FACs (this has been observed, see for example Kamide (1982)), which is the focus of this report. Initially the system is driven by currents in the magnetosphere arising from the IMF or solar wind, for example, which then flow along geomagnetic field lines (as shown in Figure 1(a) by Region 1) into the ionosphere as FAC sheets (as illustrated in Figure 1(b); see for example Cowley (2013)). As the currents are fed into the ionosphere they close via a Pedersen current and induce a Hall current, and it is these currents that are responsible for generating ground fluctuations in dB inducing the ground GMDs harmful to the electrical grid and gas industries.

As mentioned previously, we are concerned with the FAC magnitude, but its location is also significant - as you move away from the poles the Pedersen currents are less effective at cancelling out the FACs (for further discussion see Fukushima (1976)), therefore the more equatorward the latitude the more likely it is to generate severe ground GMDs. Low altitude satellites can pass through the FAC current sheets and sample the magnetic field from which its magnitude and location can de derived; this methodology is outlined in Section 2.

2. Data Analysis

CHAMP was a German satellite spanning the years 2000-2010, in a near-polar (inclination=87 °) orbit with an initial altitude of 454km (GFZ, 2009), and aimed at recording high precision atmospheric and geophysical data. In

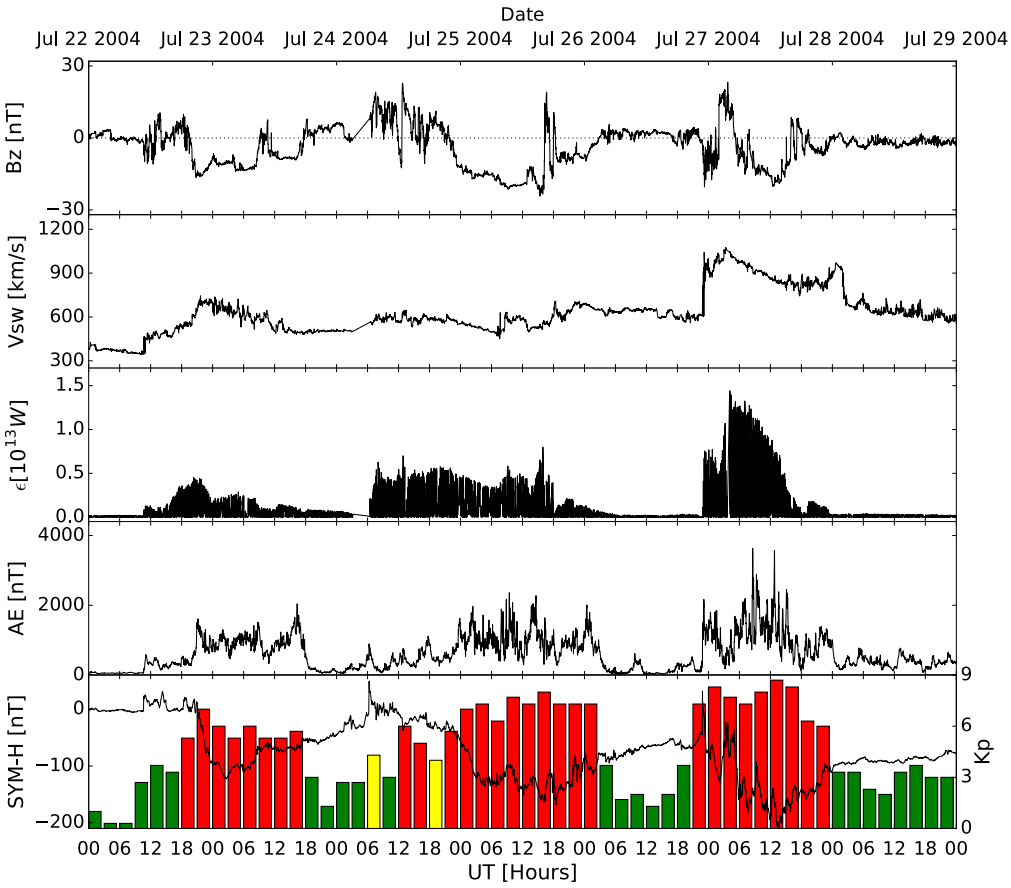

Figure 2: Ground and magnetospheric indices for the period 22-29 July 2004. From top: IMF Bz, solar wind speed, the Akasofu Epsilon parameter, the AE and Sym-H indices (in black) with overlaid 3-hourly Kp (red indicates high geomagnetic activity.

this endeavour its payload included a fluxgate magnetometer measuring the Earth's magnetic field vector. These measurements can be used to derive FACs by solving the curl of the magnetic field in Ampere's law (Wang et al., 2006):

$$j_z = \frac{1}{\mu_o}\left(\frac{\partial B_y}{\partial x} - \frac{\partial B_x}{\partial y}\right) \tag{1}$$

where j_z is the current density, B_x and B_y are the transverse magnetic field vector components generated by the currents, and μ_o is the permeability of free space.

The along-track velocity of CHAMP, similar to the velocity v_x component due to the inclination of CHAMP's orbit, is ~7km/s, therefore we can assume a stationary current sheet as CHAMP passes through the FAC (see Figure 1(b) for a visual interpretation of the FAC current 'sheet') and view these temporal measurements as spatial. Thus the current density now relies on discrete data:

$$j_z = \frac{1}{\mu_o v_x}\frac{\Delta B_y}{\Delta t} \tag{2}$$

where B_y is the magnetic field vector component parallel to the FAC current sheet and Δt is the sampling time of CHAMP, typically 1 second. The absolute current density is used, as we are only concerned with the strength of the FACs and their magnetic latitudes (the latter calculated from the orbit of CHAMP). A threshold is then applied to ensure the derived values are not quiet-time FACs; here we impose a lower limit of $10\mu A/m^2$]. Note that the

threshold used by Wang et al. (2006) was one order of magnitude lower, as they found this limit to be indicative of a storm (Wang et al., 2005); this was used as a guideline and the threshold was increased until a distribution independent of orbit became apparent.

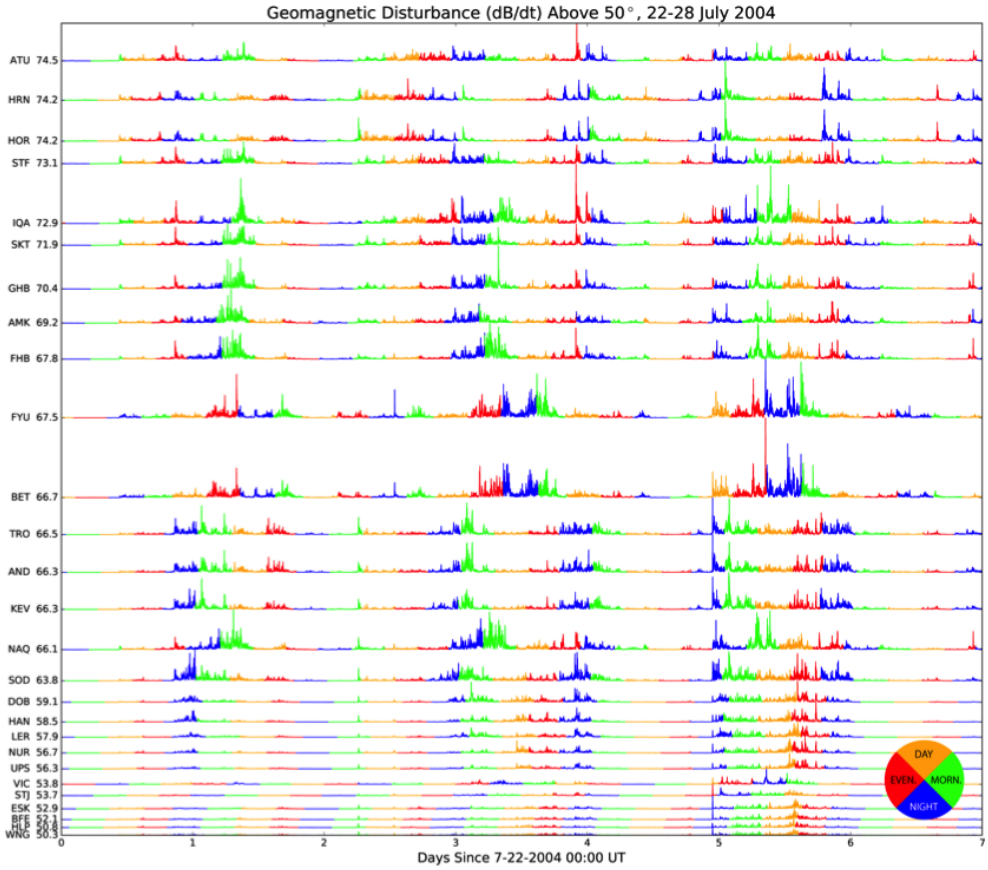

Figure 3: Ground SuperMAG magnetometer data outlining the geomagnetic disturbances measured by ground stations above 50̊ magnetic latitude for the storm period 22-29 July 2004. The perturbations are offset so that they are ordered by latitude, and all use the same scaling, with the largest value of any of the series reaching ~30 nT/s. The colour wheel indicates the local time sector. The 3-letter acronyms are station codes and a list giving station names, abbreviations and locations can be found at`http://supermag.jhuapl.edu`

2.1. Overview of the 22-29 July 2004 geomagnetic storm

During the 22-29 July 2004 three CMEs reached the Earth (Zhang et al., 2007) resulting in three high-intensity geomagnetic storms of increasing minimum Dst peak intensity on the 23rd (-99nT at 02:00UT), 25th (-136nT at 16:00UT) and 27th (-170nT at 13:00UT). These Dst values of ~-100nT or below indicate that all three storms were intense events (Gonzalez et al., 1994), though not extreme. During the three events Kp became very active, peaking at 9- soon after midday during the final storm. Figure 2 outlines the magnetospheric and geomagnetic conditions during this period including: the IMF Bz component (in GSM coordinates), the solar wind speed, the Akasofu Epsilon parameter representative of the energy input into the magnetosphere and dependent on solar wind speed, IMF magnitude and IMF clock angle (Akasofu, 1979), and the Sym-H, Kp and the Auroral Electrojet (AE) indices. Note the data is 1-minute averaged high resolution OMNI data, excluding the Kp, which is a 3-hour measurement obtained from the World Data Center for Geomagnetism, Kyoto.

The initial, main and recovery phases of the storms are described in detail by Pedatella et al. (2008); here a brief description is given. The first of these storms coincided with a ~13-hour period of southward IMF Bz, beginning its main phase around 19UT on the 22nd, where the Kp indicates high geomagnetic activity. A negative Sym-H

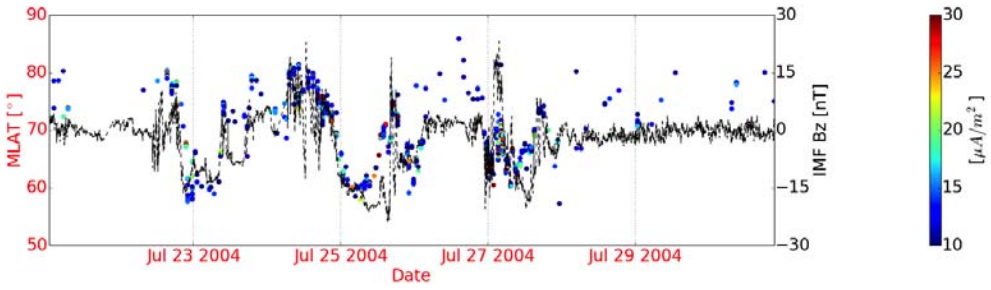

(a)

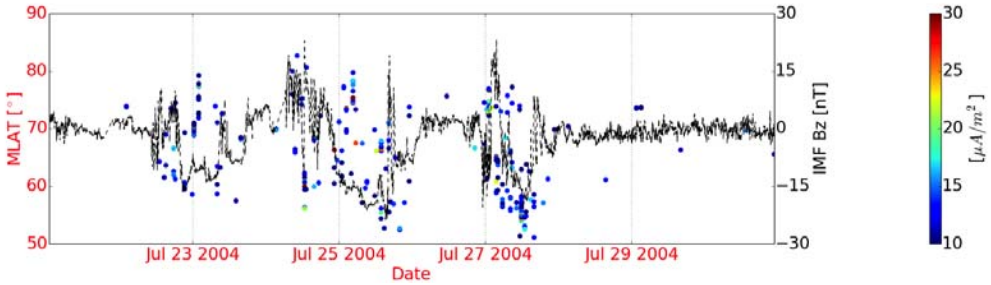

(b)

Figure 4: Correlation between IMF Bz (line and *y*-axis in black) and FAC magnetic latitudes (*y*-axis in red) and respective current density magnitudes (from colorbar) for (a) dayside, and (b) nightside FACs. Both variables share the same *x*-axis. The colorbar indicates the applied threshold to the FAC magnitude, and is capped at $30\mu A/m^2$ to highlight the variation in values.

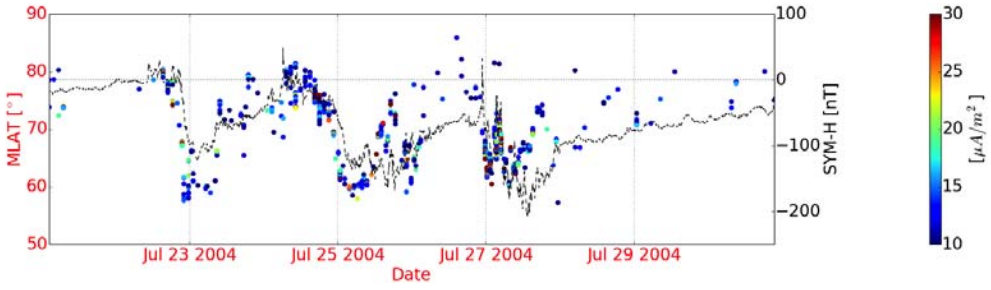

(a)

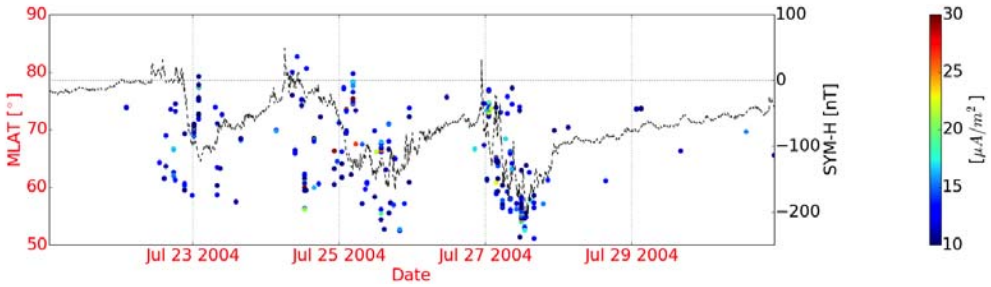

(b)

Figure 5: Correlation between the Sym-H index (line and *y*-axis in black) and FAC magnetic latitudes (*y*-axis in red) and respective current density magnitudes (from colorbar) for (a) dayside, and (b) nightside FACs. Both variables share the same *x*-axis. The colorbar indicates the applied threshold to the FAC magnitude, and is capped at $30\mu A/m^2$ to highlight the variation in values as in Figures 4(a) and 4(b).

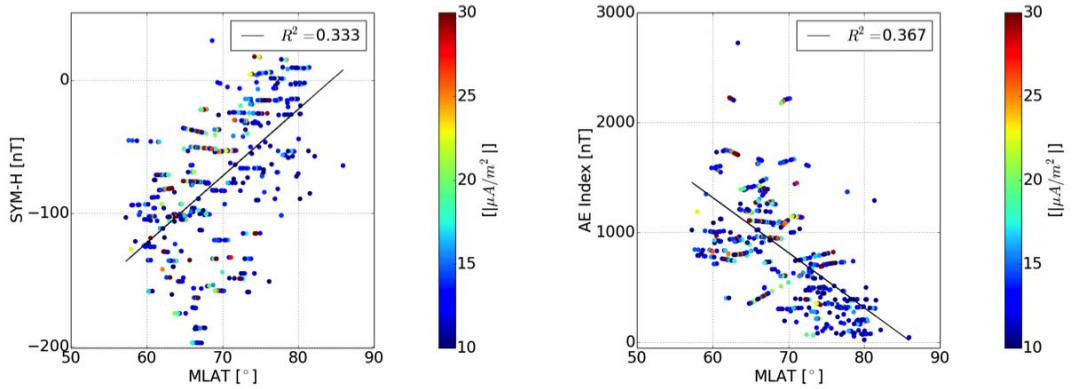

(a) (b)

Figure 6: Scatter plots showing the correlation between (a) Sym-H, (b) AE index, (on the *y*-axis) and FAC magnetic latitudes (on the *x*-axis) and respective current density magnitudes (colorbar). Colorbar as before; R^2 is the coefficient of determination and indicates the goodness-of-fit of the plotted linear relation (black line).

index value, as seen in Figure 2, is also suggestive of geomagnetic activity and is used in this study to define each storm period. Here a southward IMF Bz drives the energy input from the solar wind into the magnetosphere (see for example, Dungey (1961)). The Sym-H index is then seen to recover to near $0nT$ after reaching its minimum value in the early hours of the 23rd. The second storm begins its main phase on the following day at 21:30UT soon after the alignment of IMF Bz shifts strongly southward for an extended period of ~16 hours. The final storm has some overlap with its predecessor but seems to enter its main phase on the 27th at 5UT with intermittent southward IMF Bz for ~11 hours. Referring to the solar wind speed data, also tied to the severity of the storm (see Gonzalez et al. (2011)), the shock occurring at the start of the 3rd storm is very large, with speeds reaching ~1100km/s.

The AE index suggests a strong enhancement of ionospheric currents in the auroral oval, and in turn, energy deposition and Joule heating. An integration of the Akasofu Epsilon parameter with respect to time is also an indication of the total energy input into the magnetosphere from the solar wind. For each storm this equates to $0.5, 1.3, 2.4x10^{12}J$ respectively. The last storm was a very prolonged event, with the recovery phase extending beyond 31st July (Pedatella et al., 2008).

Figure 2 details the ground response during this time period; this shows dB/dt SuperMAG data measured by ground stations above 50° magnetic latitude, with the colour wheel indicating the local time sector. The three encompassed storms are seen in the data, with the largest ground GMDs occurring in the nightside (blue) or near where night meets evening and morning (red and green respectively).

3. Results

3.1. FACs correlation to indices

Figures 4(a) and 4(b) show the correlation between IMF Bz and magnetic latitude of the FACs for the dayside and nightside respectively, as defined by magnetic local time. The colorbar denotes the absolute magnitude of the FAC, where a lower threshold of $10\mu A/m^2$ and upper limit of $30\mu A/m^2$ have been applied to exclude quiet-time FACs whilst highlighting the variation in values. Figures 5(a) and 5(b) show the correlation between the Sym-H index and magnetic latitudes of the FACs for the dayside and nightside respectively.

Figure 4(a) shows a strong correlation between IMF Bz and the magnetic latitudes of FACs in the dayside, revealing the dependence on dayside reconnection where the magnetopause currents are being fed into the FACs (Ma et al., 1995). There is, however, no apparent relationship with FAC magnitude. The nightside currents, due to tail reconnection (Mauk and Zanetti, 1987), are less correlated; indeed the chaotic nature of this system is evident in Figure 4(b). The FACs penetrate to lower magnetic latitudes on the nightside than the dayside and are thus more likely the cause of the largest GMDs, this is supported by ground data (see Figure 2) which show the ground GMDs greatest in the night

local time sector. The locations of the FACs are also sequentially lower, this seems well correlated with the Sym-H intensities in Figure 5(b), likely due to the auroral oval latitude location depending on storm intensity; that is the auroral oval is moving southwards with storm intensity. The dayside FACs in Figure 5(a) also seem more correlated to the Sym-H index than the nightside, with the exception of the last storm on the nightside – this latter dip is of particular interest as it suggests the correlation improving with storm intensity (and perhaps the influence of the ring current in the system), and is the focus of future work.

A quantitative assessment of these correlations is obtained using Ordinary Least Squares (OLS) linear regression and the coefficient of determination, R^2. This gives the fraction of the variation explained by the linear model and thus is an indication of the degree to which the data follows a fitted linear regression line. Ranging between 0 and 1, 1 represents a perfect fit and 0 indicates the data are completely uncorrelated. General trends of the magnetospheric and geomagnetic indices outlined in Figure 2 and their correlations with FAC magnetic latitudes were obtained; here we present the preliminary findings of a selected few. Figures 6(a) and 6(b) show the linear regression fits for the Sym-H and AE indices with FAC magnetic latitude respectively; again the colorbar denotes FAC absolute magnitude. As expected, trends are apparent in the data; low Sym-H and high AE indices values correspond to low FAC magnetic latitudes, that is, a larger storm expands the auroral oval and forces the FACs more equatorward. Another expected correlation also seen in the data and not shown here is high solar wind speed correlating well with low magnetic latitudes.

3.2. Time-lag correlations

With linear regression applied, time lags representative of the response and propagation times were introduced to indices to see if tighter correlations could be realised. For example, the IMF Bz data was lagged by 4 minutes, a realistic propagation from the bow shock to FAC system, which improved the correlation between dayside FAC magnetic latitudes. Time lags were applied to IMF Bz, solar wind speed, Sym-H, the Akasofu Epsilon parameter and AE index. Figures 7(a) and 7(b) show the IMF Bz data and dayside FAC magnetic latitude linear regressions before and after introducing a 4-minute lag respectively. An improvement is seen with the lagged data, indeed most correlations with indices can be improved with some introduction of a time lag. This method was also repeated for nightside data, however due to the tumultuous nature of the data there seems to be little correlation at this stage of data processing. However, it is important to note there is some improvement in correlations for larger time lags, peaking at 45 minutes for IMF Bz, and perhaps suggestive of the longer propagation time needed for the nightside magnetosphere to respond to the changes in IMF Bz.

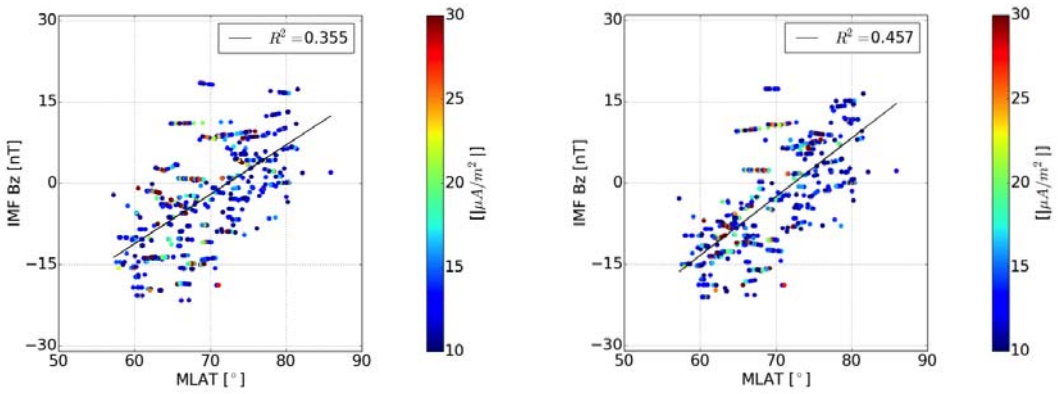

Figure 7: Scatter plots showing the introduction of a 4-minute time lag to the IMF Bz data (on the *y*-axis) correlation to the FAC magnetic latitudes (on the *x*-axis) and respective current density magnitudes (colorbar). (a) Without time lag, (b) 4-minute time lagged. Colorbar as before; $\hat{R}$ is the coefficient of determination and indicates the goodness-of-fit of the plotted linear relation (black line).

Furthermore to this, underlying processes can be inferred from time-lagging each of the three storms to find the optimum time lag and thus response time. Focusing on the more correlated dayside, 0-15 minute lags in 1-minute

increments were introduced to obtain the best correlation using R^2 as the metric of fit. Table 1 outlines the optimum time lag for each storm and the improvement in R^2 in terms of percentage. Here, the propagation and response times of the storms seem to increase with storm intensity. Physically, we expect the response to be faster with successive storms as the current system is already in place from each predecessor. However, in Figure 2 the Sym-H gradient between its initial and main phases seems to be successively less steep, which may be tied to the response times. Here, a more robust linear regression fit must be applied to ensure the statistics used are reliable, however this is a preliminary indication that the response is slower with storm strength. Moreover, from this it is evident that the goodness-of-fit can be improved by separating the storms, which implies the linear relationship between IMF Bz and FAC magnetic latitudes is changing between events.

Date of Storm	Initial R^2	Final R^2	R^2 Improvement (per cent)	Time Lag (minutes)
23-24th	0.667	0.787	18	2
25-26th	0.298	0.300	0.7	3
27-28th	0.107	0.394	268	9

Table 1: Response times of each storm in July 2004, with R^2 percentage improvement as an indicator of reliability

4. Conclusions & Further Work

A strong correlation between dayside FAC magnetic latitudes and IMF Bz has been demonstrated, in agreement with Wang et al. (2006). Dayside FACs are better correlated with IMF Bz due to magnetopause reconnection and are on average higher in magnitude, however the nightside FACs, related to tail reconnection, reach to lower magnetic latitudes, and the highest ground GMDs are observed during the local night sector. This implies the nightside FACs are responsible for the highest ground GMDs, and thus the more equatorward the FAC the better it may be at generating GMDs, with the magnitude of the FAC being secondary to this. General trends between indices and FAC magnetic latitudes have also been assessed, including the Sym-H and AE indices, with expected results. There is a strong correlation with the Sym-H index, and evidence of the nightside FACs descending with increasing Sym-H intensity, suggestive of an auroral oval expansion, and also an indication that the nightside is more organised at intense storms. This intermittency in Sym-H may also be suggestive of a preconditioner making the ionosphere more susceptible to large fluctuations, and in turn GMDs. Finally, we note that time lags, related to propagation and response, improve these correlations.

The next stage of this project aims to improve the robustness of the linear regression fitting, focus on the link between ground GMDs and FACs using ground data, and verify the CHAMP results with another satellite. This work is the focus of a paper in preparation.

Acknowledgments

Magnetospheric indices data were obtained from the High Resolution OMNIWeb Data Explorer (available from: `http://omniweb.gsfc.nasa.gov/ow_min.html`) and Kp data from the World Data Center for Geomagnetism, Kyoto (available from: `http://wdc.kugi.kyoto-u.ac.jp`).

References

Akasofu, S.I., 1979. Interplanetary energy flux associated with magnetospheric substorms. Planetary and Space Science 27, 425 – 431.

Cowley, S.W.H., 2013. Magnetosphere-Ionosphere Interactions: A Tutorial Review. American Geophysical Union. pp. 91–106.

Dungey, J.W., 1961. Interplanetary magnetic field and the auroral zones. Phys. Rev. Lett. 6, 47–48.

Fukushima, N., 1976. Generalized theorem for no ground magnetic effect of vertical currents connected with Pedersen currents in the uniform-conductivity ionosphere. Report of Ionosphere and Space Research in Japan, vol. 30, no. 1-2, June 1976, p. 35-40. 30, 35–40.

GFZ, 2009. Champ: Mission and orbit. [Online; accessed 2016-10-27].

Gonzalez, W.D., Echer, E., Tsurutani, B.T., Clúade Gonzalez, A.L., Dal Lago, A., 2011. Interplanetary origin of intense, superintense and extreme geomagnetic storms. Space Science Reviews 158, 69–89.

Gonzalez, W.D., Joselyn, J.A., Kamide, Y., Kroehl, H.W., Rostoker, G., Tsurutani, B.T., Vasyliunas, V.M., 1994. What is a geomagnetic storm? Journal of Geophysical Research: Space Physics 99, 5771–5792.

Kamide, Y., 1982. The relationship between field-aligned currents and the auroral electrojets: A review. Space Science Reviews 31, 127–243.

Lloyds, 2013. Solar storm risk to the north american electric grid. [Online; accessed 2016-10-27].

Ma, Z.W., Lee, L.C., Otto, A., 1995. Generation of field-aligned currents and Alfven waves by 3d magnetic reconnection. Geophysical Research Letters 22, 1737–1740.

Mauk, B.H., Zanetti, L.J., 1987. Magnetospheric electric fields and currents. Reviews of Geophysics 25, 541–554.

National Research Council, 2008. Severe Space Weather Events–Understanding Societal and Economic Impacts: A Workshop Report. The National Academies Press, Washington, DC.

Pedatella, N.M., Forbes, J.M., Lei, J., Thayer, J.P., Larson, K.M., 2008. Changes in the longitudinal structure of the low-latitude ionosphere during the july 2004 sequence of geomagnetic storms. Journal of Geophysical Research: Space Physics 113. A11315.

Riswadkar, A., Dobbins, B., 2010. Solar storms: Protecting your operations against the sun's 'dark side'. [Online; accessed 2016-10-03].

Royal Academy of Engineering, 2013. Extreme space weather:impacts on engineered systems and infrastructure. Royal Academy of Engineering, London, UK.

Viljanen, A., Pirjola, R., Prcser, E., Katkalov, J., Wik, M., 2014. Geomagnetically induced currents in europe. J. Space Weather Space Clim. 4, A09.

Wang, H., Lühr, H., Ma, S.Y., Weygand, J., Skoug, R.M., Yin, F., 2006. Field-aligned currents observed by champ during the intense 2003 geomagnetic storm events. Annales Geophysicae 24, 311–324.

Wang, H., Lhr, H., Ma, S.Y., 2005. Solar zenith angle and merging electric field control of field-aligned currents: A statistical study of the southern hemisphere. Journal of Geophysical Research: Space Physics 110. A03306.

Zhang, J., Richardson, I.G., Webb, D.F., Gopalswamy, N., Huttunen, E., Kasper, J.C., Nitta, N.V., Poomvises, W., Thompson, B.J., Wu, C.C., Yashiro, S., Zhukov, A.N., 2007. Solar and interplanetary sources of major geomagnetic storms (dst 100 nt) during 19962005. Journal of Geophysical Research: Space Physics 112. A10102.

Preparing a more useful HOPE data set for wave-particle interaction studies

Lilla Juhász

Eötvös University, Pazmany Peter Setany 1/A., Budapest, H-1117 Hungary

Reinhard H. W. Friedel

Los Alamos National Laboratory National Security Education Center (NSEC) MS-T001, Los Alamos, NM 87545, USA

Brian Larsen

Los Alamos National Laboratory National Security Education Center (NSEC) MS-T001, Los Alamos, NM 87545, USA

Abstract

The generation mechanism of whistler-mode chorus waves remains a subject of debate, even though chorus waves are known to be responsible for prompt changes in outer radiation belt conditions. For several theories intended to explain results of empirical studies of wave-particle interaction, validation requires thorough research based on (and by the use of) precise/accurate datasets. Measurements of electromagnetic waves and particles taken by the instruments EMFISIS, HOPE and MagEIS on the Van Allen Probes are ideal for such studies. In this paper we aim to demonstrate the reliability and efficiency of the HOPE instrument from this point of view. A preliminary investigation of HOPE L1 data's count rates is shown; the typically low count rates of this instrument requirtes efforts designed to raise the signal to noise ratios above SNR ≈ 10. In addition, the 5 polar pixels of HOPE have not been inter-calibrated yet, leading to inaccuracies when these data are combined to obtain pitch angle distribution (PAD) data. We here use count ratios of neighboring pixels with overlapping pitch angle intervals, to produce pixel-intercalibration data for the entire mission. Finally, we present a robust method to define isotropy or anisotropy in PADs as these represent conditions that are needed for theories of chorus wave generation.

Keywords: wave-particle interaction, HOPE, polar pixel calibration

1. Introduction

There has been a lot of development in radiation belts modeling in recent years, particulary due to the availability of in-situ data from NASA missions such as the Time History of Events and Macroscale Interactions during Substorms (THEMIS), Van Allen Probes (RBSP) and Magnetospheric Multiscale (MMS) missions, which advanced our understanding of the complex inter-connections of the geospace environment. On the other hand, continuous measurements of these models' key parameter inputs are integral part of space weather forecast, for which ground-based measurements can be a more reliable, long-running solution/provision. The PLASMON project is an outstanding example for efforts to produce important key parameters, like plasmasphere densities, with the use of groundbased whistler measurements [Lichtenberger et al. (2013)]. As part of PLASMON, AWDANet [Lichtenberger et al. (2008); Lichtenberger (2009)] is consisting of 28 VLF receiver stations covering low, mid and high latitudes with wide range of longitudes, detects lightning induced whistler waves. Receivers at stations with magnetic footprint $L > 4$ can also record whistler mode chorus emissions.

Coherent chorus emissions are typically observed as rising/falling tones in the frequency range of $0.1 f_{ce} < f < 0.8 f_{ce}$ with discontinuity at $0.5 f_{ce}$, where f_{ce} is the electron gyrofrequency [Burtis and Helliwell (1969); Koons and

Email addresses: lilla@sas.elte.hu (Lilla Juhász), rfriedel@lanl.gov (Reinhard H. W. Friedel), blarsen@lanl.gov (Brian Larsen)

Roeder (1990); Santolik et al. (2003); Sazhin and Hayakawa (1992)]. These emissions are typically excited during geomagnetic storms close to the magnetic equator in low-density plasmas near outside the plasmapause. Chorus emissions are known to be generated via wave-particle interactions with an anisotropic distribution of energetic electrons (few keV- 100 keV) injected from the plasmasheet [Kennel and Petschek (1966); Anderson and Maeda (1977); LeDocq et al. (1998); Meredith et al. (2001); Omura et al. (2009); Santolik et al. (2010);Li et al. (2013); Spasojevic (2014)]. General consensus has not been reached yet on the exact generation mechanism of chorus waves, but electron cyclotron resonance seems to be the most accepted [Kennel and Petschek (1966); Kennel and Thorne (1967); Tsurutani and Smith (1974); Nunn et al. (1997); Chum et al. (2007); Katoh and Omura (2007a), Katoh and Omura (2007b); Omura et al. (2008)]. Anisotropic angular distributions of substorm injected energetic electrons (also called source population [Jaynes et al. (2015)]) are able to provide free-energy for chorus wave excitation [Thorne et al. (2013), and references therein] and cause isotropic PAD at the energy range of interacting particles. Attention of radiation belt modelers recently turned to whistler mode chorus waves due to its role in both accelerating electrons to MeV energies in the Earth's outer radiation belt [Horne and Thorne (1998); Summers et al. (1998); Summers et al. (2002); Reeves et al. (2013); Thorne et al. (2013); Li et al. (2014)] and in pitch angle scattering of electrons into the atmospheric loss cone [Lorentzen et al. (2001); O'Brien et al. (2004); Thorne et al. (2005); Hikishima et al. (2010)].

The AWDANet Team is currently working on deriving density and energy of energetic electrons (source population) from chorus emissions recorded on the ground. This seems to be feasible since the nonlinear theory of Omura et al. (2008) and Omura and Nunn (2011) have found a relation between some of the characteristics of the rising tone chorus signal (frequency sweep rates, threshold and optimum wave amplitudes) and the energy and number density of energetic electrons in the source region. As it was proposed by this theory, chorus wave elements are generated close to the magnetic equator from coherent whistler mode waves which are excited by linear instability caused by temperature anisotropy. Through nonlinear wave mechanism in a direction parallel to the magnetic field lines, rising-tone chorus emissions can be triggered. During its slightly oblique propagation away from the equator, the gap at $0.5 f_{ce}$ is formed by nonlinear wave damping. As a first step, we should validate this non-linear theory with simultaneous measurements of particles and waves from Van Allen Probes HOPE and EMFISIS instruments, and later form a robust model which can be used in an inversion model which can derive the in-situ densities from ground-based chorus detection.

In Section 2. a brief introduction of the Van Allen Probes - HOPE instrument is presented to outline the HOPE data sets we examine in Section 3. In Section 4. a robust method is introduced to find isotropic pitch angle distributions as possible signatures of chorus emission interaction, which can be used as a "first-round" selection of HOPE data. Section 5 summarizes my work the Los Alamos Space Weather Summer School and also shares some ideas of future research.

2. Van Allen Probe HOPE Data

The Van Allen Probes (Mauk et al., 2013), also called Radiation Belt Storm Probes (RBSP), were designed to explore the harsh environment of the radiation belts and its processes, as well as examine those spatially overlapping regions which strongly affect the dynamics of the Van Allen radiation belts. One spacecraft follows the other on a slightly different, nearly equatorial (inclination 10.2°) and highly elliptical orbit with perigee 618 km and apogee 30, 414 km (5.8 RE). To fulfill the mission's scientific objectives, a wide range of wave and particle instruments are mounted on both spacecrafts:

Radiation Belt Storm Probes Ion Composition Experiment (RBSPICE)
Relativistic Proton Spectrometer (RPS)
Electric Field and Waves Suite (EFW)
Electric and Magnetic Field Instrument Suite and Integrated Science (EMFISIS)
Energetic Particle, Composition, and Thermal Plasma Suite (ECT) which consists of:
- Helium Oxygen Proton Electron (HOPE)
- Magnetic Electron Ion Spectrometer (MagEIS)
- Relativistic Electron Proton Telescope (REPT)

The Helium, Oxygen, Proton, and Electron (HOPE) Mass Spectrometer (Funsten et al., 2013) is in the focus of this study, which is intended to measure the fluxes of electrons and dominant ion species in the energy range of 1 eV - 50 keV, in 36 logarithmically spaced steps (before September 2013) and later modified to 72 log-spaced steps at an energy resolution $\Delta E_{FWHM}/E \approx 15\%$. The 4π sr field of view is achieved with 5 polar pixels (consisting of individual detectors) and the spin of the spacecrafts, however, HOPE data sampling is not spin synchronized. Polar pixels are centered at polar angles ±72°, ±36°, 0°, where the latter points perpendicular to the spin axis of the spacecraft. The $2\,\pi$ azimuthal region is divided into 16 sectors, each sector contains a sequence of energy data from the entire range. For telemetry reasons, sectors of polar pixels ±72° are averaged to 4 sectors, leading to similar solid angles sampling for all pixels. As a result, HOPE measurements provide the number of incoming particles in 4 dimensional parameter space: a fixed time cadence of ~ 24 sec for a full, measurements of electrons and ions, 5 polar pixels, 72 or 36 energy steps and nominal 16 azimuthal sectors. In Section 3, Level 1 electron count rate data are used along with pitch angle tagging for every sector, detector, energy and time.

Wave-particle interaction studies require electromagnetic wave data. EMFISIS (Kletzing et al., 2013) measures six component of wave electric and magnetic field in continuous waveform burst data mode covering the frequency range 10 Hz- 12 kHz. It also provides a single wave electric field component in the range of 10 kHz - 500 kHz with which electron cyclotron harmonics and upper-hybrid frequency can be detected, consequently electron densities are deductible as well. EMFISIS also includes the MAG instrument which provides three-dimensional background magnetic field vectors essential for wave-particle studies.

3. HOPE performance

3.1. Low count rates

As mentioned earlier to verify (and to use for ground-based measurements) the theory of non-linear chorus generation we must use characteristics of individual chorus signatures and simultaneously measured electron PADs. The complexity of the theory implies the need of reliable input data, while at the same time HOPE often lacks the counting statistics needed, so our first goal is to examine the validity of HOPE data. From Level 1 pitch angle tagged Count data we created a time-energy-pitch angle dependent counts product, using only mode 0 (the main science mode data). On the top panel of Figure 1 a, the daily variation of total electron content can be seen as a function of energy during 1st of June 2016, lower boxes show the position of the spacecraft. The top panel of Figure 1 b, shows particle counts at an energy 833.1 eV. Unequal sized pitch angle bins are used with narrower bin sizes around 90° to account for the lower counting rate in the field-aligned directions.

Assuming a Poisson distribution of incoming particles, the signal to noise ratios (SNR) are calculated as the square root of total counts. In the bottom panel of Figure 1 b, as function of time the SNR values are presented, the red line at SNR = 12 indicates the lowest value of the desired counting statistics. The data is analyzed by using moving averages with different sized windows: the window size grows until the total count content reaches 144 (i.e SNR =12) then moves on. Bottom panel of Figure 1 b, presents the results: signal to noise ratio is always above 12 (points at zeros indicates the dropped-out times), on the other hand the time resolution of the measurements is reduced during low count rate periods. This simple method is a great tool to increase the accuracy of our calculation presented in the following section.

(a)

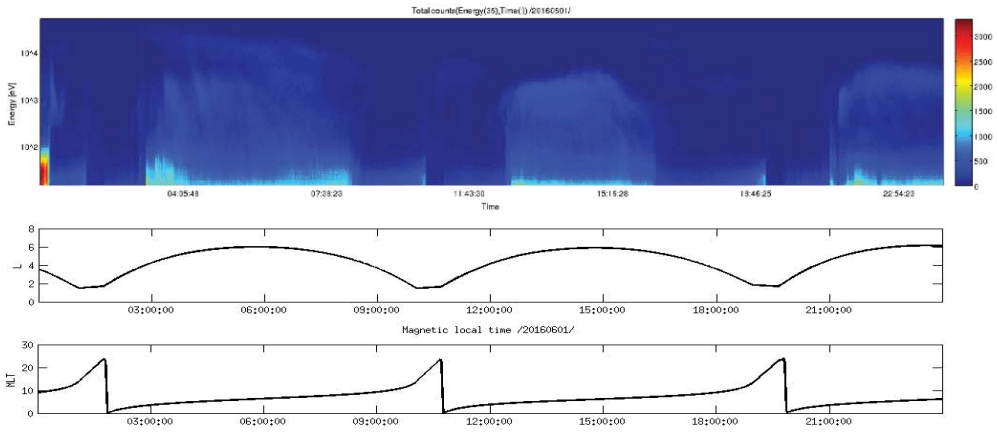

(b)

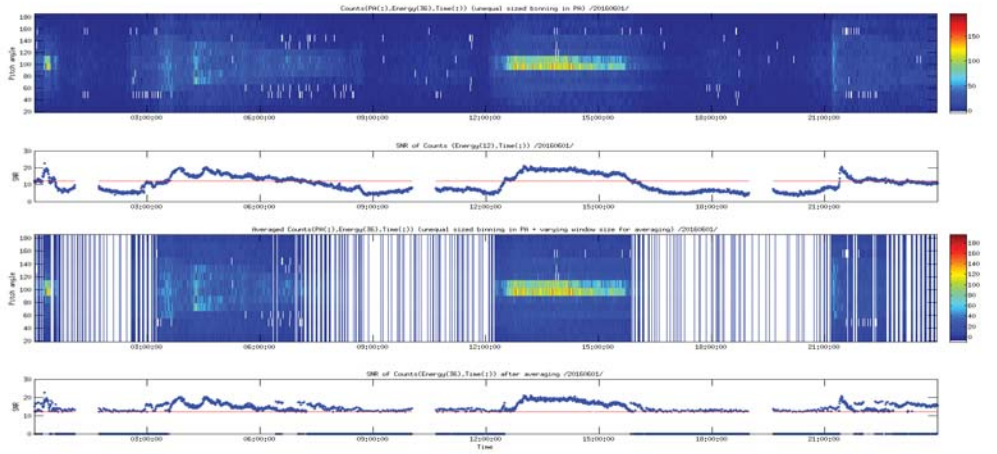

Figure 1: (a) Total counts of electrons measured by VAP-A HOPE during 1 June 2016 in the energy range of 1 eV - 50 keV accompanied by L parameter and MLT of S/C ; (b) Pitch angle distributions of electrons at 833.1 eV and its signal-to-noise ratios measured by VAP-A HOPE during 1st June 2016

3.2. Inter-calibration of polar pixel detectors

Besides low count rates, the different gains of pixel detectors can cause other uncertainties in pitch angle resolved data. In Figure 2 the pitch angle variation and the overlapping PA views of individual detectors can be followed. Assuming that count rates change relatively slow, we can use total count rates of the common pitch angle areas of neighboring detectors to compare detector gains. Taking the interval of $70^\circ - 110^\circ$ and selecting only periods when the total electron count is higher than 100, a list of detector ratios are created (Figure 3). During the mission, detector gains are changed individually except the period for 2014 October - 2015 February, while at late May 2015 a gain correction can be seen clearly. However a few months later the so-called detector five's gain started to shift independently. Comparing the changes of calibration ratios to the DST and energetic particle data from MAGEIS, see the example of year 2015 on Figure 4, it is obvious that geomagnetic storms effect the performance of HOPE.

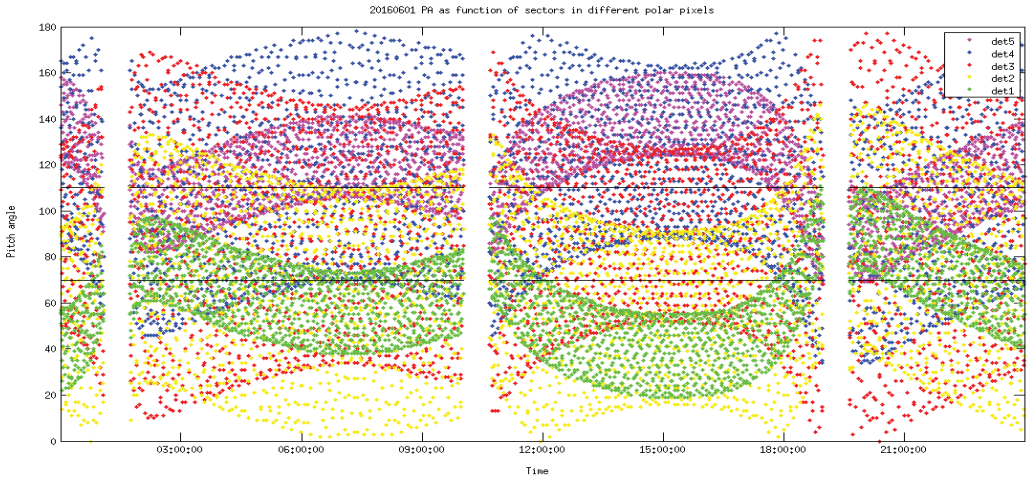

Figure 2: Pitch angle covering of detectors at 1st of June 2016

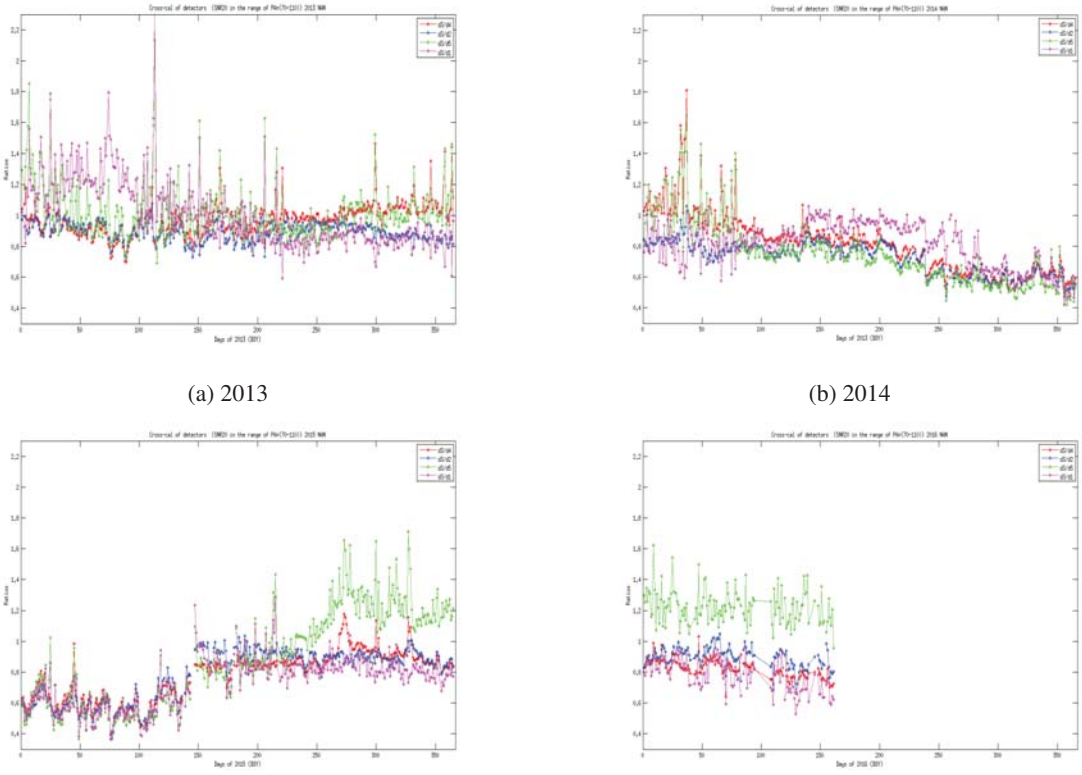

(a) 2013

(b) 2014

(c) 2015

(d) 2016

Figure 3: Ratios of counts referring to the middle detector of Van Allen Probes HOPE-A instrument from 2013-2016

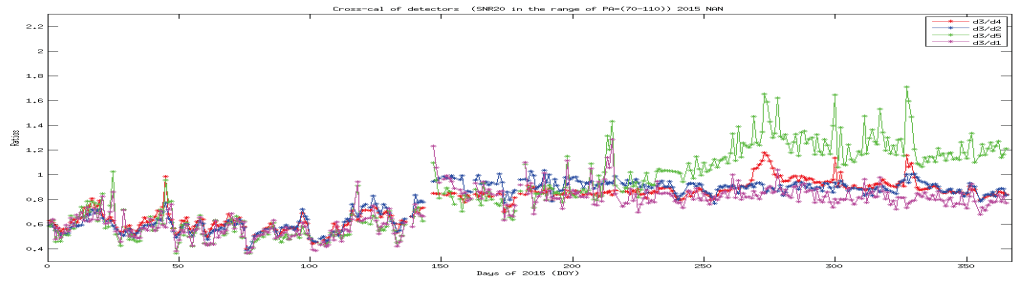

(a) Ratios of counts referring to the middle detector of VAP HOPE-A in 2015

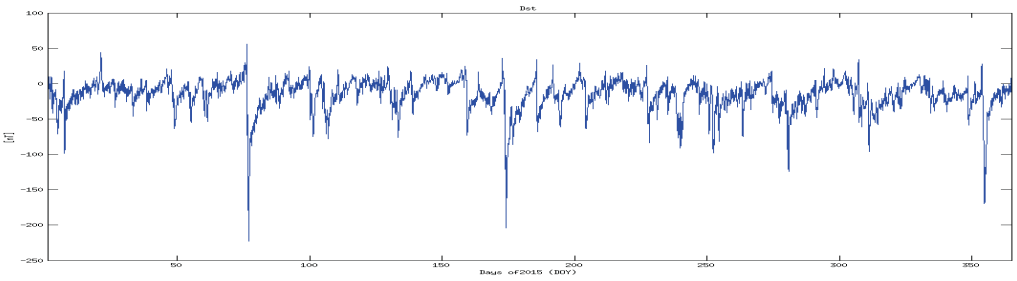

(b) DST values in 2015

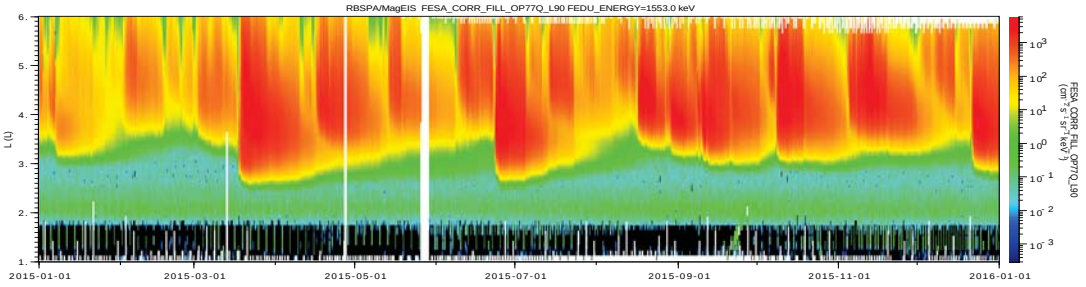

(c) MAGEIS E = 1553.0 keV

Figure 4: Comparison of gain changes to DST and MAGEIS data in 2015

4. PAD isotropy

As it was written in the introduction, anisotropic PADs can be the signature of freshly injected energetic particles, which assumed to be the free energy source of whistler mode waves. Isotropic PADs can be the results of pitch angle scattering caused by wave-particle interaction. Different PAD fitting methods have already developed [Chen et al. (1999) for proton ring current; Chen et al. (2014) for relativistic electrons] and used successfully to determine at least the measure of anisotropy. The sensitivity of HOPE data, which results in noisy pitch angle distributions due to low count rates despite of the 5 min averages we use in this section, motivates us to utilize a robust method again. We increase counting statistics by assuming PAD symmetry around $PA = 90°$ and sum the counts while ignoring loss cone, then define 3 boxes Figure (5a) in the domain of pitch angles and compute ratios A/B and A/C. If both ratios fulfill the criteria

$$0.8 < \frac{C \pm SNR}{[A,B] \pm SNR} < 1.2 \tag{1}$$

then the given PAD is declared to be isotropic. Figure 5b shows PADs of particles at different energies in 14 November

2012 14:10UT, lines with filled dots represent isotropic PADs. We run our code on the entire dataset of VAP-A HOPE electron counts (for example 2012 in Figure 6), and also plot Dst index in order to compare geomagnetically disturbed periods with those we found to have isotropic PADs. Note that low Dst values are not direct indicators of chorus wave excitation. In Figure 7a we show the daily variation of isotropic PADs and the simultaneous measurements of VAP-A EMFISIS in Figure 7b, one of the electric and magnetic component of the wave data can be found, with white lines indicating half the gyrofrequency. Chorus waves are showing up 00:30-07:00 and 09:00-15:00, latter one includes the gap at $0.5 f_{ce}$. For the validation of the nonlinear theory of Omura, the existence of isotropic PADs and chorus waves is not enough, but the above described method can be an easy way to find the first examples for our validation process.

(a) (b)

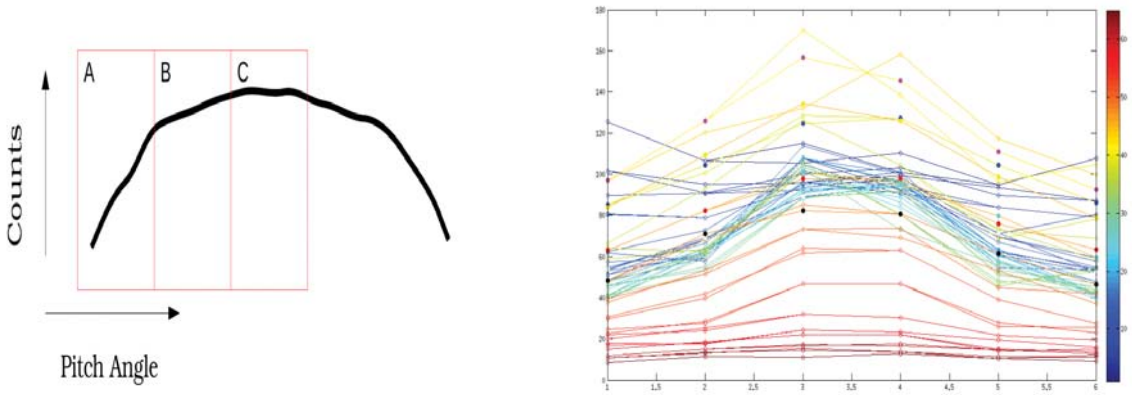

Figure 5: Sketch of how to define isotropy and an example of finding isotropic PADs in 14 November 2012 14:10UT on VAP-A HOPE

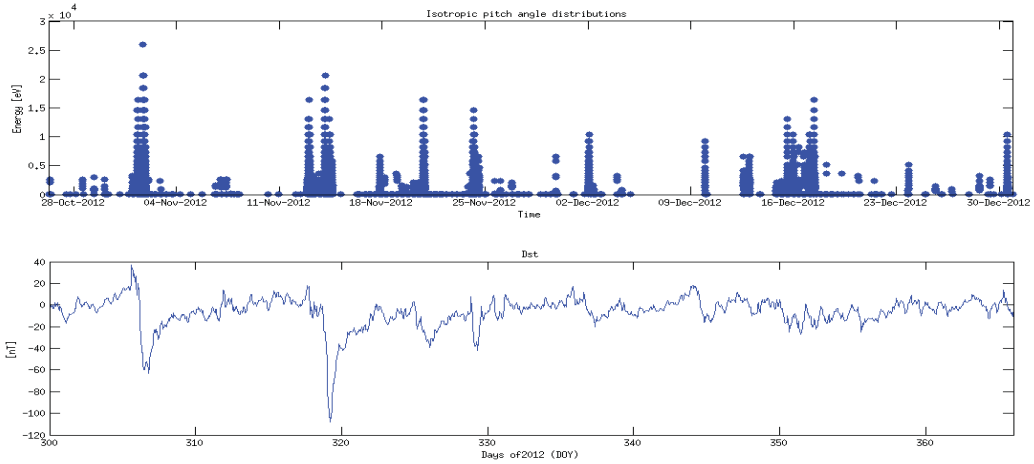

Figure 6: Isotropic pitch angle distributions in 2012 as a function of time and energy and Dst indexes during same time

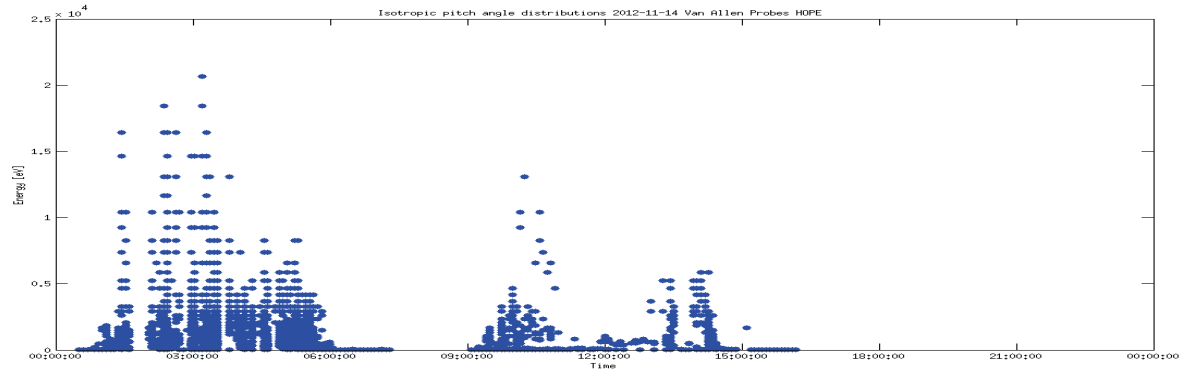

(a) Isotropic PADs of VAP-A HOPE in 2012-11-14 at different energies

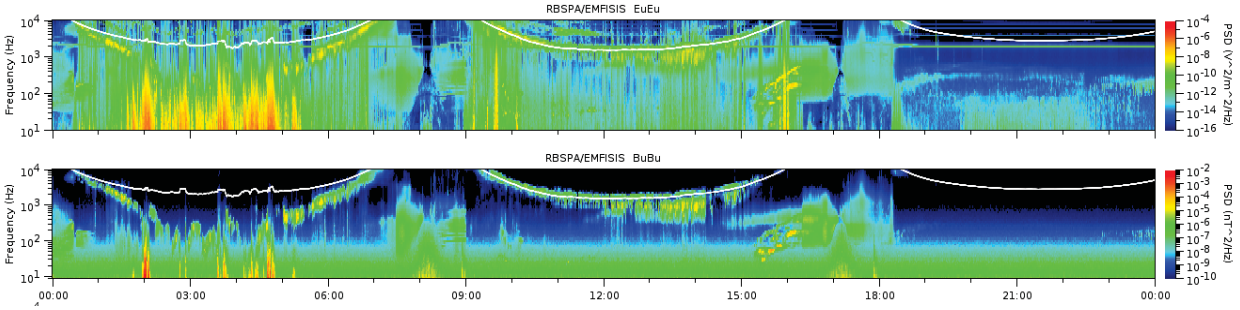

(b) VAP-A EMFISIS EuEu and BuBu component during 2012-11-14 with $0.5 f_{ce}$ (white line)

Figure 7: Comparison of isotropic PADs and electromagnetic waves during 2012-11-14. On plots of Figure b, whistler-mode chorus waves can be found close (or around) half the gyrofrequency

5. Conclusion

In this work here at LANL I have established robust criteria and methods to detect conditions of isotropy in the Hope data, which is one of the indicators of wave-particle interactions. Continued work will consist of a systematic study of all Hope pitch angle data to establish energy ranges and times of isotropy, and to compare those to the EMFISIS wave data through minimum resonant energies of waves. When we have the sufficient number of events, a statistical study should be carried out to validate the relation between the earlier mentioned characteristics of chorus elements and energetic particles. In the far future the propagation of chorus waves from the generation region to the ground will be examined, which is the last piece of the theoretical description required for an inversion method. This inversion method will be able to derive important parameters of low-energy electrons in the equatorial region from ground detected chorus elements.

6. References

Anderson, R.R., Maeda, K., 1977. VLF emissions associated with enhanced magnetospheric electrons. Journal of Geophysical Research 82, 135–146.

Burtis, W.J., Helliwell, R.A., 1969. Banded chorus—A new type of VLF radiation observed in the magnetosphere by OGO 1 and OGO 3. Journal of Geophysical Research 74, 3002–3010.

Chen, M.W., Roeder, J.L., Fennell, J.F., Lyons, L.R., Lambour, R.L., Schulz, M., 1999. Proton ring current pitch angle distributions: Comparison of simulations with CRRES observations. Journal of Geophysical Research: Space Physics 104, 17379–17389.

Chen, Y., Friedel, R.H.W., Henderson, M.G., Claudepierre, S.G., Morley, S.K., Spence, H.E., 2014. REPAD: An empirical model of pitch angle distributions for energetic electrons in the Earth's outer radiation belt. Journal of Geophysical Research: Space Physics 119, 1693–1708. 2013JA019431.

Chum, J., Santolik, O., Breneman, A., Kletzing, C., Gurnett, D., Pickett, J., 2007. Chorus source properties that produce time shifts and frequency range differences observed on different Cluster spacecraft. Journal of Geophysical Research: Space Physics 112.

Funsten, H.O., Skoug, R.M., Guthrie, A.A., MacDonald, E.A., Baldonado, J.R., Harper, R.W., Henderson, K.C., Kihara, K.H., Lake, J.E., Larsen, B.A., Puckett, A.D., Vigil, V.J., Friedel, R.H., Henderson, M.G., Niehof, J.T., Reeves, G.D., Thomsen, M.F., Hanley, J.J., George, D.E., Jahn, J.M., Cortinas, S., De Los Santos, A., Dunn, G., Edlund, E., Ferris, M., Freeman, M., Maple, M., Nunez, C., Taylor, T., Toczynski, W., Urdiales, C., Spence, H.E., Cravens, J.A., Suther, L.L., Chen, J., 2013. Helium, Oxygen, Proton, and Electron (HOPE) Mass Spectrometer for the Radiation Belt Storm Probes Mission. Space Science Reviews 179, 423–484.

Hikishima, M., Omura, Y., Summers, D., 2010. Microburst precipitation of energetic electrons associated with chorus wave generation. Geophysical Research Letters 37.

Horne, R.B., Thorne, R.M., 1998. Potential waves for relativistic electron scattering and stochastic acceleration during magnetic storms. Geophysical Research Letters 25, 3011–3014.

Jaynes, A.N., Baker, D.N., Singer, H.J., Rodriguez, J.V., Loto'aniu, T.M., Ali, A.F., Elkington, S.R., Li, X., Kanekal, S.G., Claudepierre, S.G., Fennell, J.F., Li, W., Thorne, R.M., Kletzing, C.A., Spence, H.E., Reeves, G.D., 2015. Source and seed populations for relativistic electrons: Their roles in radiation belt changes. Journal of Geophysical Research: Space Physics 120, 7240–7254. 2015JA021234.

Katoh, Y., Omura, Y., 2007a. Computer simulation of chorus wave generation in the Earth's inner magnetosphere. Geophysical research letters 34.

Katoh, Y., Omura, Y., 2007b. Relativistic particle acceleration in the process of whistler-mode chorus wave generation. Geophysical research letters 34.

Kennel, C.F., Petschek, H., 1966. Limit on stably trapped particle fluxes. Journal of Geophysical Research 71, 1–28.

Kennel, C.F., Thorne, R.M., 1967. Unstable growth of unducted whistlers propagating at an angle to the geomagnetic field. Journal of Geophysical Research 72, 871–878.

Kletzing, C.A., Kurth, W.S., Acuna, M., MacDowall, R.J., Torbert, R.B., Averkamp, T., Bodet, D., Bounds, S.R., Chutter, M., Connerney, J., Crawford, D., Dolan, J.S., Dvorsky, R., Hospodarsky, G.B., Howard, J., Jordanova, V., Johnson, R.A., Kirchner, D.L., Mokrzycki, B., Needell, G., Odom, J., Mark, D., Pfaff, R., Phillips, J.R., Piker, C.W., Remington, S.L., Rowland, D., Santolik, O., Schnurr, R., Sheppard, D., Smith, C.W., Thorne, R.M., Tyler, J., 2013. The Electric and Magnetic Field Instrument Suite and Integrated Science (EMFISIS) on RBSP. Space Science Reviews 179, 127–181.

Koons, H., Roeder, J., 1990. A survey of equatorial magnetospheric wave activity between 5 and 8 RE. Planetary and Space Science 38, 1335–1341.

LeDocq, M., Gurnett, D., Hospodarsky, G., 1998. Chorus source locations from VLF Poynting flux measurements with the Polar spacecraft. Geophysical research letters 25, 4063–4066.

Li, W., Bortnik, J., Thorne, R., Cully, C., Chen, L., Angelopoulos, V., Nishimura, Y., Tao, J., Bonnell, J., LeContel, O., 2013. Characteristics of the Poynting flux and wave normal vectors of whistler-mode waves observed on THEMIS. Journal of Geophysical Research: Space Physics 118, 1461–1471.

Li, W., Thorne, R., Ma, Q., Ni, B., Bortnik, J., Baker, D., Spence, H.E., Reeves, G., Kanekal, S., Green, J., et al., 2014. Radiation belt electron acceleration by chorus waves during the 17 March 2013 storm. Journal of Geophysical Research: Space Physics 119, 4681–4693.

Lichtenberger, J., 2009. A new whistler inversion method. Journal of Geophysical Research: Space Physics 114.

Lichtenberger, J., Clilverd, M.A., Heilig, B., Vellante, M., Manninen, J., Rodger, C.J., Collier, A.B., Jørgensen, A.M., Reda, J., Holzworth, R.H., et al., 2013. The plasmasphere during a space weather event: first results from the PLASMON project. Journal of Space Weather and Space Climate 3, A23.

Lichtenberger, J., Ferencz, C., Bodnár, L., Hamar, D., Steinbach, P., 2008. Automatic whistler detector and analyzer system: Automatic whistler detector. Journal of Geophysical Research: Space Physics 113.

Lorentzen, K., Blake, J., Inan, U., Bortnik, J., 2001. Observations of relativistic electron microbursts in association with VLF chorus. Journal of Geophysical Research: Space Physics 106, 6017–6027.

Mauk, B.H., Fox, N.J., Kanekal, S.G., Kessel, R.L., Sibeck, D.G., Ukhorskiy, A., 2013. Science Objectives and Rationale for the Radiation Belt Storm Probes Mission. Space Science Reviews 179, 3–27.

Meredith, N.P., Horne, R.B., Anderson, R.R., 2001. Substorm dependence of chorus amplitudes: Implications for the acceleration of electrons to relativistic energies. Journal of Geophysical Research: Space Physics 106, 13165–13178.

Nunn, D., Omura, Y., Matsumoto, H., Nagano, I., Yagitani, S., 1997. The numerical simulation of VLF chorus and discrete emissions observed on the Geotail satellite using a Vlasov code. Journal of Geophysical Research: Space Physics 102, 27083–27097.

O'Brien, T., Looper, M., Blake, J., 2004. Quantification of relativistic electron microburst losses during the GEM storms. Geophysical research letters 31.

Omura, Y., Hikishima, M., Katoh, Y., Summers, D., Yagitani, S., 2009. Nonlinear mechanisms of lower-band and upper-band VLF chorus emissions in the magnetosphere. Journal of Geophysical Research: Space Physics 114.

Omura, Y., Katoh, Y., Summers, D., 2008. Theory and simulation of the generation of whistler-mode chorus. Journal of Geophysical Research: Space Physics 113.

Omura, Y., Nunn, D., 2011. Triggering process of whistler mode chorus emissions in the magnetosphere. Journal of Geophysical Research: Space Physics 116.

Reeves, G., Spence, H.E., Henderson, M., Morley, S., Friedel, R., Funsten, H., Baker, D., Kanekal, S., Blake, J., Fennell, J., et al., 2013. Electron acceleration in the heart of the Van Allen radiation belts. Science 341, 991–994.

Santolik, O., Gurnett, D., Pickett, J., Parrot, M., Cornilleau-Wehrlin, N., 2003. Spatio-temporal structure of storm-time chorus. Journal of Geophysical Research: Space Physics 108.

Santolik, O., Gurnett, D.A., Pickett, J.S., Grimald, S., Décreau, P.M.E., Parrot, M., CornilleauWehrlin, N., Mazouz, F.E., Schriver, D., Meredith, N.P., Fazakerley, A., 2010. Waveparticle interactions in the equatorial source region of whistlermode emissions. Journal of Geophysical Research: Space Physics (1978–2012) 115.

Sazhin, S., Hayakawa, M., 1992. Magnetospheric chorus emissions: A review. Planetary and Space Science 40, 681–697.

Spasojevic, M., 2014. Statistical analysis of ground-based chorus observations during geomagnetic storms. Journal of Geophysical Research: Space Physics 119, 8299–8317.

Summers, D., Ma, C., Meredith, N., Horne, R., Thorne, R., Heynderickx, D., Anderson, R., 2002. Model of the energization of outer-zone electrons by whistler-mode chorus during the October 9, 1990 geomagnetic storm. Geophysical research letters 29.

Summers, D., Thorne, R.M., Xiao, F., 1998. Relativistic theory of wave-particle resonant diffusion with application to electron acceleration in the magnetosphere. Journal of Geophysical Research: Space Physics 103, 20487–20500.

Thorne, R., Li, W., Ni, B., Ma, Q., Bortnik, J., Chen, L., Baker, D., Spence, H.E., Reeves, G., Henderson, M., et al., 2013. Rapid local acceleration of relativistic radiation-belt electrons by magnetospheric chorus. Nature 504, 411–414.

Thorne, R.M., O'Brien, T., Shprits, Y., Summers, D., Horne, R.B., 2005. Timescale for MeV electron microburst loss during geomagnetic storms. Journal of Geophysical Research: Space Physics 110.

Tsurutani, B.T., Smith, E.J., 1974. Postmidnight chorus: A substorm phenomenon. Journal of Geophysical Research 79, 118–127.

Coupling of PIC and Vlasov spectral solver in velocity space

Oleksandr Koshkarov

Department of Physics and Engineering Physics, University of Saskatchewan, Saskatoon, Saskatchewan, Canada

Gian Luca Delzanno

Los Alamos National Laboratory, Los Alamos, New Mexico, USA

Gianmarco Manzini

Los Alamos National Laboratory, Los Alamos, New Mexico, USA

Vadim Roytershteyn

The Space Science Institute, Boulder, Colorado, USA

Abstract

A new method for the solution of the kinetic equations for a collisionless plasma has been developed. It treats part of the distribution function with a spectral (moment-based) expansion in Hermite basis, while the remaining part of the distribution function is described with macro-particles as in the Particle-In-Cell (PIC) approach. The goal is to combine the accuracy typical of spectral methods, with the flexibility of PIC in dealing with complex distribution functions that might otherwise require a large number of moments for convergence. The application of the new method is studied on the example problem of interaction of a weak beam with background plasma. This problem is challenging for both conventional PIC and spectral methods due to the low density of the beam and the complex, quickly evolving, shape of the distribution function. The potential of the new method is demonstrated and its efficiency and accuracy are characterized.

Keywords: PIC, Spectral methods, Kinetic plasma simulations, Beam instability

1. Introduction

The Vlasov-Maxwell system describes kinetic evolution of collisionless magnetized plasma. Unfortunately, the kinetic Vlasov equation is very difficult to solve analytically or numerically. The system intractability is connected to various factors. First of all, it is a time dependent system of partial differential equations which describes the evolution of six-dimensional phase space. This fact implies that high computational resources are required to resolve the system. Kinetic equation is also highly nonlinear meaning that it can lead to turbulence and chaos. Such solutions usually need high resolution. Moreover, collisionless magnetized plasma is characterized by large number of very different time and space scales making the system of equations very stiff. For example, light electrons respond to perturbations much faster then heavy ions. In the presence of a strong magnetic field it is common to have huge anisotropy along and across the magnetic field which also makes the problem stiff.

There are a lot of different numerical methods to solve Vlasov-Maxwell system. One of the main distinctions between them is the approach to treat the phase space. Probably the most popular method is particle-in-cell (PIC) method (Birdsall and Langdon, 2004) where phase space is discretized with macro-particles. The PIC method is very robust and it can be efficiently parallelized. Another common approach is Eulerian Vlasov (Cheng and Knorr, 1976; Sonnendrcker et al., 1999; Filbet et al., 2001), where phase space is discretized with stationary computational grid. Third

Email address: koshkarov.alexandr@usask.ca (Oleksandr Koshkarov)

method is spectral (Armstrong et al., 1970; Shoucri and Gagne, 1976; Holloway, 1996; Schumer and Holloway, 1998). Spectral methods handle the phase space by expanding distribution function in basis functions. The proper choice of functions can dramatically improve efficiency of the method.
The numerical methods discussed above have another important direction of classification — time discretization. Explicit methods are the simplest ones. Unfortunately, they suffer form various numerical stability constrains. Recently, fully implicit methods are getting more popularity in kinetic simulations due to their unconditional stability and ability to exactly satisfy physical conservation laws. For example, see recent papers for conservative implicit PIC (Lapenta et al., 2010; Chen et al., 2011) or spectral methods (Delzanno, 2015; Vencels et al., 2015; Manzini et al., 2016; Camporeale et al., 2016).
The main goal of this work is to construct and investigate a new hybrid method which is based on combining PIC and spectral methods. The main idea is to divide distribution function in the velocity space into two regions and resolve one part with macro-particles and another with basis function expansion. The PIC noise decreases as $\sim 1/\sqrt{N_p}$ where N_p is a number of macro-particles, thus it becomes computationally expensive to obtain high accuracy. So one of the targeted results is to improve accuracy of PIC by resolving the part of distribution function with spectral approach. On the other hand, spectral method may require high number of expansion functions (and computational time) to handle complex part of distribution function, therefore treating complex part with macro-particles may boost the performance. To the best of the authors knowledge, PIC and spectral coupling was never done before. Thus it is important to investigate properties and merits of the new method.
The paper is organized as follows: Section 2 introduces the main equations and a mathematical formulation of the new method. Landau damping benchmark is shown in Section 3. The comparison of new numerical method against pure spectral approach is conducted in Section 4. Finally, Section 5 summarizes results.

2. Method description

We will demonstrate the hybrid method with the example of one-dimensional electrostatic unmagnetized plasma. Thus the Vlasov-Maxwell system takes the form,

$$\partial_t f^s + v\partial_x f^s + \frac{q^s}{m^s} E \partial_v f^s = 0, \tag{1}$$

$$\partial_x E = \sum_s q^s \int_{-\infty}^{+\infty} f^s dv, \tag{2}$$

where s superscript denotes a species (e.g. electrons, ions, etc.); t, x, v are time, space and velocity variables respectively; $f^s = f^s(t, x, v)$ is the distribution function; q^s, m^s are charge and mass; E is the electric field. All variables are dimensionless and the normalization units defined as

$$t = t^d \omega_{pe}, \qquad x = \frac{x^d}{\lambda_D}, \qquad E = \frac{e\lambda_D}{T_e} E^d, \qquad f = \left(\frac{T_e}{m_e}\right)^{3/2} \frac{f^d}{n_0}, \qquad q = \frac{q^d}{e}, \qquad m = \frac{m^d}{m_e}, \tag{3}$$

with periodic boundary conditions

$$f^s(t, 0, v) = f^s(t, L, v), \quad E(t, 0) = E(t, L), \quad f^s(t, x, \pm\infty) = 0, \tag{4}$$

where d superscript denotes dimensional variables; ω_{pe} is the plasma frequency; λ_D is the Debye length; n_0 is the plasma density; L is the domain length; e, m_e, T_e are electron charge, mass and temperature, respectively.
To begin the formulation of the hybrid method, we write the distribution function f^s for each species s in the form

$$f^s = f^s_{spectral} + f^s_{particle}, \tag{5}$$

meaning that we solve two instances of Eq. (1) separately for $f^s_{spectral}$ and $f^s_{particle}$ with the common electric field which depends on the sum of all distribution functions. We solve one instance with the spectral method and another with the PIC method. To simplify notations, we will move the separation (5) into the species superscript. This means that we are solving the system (1-2) for s = spectral electrons, particle electrons, spectral ions, particle ions, etc. We also introduce superscripts for spectral and PIC part only: ss and ps respectively.
Note that nonlinear partial differential equations (PDE) generally do not permit the separation (5) because a sum of two PDE solutions may not be a solution. In our case this separation is possible if we keep a common electric field.

2.1. PIC

In particle-in-cell method we solve the Eq. (1) in the Lagrangina reference frame by following the characteristics of the macro-particles. In this frame the distribution function is always constant. Thus we only need to follow the frame evolution. Following Birdsall and Langdon (2004), for electrostatic momentum conserving explicit PIC we have the following equations

$$\frac{dx_i^{ps}}{dt} = v_i^{ps} \tag{6}$$

$$\frac{dv_i^{ps}}{dt} = \frac{q^{ps}}{m^{ps}} E^{local}(x_i^{ps}) \tag{7}$$

$$E^{local}(x_i^{ps}) = \sum_{j=0}^{N_x-1} E_j S(x_j - x_i^{ps}) \tag{8}$$

where $i = (1, \ldots, N_p)$ and N_p is the number of macro-particles; x_i^{ps}, v_i^{ps} are position and velocity of a macro-particle i; q^{ps}, m^{ps} are charge and mass of a species ps; $E_j, E^{local}(x_i^{ps})$ are the electric field at the grid point x_j and particle position x_i^{ps} respectively; S is the interpolation function; N_x is the number of grid points.
To compute the electric field at the grid point we would need the charge density which is

$$\rho_j = \sum_{ps} \sum_{i=1}^{N_p} q^{ps} S(x_j - x_i^{ps}). \tag{9}$$

2.2. Spectral method

There are a lot of different spectral methods (David Gottlieb, 1977) some of which are specifically designed to solve kinetic equation (Armstrong et al., 1970; Shoucri and Gagne, 1976; Holloway, 1996; Schumer and Holloway, 1998). Here we closely follow the approach taken by Delzanno (2015). Therefore, to solve Eq. (1), we approximate the distribution function and the electric field with the expansion

$$f^{ss}(t, x, v) = \sum_{n=0}^{N_v-1} \sum_{k=-N_k}^{N_k} C_{n,k}^{ss}(t) \Psi_n(\xi^{ss}) \exp\left(2\pi i \frac{kx}{L}\right), \tag{10}$$

$$E(x) = \sum_{k=-N_k}^{N_k} E_k \exp\left(2\pi i \frac{kx}{L}\right), \tag{11}$$

where N_k is the number of spacial Fourier modes defined to satisfy $N_x = 2N_k + 1$; N_v is the number of Hermite modes; $\xi^{ss} = (v - u^{ss})/\alpha^{ss}$ with free parameters u^{ss}, α^{ss} which affect convergence of the spectral method. The expansion functions in velocity space are defined as

$$\Psi_n(\xi) = \Psi^n(\xi) = \frac{\pi^{-1/4}}{\sqrt{2^n n!}} H_n(\xi) \exp\left(-\frac{\xi^2}{2}\right), \tag{12}$$

where $H_n(\xi)$ is a Hermite polynomial of degree n in ξ with the definition

$$H_0(\xi) = 1, \quad H_1(\xi) = 2\xi, \quad \xi H_n(\xi) = \frac{1}{2} H_{n+1}(\xi) + n H_{n-1}(\xi). \tag{13}$$

The final step is to use the orthogonality of Hermite and Fourier basis

$$\int_{-\infty}^{+\infty} \Psi_n(\xi) \Psi^m(\xi) d\xi = \delta_{n,m}, \tag{14}$$

$$\int_0^L \exp\left(2\pi i x \frac{n-m}{L}\right) dx = \delta_{n,m}. \tag{15}$$

The orthogonality gives us final system of equations

$$\frac{dC^{ss}_{n,k}}{dt} = -\alpha^{ss}\frac{2\pi i k}{L}\left(\sqrt{\frac{n}{2}}C^{ss}_{n-1,k} + \frac{u^{ss}}{\alpha^{ss}}C^{ss}_{n,k} + \sqrt{\frac{n+1}{2}}C^{ss}_{n+1,k}\right) + \frac{q^{ss}}{m^{ss}\alpha^{ss}}\left[E_* * \left(-\sqrt{\frac{n}{2}}C^{ss}_{n-1,*} + \sqrt{\frac{n+1}{2}}C^{ss}_{n+1,*}\right)\right]_k \quad (16)$$

where $n = (0, \dots, N_v - 1)$; $k = (-N_k, \dots, N_k)$ and the convolution is defined as

$$[A_* * B_*]_k = \sum_{k'=-N_k}^{N_k} A_{k-k'}B_{k'}. \quad (17)$$

2.3. Hybrid

Finally, the hybrid method comprises the PIC and spectral parts, coupled by the solution of Poisson's equation (2) including all contributions to the plasma density. The field equation is also solved with spectral method using the expansion (11) and the orthogonality condition (15), therefore

$$E(x_j) = \sum_{k=-N_k}^{N_k} E_k \exp\left(2\pi i \frac{k x_j}{L}\right), \quad (18)$$

$$E_k = \frac{L}{2\pi i k}\left(\sum_{ss} q^{ss}\alpha^{ss}\sum_{n=0}^{N_v-1} h_n C^{ss}_{n,k} + \rho_k\right), \quad (19)$$

$$\rho_k = \frac{1}{N_x}\sum_{j=0}^{N_x-1}\rho_j \exp\left(-2\pi i \frac{k x_j}{L}\right), \quad (20)$$

where

$$h_n = 0, \qquad \text{for odd n,} \quad (21)$$

$$h_n = \frac{\sqrt{2\pi}}{\pi^{1/4}}\left(\frac{1}{(n/2)!}\sqrt{\frac{n!}{2^n}}\right), \qquad \text{for even n.} \quad (22)$$

Thus the system of equations (6,7,16) with binding equations (8,9,19,18,20) is a system of time dependent ordinary differential equations which can be integrated, for example, with family of Runge-Kutta methods.

3. Landau damping benchmark

To investigate the properties of the new hybrid method a numerical code was developed. However, before proceeding with study, the correctness of the code must be verified. In this section, the ability of the code to reproduce the Landau damping is demonstrated.

Landau damping is a collisionless/entropy conserving damping of electrostatic waves in plasma. It is described by the dispersion equation (Landau, 1946)

$$1 + k^2 + \frac{\omega}{2k}Z\left(\frac{\omega}{2k}\right) = 0. \quad (23)$$

where the normalization corresponds to (3); ω is the frequency; k is the wave vector; $Z(z) = \pi^{-1/2}\int_{-\infty}^{+\infty} e^{t^2}dt/(t-z)$ is the dispersion plasma function.

To benchmark the numerical code we measure the damping rate of electrostatic wave in the simplest scenario: quasineutral plasma of two species — electrons and hydrogen ions with temperature of T_e and T_i respectively. In order to compare numerical and theoretical damping rates, a particular mode is excited to observe its evolution. We choose $k = 0.5$. The analytical solution of Eq. (23) for this k is $\mathrm{Re}(\omega) = 1.414$ and $\mathrm{Im}(\omega) = 0.154$.

The Landau damping occurs on the time scales where the ion dynamics is negligible in comparison to the electron

dynamics. Thus, to check the PIC and the spectral part of the code separately, we conduct two separate tests: (a) electrons are resolved with the spectral part of the code and ions with the PIC part; (b) electrons are resolved with the PIC part of the code and ions with the spectral part. The results of the simulations are shown in Figure 1 where we can clearly see that electrostatic wave damps according to the theoretical prediction. We also can see that the spectral part of the code Figure 1(a) is more precise than the PIC part Figure 1(b) for the relatively similar resolution (the computation time is similar).

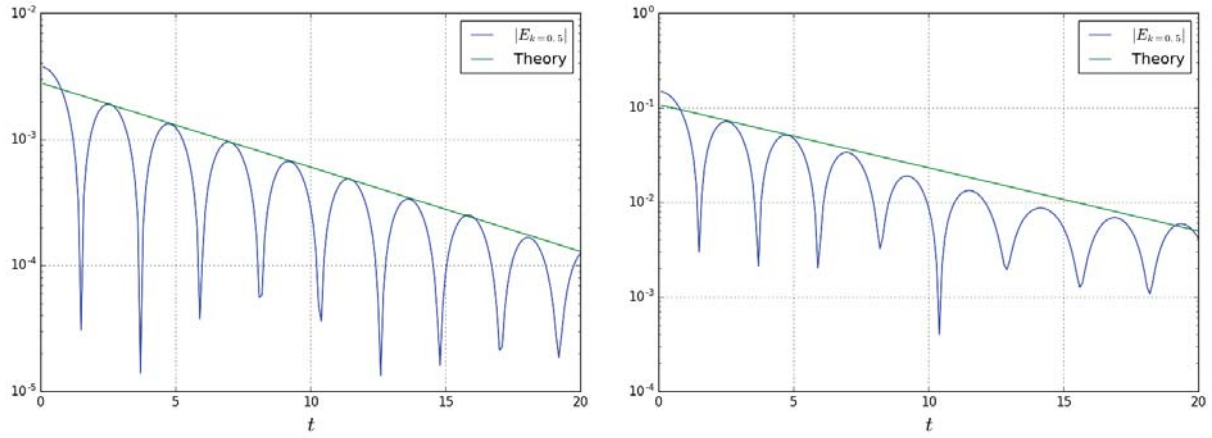

(a) electrons — spectral, ions — PIC

(b) electrons —PIC, ions — spectral

Figure 1: Ladau damping benchmark

4. Weak beam-plasma interaction problem

In this section the capabilities of the new hybrid method are demonstrated on a classical problem — interaction of a weak electron beam with plasma. This problem is very challenging for the pure PIC method (Ratcliffe et al., 2014) because the required resolution and characteristic evolution time are increasing with the weaker beam density. During the beam-plasma interaction, the electron distribution function forms a plateau in the velocity space. Therefore, a pure spectral method requires a high number of expansion functions to capture the correct dynamics. In order to improve performance, the hybrid method treats the bulk plasma with spectral method and the beam with macro-particles.
The following simulation parameters with normalization (3) are used:

- 3 species — ions (with mass 1836), background electrons and beam electrons
- Domain length is 2048 with periodic boundary conditions
- Electron beam mean velocity is 10
- Electron bulk and beam thermal velocities are 1
- Ion thermal velocity is $1/\sqrt{10 \cdot 1836}$
- Beam density is 10^{-2}

The hybrid and spectral codes use the same

- initial condition shown in Figure 2
- time discretization (Runge-Kutta 4)
- spectral discretization of plasma bulk with 51 Hermite polynomials

At the same time, they resolve electron beam differently

- Hybrid code uses macro-particles with different number of particle per cell (ppc)
- Spectral code uses the expansion with different number of Hermite polynomials N_v

After some time the electron distribution function flattens to form a plateau which is shown in Figure 3. One can see that spectral and hybrid codes converge to the same solution. To quantify the accuracy, we define an error

$$\epsilon(t) = \frac{\int \left| f(t,x,v) - f_{ref}(t,x,v) \right| dxdv}{\int |f_{ref}(t,x,v)| dxdv} \cdot 100\% \tag{24}$$

where f_{ref} is the reference solution which is obtained by a spectral method solution with high number of Hermite polynomials $N_v = 1601$ for the beam and $N_v = 51$ for the bulk. Results are listed in Tables 1,2.

Ppc	Simulation time (s)	$\epsilon(100)$ (%)	$\epsilon(200)$ (%)
10^1	1207	0.232	0.308
10^2	1459	0.226	0.327
10^3	3906	0.119	0.416
10^4	31425	0.123	0.128

Table 1: Hybrid method performance

N_v	Simulation time (s)	$\epsilon(100)$ (%)	$\epsilon(200)$ (%)
51	1794	0.501	2.674
101	2364	0.072	0.347
201	3703	0.013	0.043
401	5987	0.004	0.017

Table 2: Spectral method performance

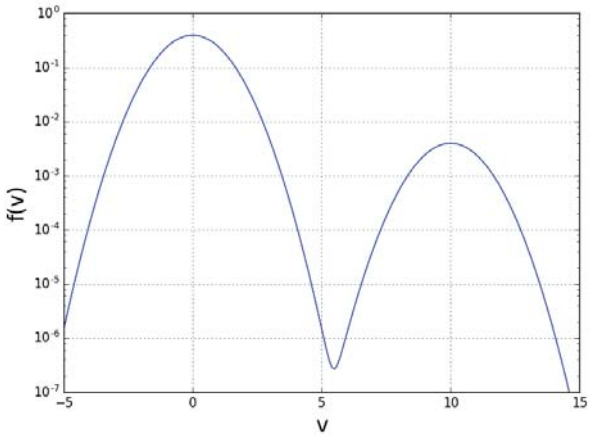

Figure 2: Initial condition for electron distribution function for the beam-plasma problem.

5. Discussion and Conclusion

In this letter, the new hybrid method to solve Vlasov-Maxwell system was described. The new key concept is to resolve one part of the velocity space with macro-particles and another with the spectral expansion. This approach gives more flexibility to balance between accuracy and computational load in comparison to pure PIC and spectral methods.

The numerical method was implemented and benchmarked with Landau damping problem. The benchmark revealed that the code can reproduce the correct damping rate either with the PIC or with the spectral part.

Next the new method was applied to the problem of weak electron-beam plasma interaction. This problem combines phenomena with different time scales. The essential part of the beam instability is Landau resonance which is responsible for production and absorption of Langmuir waves. Therefore, the plasma frequency, electron time scales, should

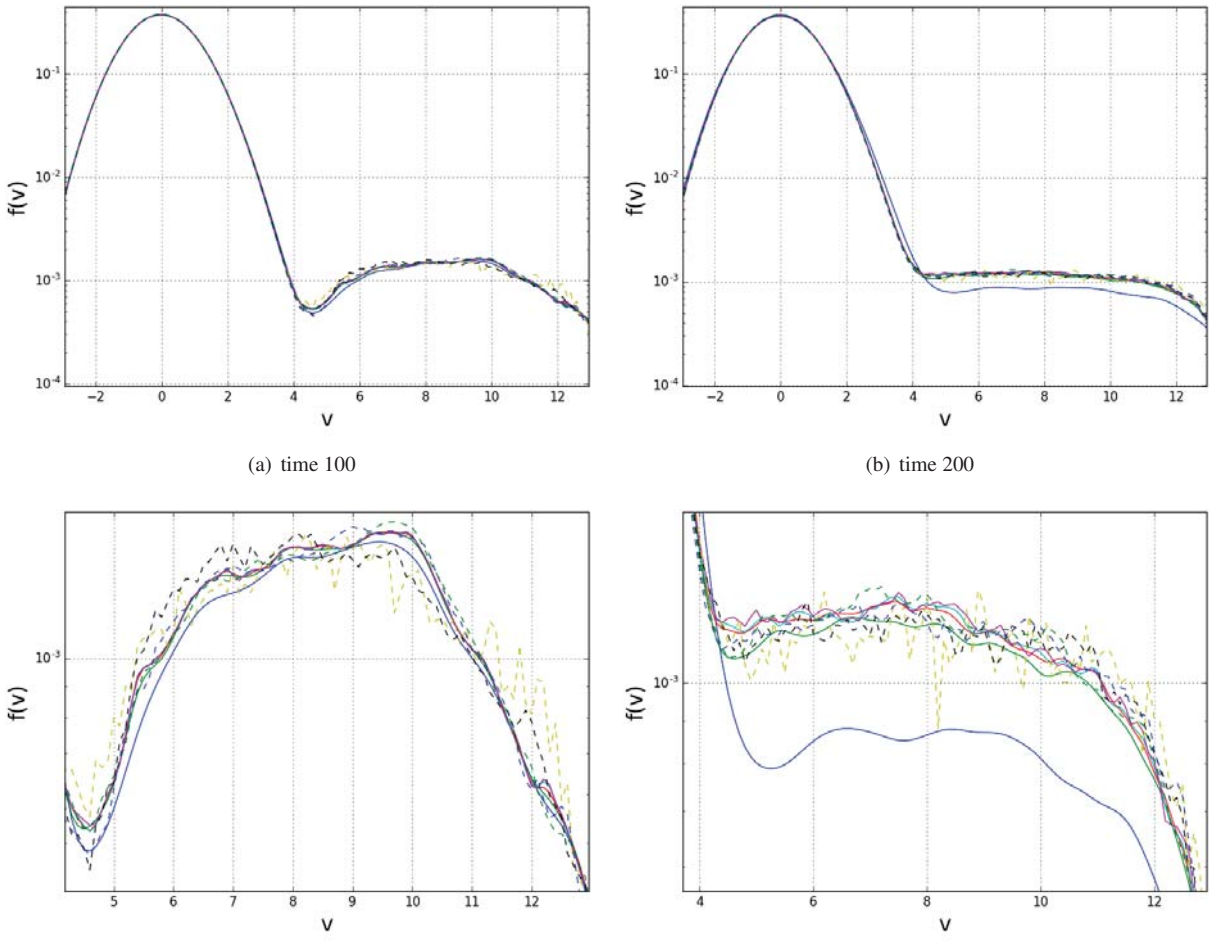

(a) time 100

(b) time 200

(c) amplified Figure 3(a)

(d) amplified Figure 3(b)

(e) Common legend

Figure 3: Electron distribution function for hybrid and spectral methods for times 100 and 200

be resolved. On the other hand, to capture the correct dynamics, one needs to consider a nonlinear wave interaction between Langmuir waves and the ion sound which happens on ion time scales. Thereby, the combination of different time scales makes this problem challenging for computational physics.

The results (Tables 1,2) show that sufficiently small error could be obtained by discretizing the electron beam with small number of macro-particles ($10 - 100$ ppc). To obtain similar error with the pure spectral method, one needs to use $\sim$ 100 polynomials which is computationally more expansive. The difference in performance may be more prominent in 3-dimensional case.

It is important to note, that comparison of numerical methods is extremely difficult task. For instance, the error definition (24) uses the pure spectral method as a reference solution. This fact makes it difficult to reason about hybrid method convergence. Thus, one needs to investigate further the correct measure of the error.

References

Armstrong, T.P., Harding, R.C., Knorr, G., Montgomery, D., 1970. Solution of Vlasov's equation by transform methods. Methods in Computational Physics 9, 29–86.

Birdsall, C.K., Langdon, A.B., 2004. Plasma Physics via Computer Simulation. CRC Press.

Camporeale, E., Delzanno, G., Bergen, B., Moulton, J., 2016. On the velocity space discretization for the vlasovpoisson system: Comparison between implicit hermite spectral and particle-in-cell methods. Computer Physics Communications 198, 47 – 58.

Chen, G., Chacn, L., Barnes, D.C., 2011. An energy- and charge-conserving, implicit, electrostatic particle-in-cell algorithm. Journal of Computational Physics 230, 7018 – 7036.

Cheng, C.Z., Knorr, G., 1976. The integration of the Vlasov equation in configuration space. Journal of Computational Physics 22, 330 – 351.

David Gottlieb, S.A.O., 1977. Numerical Analysis of Spectral Methods : Theory and Applications. SIAM.

Delzanno, G., 2015. Multi-dimensional, fully-implicit, spectral method for the vlasovmaxwell equations with exact conservation laws in discrete form. Journal of Computational Physics 301, 338 – 356.

Filbet, F., Sonnendrcker, E., Bertrand, P., 2001. Conservative Numerical Schemes for the Vlasov Equation. Journal of Computational Physics 172, 166 – 187.

Holloway, J.P., 1996. Spectral velocity discretizations for the Vlasov-Maxwell equations. Transport theory and statistical physics 25, 1–32.

Landau, L.D., 1946. On the vibrations of the electronic plasma. J. Phys. (USSR) 10, 96–117.

Lapenta, G., Markidis, S., Divin, A., Goldman, M., Newman, D., 2010. Scales of guide field reconnection at the hydrogen mass ratio. Physics of Plasmas 17.

Manzini, G., Delzanno, G., Vencels, J., Markidis, S., 2016. A legendrefourier spectral method with exact conservation laws for the vlasovpoisson system. Journal of Computational Physics 317, 82 – 107.

Ratcliffe, H., Brady, C.S., Che Rozenan, M.B., Nakariakov, V.M., 2014. A comparison of weak-turbulence and particle-in-cell simulations of weak electron-beam plasma interaction. Physics of Plasmas 21.

Schumer, J.W., Holloway, J.P., 1998. Vlasov Simulations Using Velocity-Scaled Hermite Representations. Journal of Computational Physics 144, 626 – 661.

Shoucri, M., Gagne, R.R.J., 1976. Numerical solution of the vlasov equation by transform methods. Journal of Computational Physics 21, 238 – 242.

Sonnendrcker, E., Roche, J., Bertrand, P., Ghizzo, A., 1999. The Semi-Lagrangian Method for the Numerical Resolution of the Vlasov Equation. Journal of Computational Physics 149, 201 – 220.

Vencels, J., Delzanno, G.L., Johnson, A., Peng, I.B., Laure, E., Markidis, S., 2015. Spectral solver for multi-scale plasma physics simulations with dynamically adaptive number of moments. Procedia Computer Science 51, 1148 – 1157.

Anomalous radial diffusion at low L shell due to the combined effects of drift-shell splitting and atmospheric pitch angle scattering

Vivien Loridan

CEA, DAM, DIF, F-91297 Arpajon, France.

Gregory S. Cunningham

Space Science and Applications, Los Alamos National Laboratory, Los Alamos, New Mexico, USA.

Jean-François Ripoll

CEA, DAM, DIF, F-91297 Arpajon, France.

Abstract

The Fokker-Planck equation governing the evolution of the phase-averaged electron distribution function in the radiation belts commonly involves a radial diffusion coefficient. Although the first expressions for the radial diffusion term have been derived a few decades ago, they are still being debated, until very recently. Most of these works put forward a radial diffusion coefficient induced by drift-resonant interactions between electrons and ultra low frequency (ULF) electromagnetic waves. The radial diffusion coefficient commonly increases as a power law with respect to the radial adiabatic invariant L^* and has been used to explain the evolution of electron flux in the slot region and in the outer belt. However, observations made in 1964 of the electron fluxes at low altitude indicated an empirical radial diffusion coefficient, which decreases strongly with increasing L^*. This sharp reversal behavior at L^* below 1.5 Earth radius differs strongly from the aforementioned expressions of the radial diffusion coefficient and suggests that other physical processes may impact the radial diffusion term. In this study, we propose a quantitative explanation for this additional radial diffusion occurring in the inner-belt, based on the combination of two different physical effects. The first effect is the drift-shell splitting of electrons, inherent to the asymmetries of the Earth magnetic field, even at very low L shells. The second phenomenon is atmospheric Coulomb scattering, which makes the electron diffuse in pitch angle. By quantifying and coupling both of these processes, we exhibit a radial diffusion term, which indeed decreases with increasing L^* and is in good agreement with the few empirical studies made in the late 60's.

Keywords: anomalous radial diffusion, drift-shell splitting, atmospheric pitch angle scattering

1. Introduction

The radial diffusion theory of magnetospheric particles often relies on a radial diffusion coefficient. This radial diffusion term has to be accurately calculated if one wants to predict the dynamics of trapped particles in the Earth magnetic field. Understanding such a process is crucial because when these particles diffuse radially inward, they gain energy and may cause damage to orbiting satellites.

As a quick fundamental review, a charged particle trapped in a magnetic field undergoes three types of motions. The first and quickest motion is the gyromotion of the particle around a field line, due to the

Email addresses: vivien.loridan@cea.fr (Vivien Loridan), cunning@lanl.gov (Gregory S. Cunningham), jean-francois.ripoll@cea.fr (Jean-François Ripoll)

Lorentz force, characterized by a frequency of several kHz. The second motion is the bounce motion of the particle along a field line, with a frequency of a few Hz. This back and forth motion between two mirror points is attributed to both the mirror force and the energy conservation of the particle along the field line. The third motion is the drift motion of the particle across field lines, at a frequency of some mHz, in response to the gradient and curvature of the magnetic field. A given adiabatic invariant is associated with each of these three periodic motions. Hence for a particle of rest mass m_0, momentum p and local pitch angle α (i.e. the angle between the electron momentum and the vector of the magnetic field), the first adiabatic invariant associated with the gyromotion is

$$\mu = \frac{p^2 \sin^2(\alpha)}{2m_0 B}$$

where B is the local magnetic field intensity. The second adiabatic invariant associated with the bounce motion is commonly

$$J = 2\int_{s_m}^{n_m} p\cos(\alpha)\mathrm{d}s = 2\int_{s_m}^{n_m} p\sqrt{1-\frac{B(s)}{B_m}}\mathrm{d}s$$

where s is the distance along the particle's bounce trajectory, from the south mirror s_m point to the north mirror n_m point. If the particle keeps its energy constant along a field line, one can also consider the invariant

$$K = \frac{\sqrt{B_m}}{2p}J = \int_{s_m}^{n_m}\sqrt{B_m - B(s)}\,\mathrm{d}s$$

where B_m is the intensity of the magnetic field at the mirror point of the particle. Then the third adiabatic invariant associated with the drift motion corresponds to the magnetic flux encompassed by the guiding drift shell of the particle

$$\Phi = \iint_{\Sigma} \mathbf{B}\cdot\mathrm{d}\mathbf{S},$$

where the integral is over the vector magnetic field $\mathbf{B}$ dot product with the surface element of the drift-shell $\mathrm{d}\mathbf{S}$. We can substitute the invariant coordinate Φ with the coordinate $L^* = 2\pi B_E R_E^2/\Phi$ (Roederer, 1970) where B_E is the value of the equatorial magnetic field at the Earth surface and R_E the Earth radius. For a pure dipole magnetic field, the L^* invariant coordinate is equal to the L shell parameter defined as $L = r_0/R_E$ where r_0 is the radius at the equatorial point of a field line. In what follows, we will use the L notation to refer to the equatorial radius of the field line at a fixed azimuth and the L^* notation to refer to the third adiabatic invariant.

A given adiabatic invariant can be violated when forces controlling the motion vary on a timescale comparable to or smaller than the associated period of motion. When all three adiabatic invariants are violated, the equation governing the phase-averaged particle distribution function f in the radiation belts is the Fokker-Planck equation, which is written in canonical form as (e.g., Schulz and Lanzerotti, 1974)

$$\frac{\partial f}{\partial t} = \sum_{i,j=1}^{3}\frac{\partial}{\partial J_i}\left[D_{J_iJ_j}\frac{\partial f}{\partial J_j}\right], \tag{1}$$

where $(J_1, J_2, J_3) \equiv (\mu, J, \Phi)$ and $D_{J_iJ_j}$ is the tensorial diffusion coefficient. Equation (1) can also be written in a more common form in terms of (μ, K, L^*) to yield

$$\frac{\partial f}{\partial t} = \sum_{i,j=1}^{3}\frac{1}{G}\frac{\partial}{\partial Q_i}\left[G\widetilde{D}_{Q_iQ_j}\frac{\partial f}{\partial Q_j}\right], \tag{2}$$

where $(Q_1, Q_2, Q_3) \equiv (\mu, K, L^*)$, G is the Jacobian of the transformation from (μ, J, Φ) to (μ, K, L^*) and $\widetilde{D}_{Q_iQ_j}$ are the new diffusion coefficients in the (μ, K, L^*) coordinate system. This equation can be hard to both

express mathematically and to solve numerically in the presence of a realistic Earth magnetic field (e.g., Cunningham, 2016).

The radial diffusion coefficient $\widetilde{D}_{L^*L^*}$ involved in (2) can be expressed from drift-resonant interactions between electrons and ultra low-frequency (ULF) electromagnetic waves at constant first and second adiabatic invariants (μ, K), but also from other processes as we show below. An expression for the radial diffusion coefficient $D^{\mathrm{ULF}}_{L^*L^*}$ for drift-resonant interactions between electrons and ULF electromagnetic waves was first investigated by Fälthammar (1965) and later extended by Schulz and Lanzerotti (1974). Based on satellite observations, Brautigam and Albert (2000) and Ozeke et al. (2014) assumed that the radial diffusion coefficient increases as a power law in L^*, as shown in Figure 1. All these expressions of the radial diffusion coefficient have been successfully used in many studies intended to describe the evolution of the electron phase space density in the slot region and in the outer radiation belt.

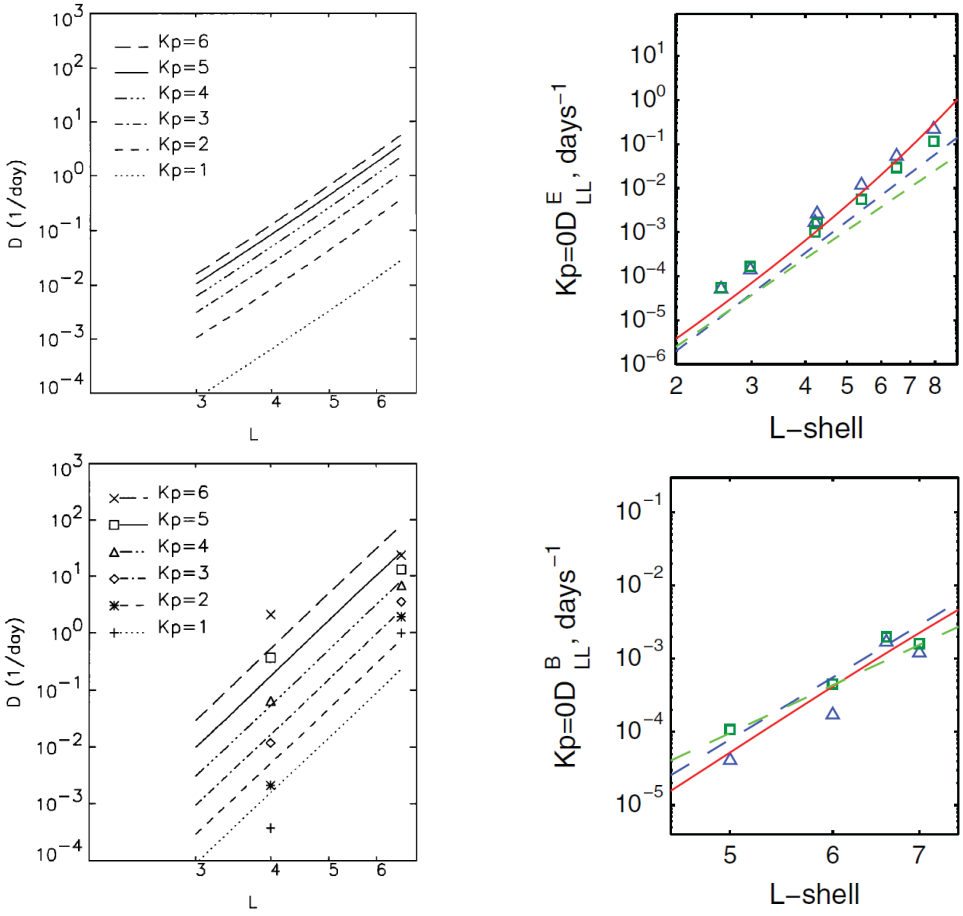

Figure 1: Evolution of the radial diffusion coefficient from drift-resonant interactions with ULF electromagnetic waves vs L^*. The electrostatic part $D^{E}_{L^*L^*}$ increases with L^{*6} for Brautigam and Albert (2000) (top-left) and Ozeke et al. (2014) (top-right). The electromagnetic part $D^{M}_{L^*L^*}$ increases with L^{*10} for Brautigam and Albert (2000) (bottom-left) and Ozeke et al. (2014) (bottom-right).

2. Evidence of anomalous radial diffusion

The power law dependence on L^* of the radial diffusion coefficient has, however, not been observed for $L^* < 1.5$. Newkirk and Walt (1968), and, then, Farley (1969), studied the electron flux in the upper atmosphere following the Starfish nuclear detonation in 1962. They realized that the decay rate of the

low L^* shell electrons was surprisingly much slower than what was predicted by the atmospheric scattering theory. This discrepancy between theory and observations was attributed to additional radial diffusion from an unknown process. Based on these observations, they empirically derived the expression for the radial diffusion coefficient in the narrow region $L^* < 1.5$, for a constant first adiabatic invariant and for equatorially mirroring particles (i.e. for $K = 0$). These studies both showed a surprising radial diffusion coefficient strongly decreasing with increasing L^*, as shown in Figure 2. The sharp reversal behavior of the radial diffusion coefficient at low L shell values compared with the radial diffusion coefficients represented in Figure 1 is characteristic of another physical process that adds to the interactions of electrons with ULF waves.

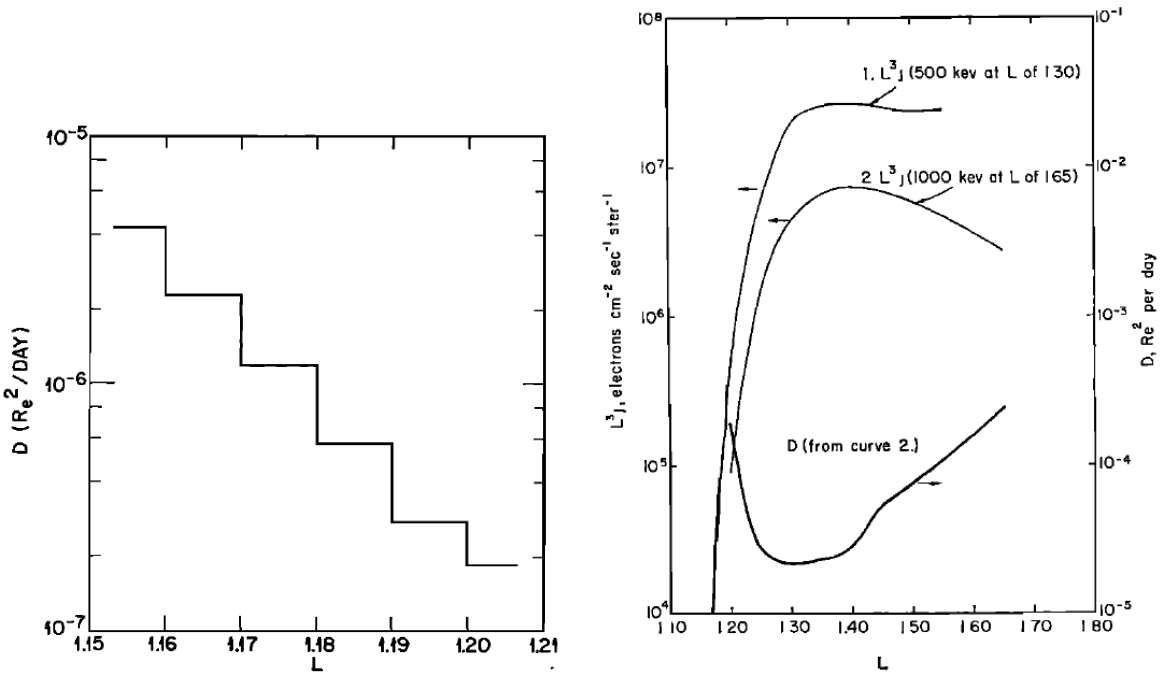

Figure 2: Evolution of the radial diffusion coefficient vs L^*, taken from Newkirk and Walt (1968) (left) and Farley (1969) (right, bottom curve, right axis), for $K \sim 0.0$. The electron energy studied by Newkirk and Walt (1968) is above 1.6 MeV, while Farley (1969) focused on electrons having an energy of 1 MeV at $L^* = 1.65$. We also notice that the values of the radial diffusion coefficient taken from Farley (1969) are two order of magnitude above the values obtained by Newkirk and Walt (1968). As mentioned by Walt (1971), this discrepancy is due to the fact that Farley (1969) took only into account the losses due to atmosphere collision, which makes his values an upper limit for the radial diffusion coefficient.

Roederer et al. (1973) interpreted this additional radial diffusion process as a consequence of two different physical phenomena, the drift shell splitting process and atmospheric scattering, as we will investigate in this work. The drift-shell splitting effect is due to the azimuthal asymmetry of the Earth magnetic field, which makes electrons of different equatorial pitch angle on the same field line populate different drift-shells. We expect the presence of the South Atlantic Anomaly (SAA) to contribute to significant drift shell splitting effect. At low L shells, electrons also experience atmospheric scattering and so diffuse in pitch angle. But as their pitch angles change, the asymmetry of the magnetic field makes them follow different drift-shells, and so make them diffuse radially.

Relying on their assumptions, we have to quantify an additional radial diffusion term at constant (μ, K), as observed by Newkirk and Walt (1968) and Farley (1969), due to drift-shell splitting associated to Coulomb collisions occurring at constant energy. We consider a situation in which the only interaction that occurs is pitch angle scattering from Coulomb collisions between electrons with ions and neutrals. Because the ions and neutrals are massive compared to the electron, the interaction is nearly elastic, i.e. the energy of the

electron is nearly constant. The diffusion tensor in the three adiabatic invariants (μ, K, L^*) related to the diffusion tensor expressed in (p, α_0, L), where α_0 is the equatorial pitch angle, takes the form (e.g., Roederer and Zhang, 2014)

$$\begin{pmatrix} D_{\mu\mu} & D_{\mu K} & D_{\mu L^*} \\ D_{\mu K} & D_{KK} & D_{KL^*} \\ D_{\mu L^*} & D_{KL^*} & \widetilde{D}_{L^*L^*} \end{pmatrix} = \begin{pmatrix} \frac{\partial \mu}{\partial p} & \frac{\partial \mu}{\partial \alpha_0} & 0 \\ 0 & \frac{\partial K}{\partial \alpha_0} & 0 \\ 0 & \frac{\partial L^*}{\partial \alpha_0} & \frac{\partial L^*}{\partial L} \end{pmatrix} \begin{pmatrix} 0 & 0 & 0 \\ 0 & D_{\alpha_0\alpha_0} & 0 \\ 0 & 0 & 0 \end{pmatrix} \begin{pmatrix} \frac{\partial \mu}{\partial p} & 0 & 0 \\ \frac{\partial \mu}{\partial \alpha_0} & \frac{\partial K}{\partial \alpha_0} & \frac{\partial L^*}{\partial \alpha_0} \\ 0 & 0 & \frac{\partial L^*}{\partial L} \end{pmatrix}.$$

The differential terms $\partial\mu/\partial L$, $\partial K/\partial p$, $\partial K/\partial L$ and $\partial L/\partial p$ are zero by definition. The $D_{\alpha_0\alpha_0}$ term is the pitch angle diffusion coefficient for Coulomb collisions between electrons with ions and neutrals. The cross-diffusion terms D_{pL} and $D_{\alpha_0 L}$ are zero because the particle does not change its energy and does not move off that field line at the azimuth where the pitch angle diffusion occurs. Here we get

$$\widetilde{D}_{L^*L^*} = \left(\frac{\partial L^*}{\partial \alpha_0}\right)^2 D_{\alpha_0\alpha_0}.$$

If we now take account of the common radial diffusion induced by drift-resonant interactions between electrons and ultra low-frequency (ULF) electromagnetic waves at (μ, K), the full diffusion tensor becomes

$$\begin{pmatrix} D_{\mu\mu} & D_{\mu K} & D_{\mu L^*} \\ D_{\mu K} & D_{KK} & D_{KL^*} \\ D_{\mu L^*} & D_{KL^*} & \widetilde{D}_{L^*L^*} \end{pmatrix} = \begin{pmatrix} \frac{\partial \mu}{\partial p} & \frac{\partial \mu}{\partial \alpha_0} & 0 \\ 0 & \frac{\partial K}{\partial \alpha_0} & 0 \\ 0 & \frac{\partial L^*}{\partial \alpha_0} & \frac{\partial L^*}{\partial L} \end{pmatrix} \begin{pmatrix} 0 & 0 & 0 \\ 0 & D_{\alpha_0\alpha_0} & 0 \\ 0 & 0 & 0 \end{pmatrix} \begin{pmatrix} \frac{\partial \mu}{\partial p} & 0 & 0 \\ \frac{\partial \mu}{\partial \alpha_0} & \frac{\partial K}{\partial \alpha_0} & \frac{\partial L^*}{\partial \alpha_0} \\ 0 & 0 & \frac{\partial L^*}{\partial L} \end{pmatrix} + \begin{pmatrix} 0 & 0 & 0 \\ 0 & 0 & 0 \\ 0 & 0 & D^{\mathrm{ULF}}_{L^*L^*} \end{pmatrix}.$$

For an axisymmetric magnetic field (such as a dipole field), L^* does not depend on the equatorial pitch angle, and so the drift-shell splitting term $\partial L^*/\partial\alpha_0$ is zero, leading to $\widetilde{D}_{L^*L^*} = D^{\mathrm{ULF}}_{L^*L^*}$. However, if the magnetic field is more realistically considered as asymmetric, the drift-shell splitting term is nonzero and we obtain from above

$$\widetilde{D}_{L^*L^*} = D^{\mathrm{ULF}}_{L^*L^*} + \left(\frac{\partial L^*}{\partial \alpha_0}\right)^2 D_{\alpha_0\alpha_0}. \tag{3}$$

As mentioned by O'Brien (2015), an anomalous radial diffusion term $(\partial L^*/\partial\alpha_0)^2 D_{\alpha_0\alpha_0}$ appears as we have changed the system of coordinates, highlighting the impact of both processes of drift-shell splitting $(\partial L^*/\partial\alpha_0)$ and pitch angle diffusion $(D_{\alpha_0\alpha_0})$. It is important to note that the off-diagonal terms are not zero in the diffusion tensor in the left-hand side above because a change in α_0 also changes μ and K as well as L^*. For this reason, the anomalous radial diffusion cannot be accurately modeled as a one dimensional diffusion in L^* at fixed (μ, K), but rather the full equation (2) must be used.

3. Drift-shell splitting effects

The first step of the study is to compute accurately the drift-shell splitting term $\partial L^*/\partial\alpha_0$ representing the effect of drift-shell splitting due to the asymmetries of the magnetic field, represented by the IGRF model in our study. The key point of the derivation is the correspondence between the adiabatic coordinates (L^*, K, φ) with the geometric coordinates (r, α_0, φ), where r is the radius position of the particle and φ is the azimuth of the particle, both taken in the Geocentric Solar Magnetospheric (GSM) coordinates. Starting from a given numerical grid in (L^*_i, K_j, φ_k) with $i \in [1, 100]$, $j \in [1, 100]$ and $k \in [1, 24]$, we use the approach in (Cunningham, 2016) to compute the corresponding coordinate $(r_{i,j,k}, \alpha_{0i,j,k}, \varphi_{i,j,k})$ populated by

the particle. Then, any coordinate (r, α_0, φ) can be associated with a specific drift-shell using the reference set $(r_{i,j,k}, \alpha_{0i,j,k}, \varphi_{i,j,k})$ by linear interpolation. These linear interpolations are used to extract the new set (L^*, K, φ) corresponding to any arbitrary coordinate (r, α_0, φ). Hence, keeping both the reference radius $r_{i,j,k}$ and longitude $\varphi_{i,j,k}$ constant, and adding a slight change $\delta\alpha_0$ to $\alpha_{0i,j,k}$ enables us to find the corresponding $L^*_i + \delta L^*_{i,j,k}$, where $\delta L^*_{i,j,k}$ is the change of the radial invariant due to the variation in equatorial pitch angle. The desired quantity $\delta L^*/\delta\alpha_0$, as a function of (L^*, K, φ), is finally deduced.

The first challenge arising from this methodology is how to choose the best $\delta\alpha_0$ to represent the derivative of L^* with respect to α_0. As a matter of fact, if the $\delta\alpha_0$ parameter is too small, the numerical $\delta L^*/\delta\alpha_0$ is zero, and if $\delta\alpha_0$ is too large, we lose the mathematical meaning of the derivative of a function at any given point. To deal with such a problem, we compute the values of the radial invariant $L^*_i + \delta L^*_{i,j,k}$ corresponding to the equatorial pitch angle $\alpha_{0i,j,k} + \delta\alpha_0$, for several values of $\delta\alpha_0$, at fixed radius and longitude. This step gives us a L^* function evolving with respect to α_0. We then apply several spline interpolations of the L^* function over points separated by different $\delta\alpha_0$ values. Figure 3 (left) shows the differences occurring on the slope of L^* with respect to equatorial pitch angle according to the chosen interpolated points. The $\delta L^*/\delta\alpha_0$ function evolving with the $\delta\alpha_0$ parameter is thus created. From that, a region where $\delta L^*/\delta\alpha_0$ is approximately constant with respect to $\delta\alpha_0$ should emerge. This plateau region gives us an admissible range for $\delta\alpha_0$. From our study, we conclude that $\delta\alpha_0$ = 0.03 radians (i.e. $\delta\alpha_0 \sim 1.8°$) is a good value that gives an accurate derivative of L^* with respect to the equatorial pitch angle to quantify the drift-shell splitting effect. Figure 3 (right) illustrates the difficulty of finding an admissible range of $\delta\alpha_0$ to accurately compute $\delta L^*/\delta\alpha_0$. This step has to be improved in a future work.

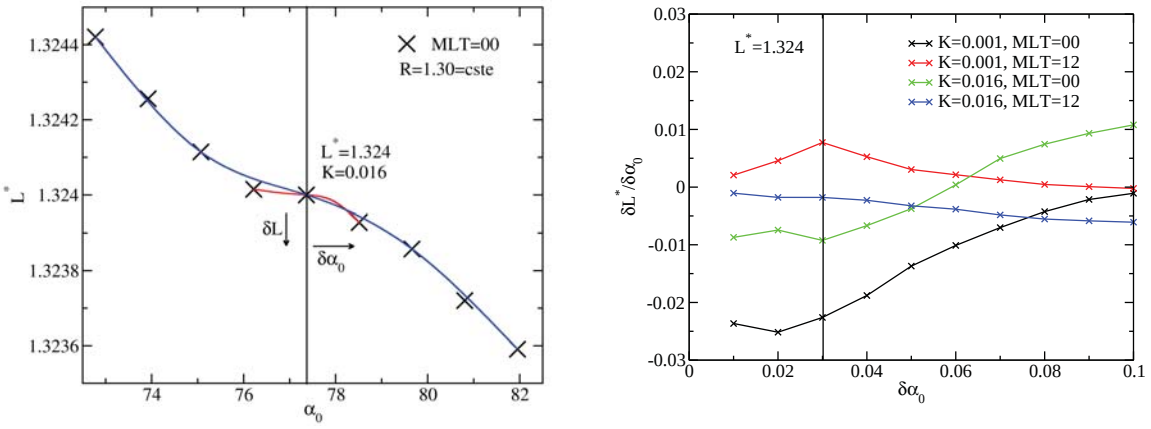

Figure 3: Effects of spline interpolations on the value of $\delta L^*/\delta\alpha_0$ (left). The red curve corresponds to the spline interpolation on all the available points in L^*. Hence the local slope value of the function is close to zero. As for the blue curve, the interpolation is made on one point over two. The slope is in this case clearly negative. The right panel shows the evolution of $\delta L^*/\delta\alpha_0$ vs $\delta\alpha_0$ for a fixed L^*,K and φ. A plateau region hardly emerges around $\delta\alpha_0$ = 0.03, highlighting the difficulty of finding a single $\delta\alpha_0$ value for all cases.

From this method, we are able to compute the drift-shell splitting quantity $\delta L^*/\delta\alpha_0$ for any given (L^*,K,φ). Our numerical study leads us to a drift-shell splitting term $\delta L^*/\delta\alpha_0$ of about 10^{-2} Earth radius per radian. The evolution of the $\delta L^*/\delta\alpha_0$ function with L^*, at a given K and φ, is characterized by many oscillations. We think this behavior is due to the spherical harmonics expansion in the IGRF magnetic field model. A spline regression can be done to get the global trend of the $\delta L^*/\delta\alpha_0$ function.

4. Atmospheric Coulomb scattering effects

To quantify the effects due to atmospheric pitch angle scattering from Coulomb collisions of electrons with ions and neutrals, we use the pitch angle diffusion coefficient formulation of Selesnick (2012) given by

$$D_{xx} = \frac{2\pi r_e^2 m_0^3 c^4 y^2 \gamma}{p^3 x^3} \left\langle \left(\frac{B_0}{B} - y^2 \right) \left[n_e \lambda_e + \sum_i n_i Q_i^2 \left(\lambda_p - \lambda_{ni} \right) + \sum_j n_j Z_j^2 \lambda_{n_j} \right] \right\rangle_b \tag{4}$$

where $x = \cos(\alpha_0)$, $y = \sin(\alpha_0)$. The parameter $r_e = e^2/(4\pi\epsilon_0 m_0 c^2)$ is the classical electron radius and γ the Lorentz factor related to the local electron velocity v. The densities n_j of the neutral species (He, O, N2, O2, Ar, H and N) are given by the MSIS model, which is included in the LANL-GeoMag library. n_e is the electron number density and n_i is the ion number density. Q_i and Z_j are respectively the charge state of the ion i and the atomic number of the neutral species j. For the purpose of this study, we intentionally do not take the ion number density into account. This step can be done in a future work. Given the Debye length $\lambda_D = \sqrt{kT/(8\pi n_e e^2)}$ and the reduced mass $m_r = m_0/2$, we have $\lambda_{e/p} = \ln\left[(m_r v \lambda_D)/\hbar\right]$ and $\lambda_{ni} = \ln\left[\beta\gamma/\left(2.05\alpha_f Z_i^{1/3}\right)\right]$ with $\beta = v/c$ and $\alpha_f = 1/137$, the fine structure constant. As before, B is the intensity of the local magnetic field and B_0 is the equatorial magnetic field intensity. In order to compute the pitch angle diffusion coefficient in a non-dipole magnetic field, we have first to compute the local diffusion coefficient at each point of a given field line, and then apply the integration over each bounce path, as in (Selesnick, 2012)

$$\langle .. \rangle_b = \frac{1}{S_b} \int_{s_m}^{n_m} \frac{..}{\cos(\alpha)} \mathrm{d}s$$

where B is the local magnetic field intensity given by the IGRF magnetic field model and S_b is the half-bounce path length. The x diffusion coefficient is converted into the needed pitch angle diffusion coefficient by the relation $D_{\alpha\alpha_0} = D_{xx}/y^2$. In this work, we focus on the particular date of October 8, 1964. The $F_{10.7}$ parameter used in the MSIS density model has been set to 100. Figure 4 shows the evolution of the longitude-averaged pitch angle diffusion coefficient $D_{\alpha\alpha_0}$ with respect to the equatorial pitch angle α_0. The global trend of the obtained curves can be compared with Figure 6 from Selesnick et al. (2013) that represents the pitch angle diffusion coefficient (but not averaged over longitude) with respect to the equatorial pitch angle α_0.

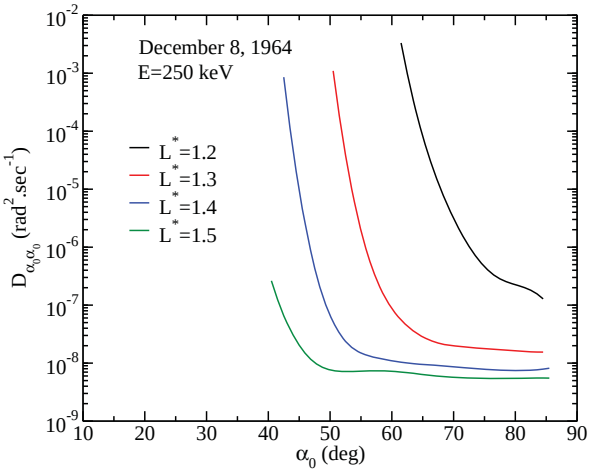

Figure 4: Evolution of the longitude-averaged pitch angle diffusion coefficient $D_{\alpha\alpha_0}$ vs α_0 for $E = 250$ keV and for $L^* = 1.2, 1.3, 1.4$ and 1.5.

5. Quantification of anomalous radial diffusion

5.1. Results

The final anomalous radial diffusion term $D^A_{L^*L^*}$ due to drift-shell splitting and pitch angle scattering is

$$D^A_{L^*L^*} = \left\langle \left(\frac{\partial L^*}{\partial \alpha_0} \right)^2 D_{\alpha_0 \alpha_0} \right\rangle_\varphi$$

where $\langle .. \rangle_\varphi$ is the average over all Magnetic Local Time (MLT). In the present work, we use a spline regression on the $D^A_{L^*L^*}$ function in order to capture its global trend and to avoid non-physical noise that goes along the calculation of the $\delta L^*/\delta\alpha_0$ term. The evolution of the anomalous radial diffusion coefficient $D^A_{L^*L^*}$ with respect to L^* is represented below in Figure 5, for $K = 0.01$ (nearly equatorial particles) and several values of μ.

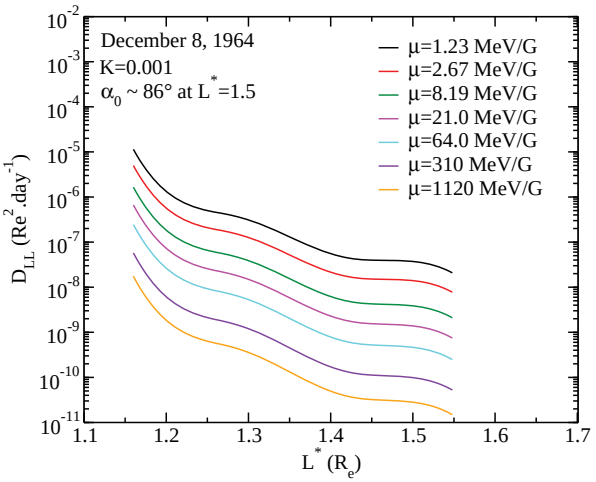

Figure 5: Evolution of the anomalous radial diffusion term $D^A_{L^*L^*}$ vs L^* for $K = 0.001$ and different values of the first adiabatic invariant μ. The indicated values for first adiabatic invariant μ (taken in ascending order) in the legend correspond respectively to energies of $E = 0.1$, 0.2, 0.5, 1.0, 2.0, 5.0 and 10 MeV at $L^* = 1.5$.

Other simulations have been made for different values of K, as presented in Figure 6. For smaller equatorial pitch angles, electrons are likely to be in the loss cone at small L^* values, for example at $L^* < 1.3$ for $\alpha_0 \sim 43°$. The above results theoretically support the empirically-derived negative slopes shown in Figure 2 as observed by Newkirk and Walt (1968) and Farley (1969).

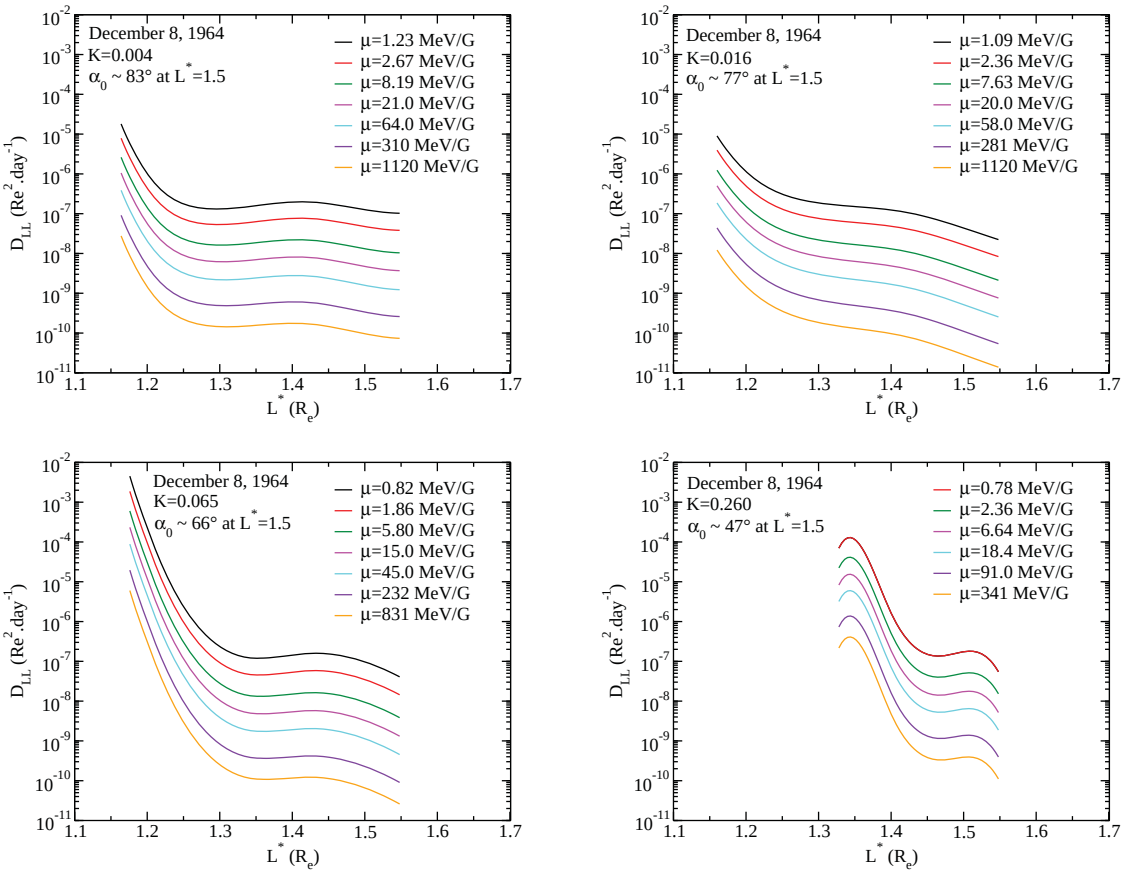

Figure 6: Evolution of the anomalous radial diffusion term $D^A_{L^*L^*}$ vs L^* for $K = 0.004$ (top-left), $K = 0.016$ (top-right), $K = 0.065$ (bottom-left) and $K = 0.260$ (bottom-right) with different values of the first adiabatic invariant μ. Again, the indicated values for first adiabatic invariant μ (taken in ascending order) correspond respectively to energies of $E = 0.1$, 0.2, 0.5, 1.0, 2.0, 5.0 and 10 MeV at $L^* = 1.5$ for $K = 0.004$, $K = 0.016$ and $K = 0.065$. For the last case $K = 0.260$, the values for μ (taken in ascending order) correspond respectively to energies of $E = 0.2$, 0.5, 1.0, 2.0, 5.0 and 10 MeV at $L^* = 1.5$.

Anomalous radial diffusion coefficients have also been obtained at another date (March 8, 2010) and confirmed the negative slopes of the radial diffusion coefficients at low L shells.

5.2. Comparison with the empirically-derived diffusion coefficients

As stated before, Farley (1969) focused on a radial diffusion coefficient $D_{L^*L^*}(\mu, K = 0, L^*)$ such that μ corresponds to $E = 1.0$ MeV at $L^* = 1.65$, which gives $\mu \sim 28$ MeV/G from the IGRF model. However the values obtained by Farley (1969) can be considered as an upper limit for the radial diffusion coefficient (Walt, 1971) and are two order of magnitude higher than the values obtained from our calculations, which makes the comparison with our anomalous radial diffusion term difficult. As for Newkirk and Walt (1968), they obtained average values of the radial diffusion coefficient for electrons above the threshold energy of 1.6 MeV rather than a $D_{L^*L^*}(\mu, K = 0, L^*)$ expressed at a fixed μ. Hence the function represented in Figure 2 (left) is $\langle D_{L^*L^*}\rangle_{E>E_0}$, with $E_0 = 1.6$ MeV, where

$$\langle D_{L^*L^*}\rangle_E = \left(\int_E D_{L^*L^*} f_E \, \mathrm{d}E\right) \Big/ \left(\int_E f_E \, \mathrm{d}E\right),$$

with f_E is the distribution function of electrons in energy. We can nevertheless relate our D_{LL} calculation with the term $\langle D_{L^*L^*}\rangle_{E>E_0}$ described by (Newkirk and Walt, 1968). As shown in Figure 5, the radial diffusion coefficient falls abruptly when μ increases for $L^* \in [1.15, 1.21]$. In this narrow interval of L^*, we can also consider that the energy does not vary much for a fixed μ (for instance $\mu = 21$ MeV/G corresponds to $E = 1.53$ MeV at $L^* = 1.21$ and $E = 1.66$ MeV at $L^* = 1.15$), and so the radial diffusion coefficient should also decrease strongly when the energy increases. Furthermore, for these high energies ($E > 2$ MeV), the distribution function f_E decreases with increasing energies, leading to the fact that $\langle D_{L^*L^*}\rangle_{E>E_0}$ should approximatively have the same behavior and the same order of magnitude as our $D_{L^*L^*}$ at $E = E_0 = 1.6$ MeV, i.e. for $\mu \sim 21$ MeV/G. The comparison between the empirically-derived diffusion coefficient from Newkirk and Walt (1968) and the diffusion coefficient taken from our computations is shown in Figure 7.

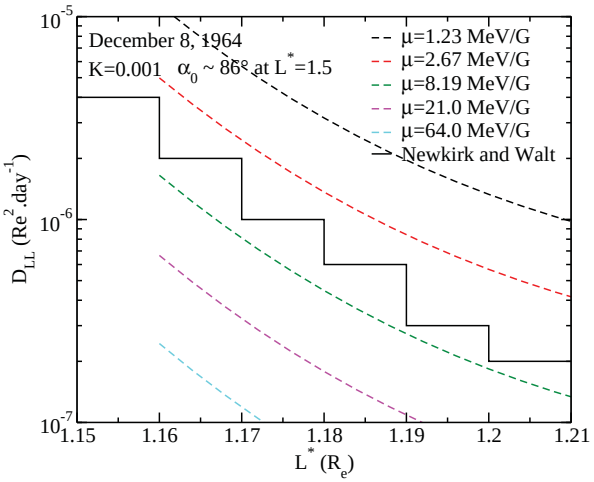

Figure 7: Evolution of the anomalous radial diffusion term $D^A_{L^*L^*}$ taken from our computations (dashed line) vs L^* for $K = 0.001$ and different values of the first adiabatic invariant μ, compared with the results obtained by Newkirk and Walt (1968) (solid line). The purple curve corresponding to $\mu = 21$ MeV/G is not the closest curve to the values of Newkirk and Walt (1968), indicating that we might have underestimated the values of the drift-shell splitting term $\delta L^*/\delta\alpha_0$.

The orders of magnitude of the radial diffusion coefficients shown in Figure 7 are consistent with the empirical results from Newkirk and Walt (1968), with $D_{L^*L^*}$ taking values between 10^{-5} and 10^{-7} R_e^2/day for $L^* \in [1.15, 1.20]$.

6. Conclusions

Throughout this work we have investigated and quantified the physical processes thought to produce additional radial diffusion at low L shell values. Roederer et al. (1973) worked on a physical interpretation of the surprising empirical radial diffusion coefficients obtained by Newkirk and Walt (1968) and Farley (1969), which exhibit a significant drop as L^* increases, up to $L^* = 1.5$. At low L^* values, a particle trapped in the Earth magnetic field experiences a pitch angle diffusion induced by atmospheric scattering. As the magnetic field is intrinsically asymmetric, a change in the pitch angle will end up in a change in drift-shell due to the drift-shell splitting effects, leading to additional and non-negligible radial diffusion. Hence we use the formalism of O'Brien (2015) to highlight an anomalous radial diffusion coefficient. The drift-shell splitting effect is represented by the variation of the radial invariant L^* with respect to the equatorial pitch angle. This term has been computed for all (L^*, K, φ) by calling the routines discussed in (Cunningham, 2016). Some improvements have yet to be done to find the optimal numerical value of $\delta\alpha_0$ to better quantify the drift-shell splitting term $\delta L^*/\delta\alpha_0$. The atmospheric scattering effect is computed from the pitch angle diffusion coefficient D_{xx} from atmospheric Coulomb scattering derived from Selesnick (2012). In this perspective, we

use the MSIS model, implemented in the LANL-GeoMag library, to find the density profile of the neutral species. Moreover, an integration of the local D_{xx} over the bounce path taken in the IGRF magnetic field has also been required. From all of these steps, we put forward a drift-averaged radial diffusion coefficient at very low L^* values, expressed in terms of μ, K and L^*. The final results we got are promising as they show the same global decreasing trend as observed by Newkirk and Walt (1968) and Farley (1969) in the late 60's. We will continue investigating this process for different atmospheric conditions and at different dates in order to confirm this unusual transport. We also expect to assess for which electron energy and pitch angle the abnormal diffusion becomes significant and whether it can become a dominant mode of transport at low L shell.

References

Brautigam, D.H., Albert, J.M., 2000. Radial diffusion analysis of outer radiation belt electrons during the october 9, 1990, magnetic storm. Journal of Geophysical Research: Space Physics 105, 291–309.

Cunningham, G.S., 2016. Radial diffusion of radiation belt particles in nondipolar magnetic fields. Journal of Geophysical Research: Space Physics 121, 5149–5171. 2015JA021981.

Fälthammar, C.G., 1965. Effects of time-dependent electric fields on geomagnetically trapped radiation. Journal of Geophysical Research 70, 2503–2516.

Farley, T.A., 1969. Radial diffusion of starfish electrons. Journal of Geophysical Research 74, 3591–3600.

Newkirk, L.L., Walt, M., 1968. Radial diffusion coefficient for electrons at low l values. Journal of Geophysical Research 73, 1013–1017.

O'Brien, T.P., 2015. The activity and radial dependence of anomalous diffusion by pitch angle scattering on split magnetic drift shells. Journal of Geophysical Research: Space Physics 120, 328–343. 2014JA020422.

Ozeke, L.G., Mann, I.R., Murphy, K.R., Jonathan Rae, I., Milling, D.K., 2014. Analytic expressions for ulf wave radiation belt radial diffusion coefficients. Journal of Geophysical Research: Space Physics 119, 1587–1605. 2013JA019204.

Roederer, J., 1970. Dynamics of geomagnetically trapped radiation. Physics and chemistry in space, Springer-Verlag.

Roederer, J., Zhang, H., 2014. Dynamics of Magnetically Trapped Particles: Foundations of the Physics of Radiation Belts and Space Plasmas. Astrophysics and Space Science Library, Springer Berlin Heidelberg.

Roederer, J.G., Hilton, H.H., Schulz, M., 1973. Drift shell splitting by internal geomagnetic multipoles. Journal of Geophysical Research 78, 133–144.

Schulz, M., Lanzerotti, L., 1974. Particle diffusion in the radiation belts. Physics and chemistry in space, Springer-Verlag.

Selesnick, R.S., 2012. Atmospheric scattering and decay of inner radiation belt electrons. Journal of Geophysical Research: Space Physics 117. A08218.

Selesnick, R.S., Albert, J.M., Starks, M.J., 2013. Influence of a ground-based vlf radio transmitter on the inner electron radiation belt. Journal of Geophysical Research: Space Physics 118, 628–635.

Walt, M., 1971. Radial diffusion of trapped particles and some of its consequences. Reviews of Geophysics 9, 11–25.

Testing EMIC wave simulated gain with Van Allen Probes' HOPE measurements

Anthony A. Saikin

Space Science Center and Department of Physics, University of New Hampshire, Durham, NH 03824, USA

Vania K. Jordanova

Los Alamos National Laboratory, Los Alamos, NM 87544, USA

Abstract:

This paper focuses on modeling EMIC wave generation with *in situ* observations from the Van Allen Probes. Plasma measurements associated with EMIC wave events observed by the Van Allen Probes' Electric and Magnetic Field Instrument Suite and Integrated Science (electron density) and the Helium, Oxygen, Proton, and Electron mass spectrometer (density, anisotropy, and parallel temperature of H^+, He^+, O^+) were used to model EMIC wave growth against the observations. Linear Theory was used to select EMIC wave events with plasma conditions favorable for EMIC wave generation. Of 680 events observed during the Van Allen Probes first complete magnetic local time precession, 168 events (98 H^+-band and 100 He^+-band) were found to satisfy Linear Theory, indicating those regions contained favorable plasma conditions for EMIC wave growth. Results reveal that ~80% of the modeled EMIC wave events could not reproduce the observed wave amplitudes, despite having favorable plasma conditions. These events lacked the free energy necessary for EMIC wave generation. Upon retroactively calculating the necessary anisotropy of hot protons, i.e., the free energy, the model reproduced wave amplitudes with a ~68% agreement.

Keywords: EMIC waves, wave generation, Van Allen Probes

1. Introduction

Electromagnetic ion cyclotron (EMIC) waves are Pc1 – Pc2 pulsating (0.1 – 5 Hz), left-hand polarized, transverse propagating waves. Through wave-particle interactions, EMIC wave events impact particle dynamics within the Earth's magnetosphere. These interactions take the form of relativistic electron pitch angle scattering in the radiation belts [*Thorne and Kennel*, 1971; *Lyons et al.*, 1972; *Meredith et al.*, 2003; *Summers et al.*, 2007; *Jordanova et al.*, 2008], energetic proton scattering losses in the ring current [*Jordanova et al.*, 2001], heavy ion heating (up to 1 keV) [*Zhang et al.*, 2010, 2011]. EMIC wave activity has also been associated with the appearances of traveling convection vortices inside the Earth's magnetosphere [*Lockwood et al.*, 1990; *Engebretson et al.*, 2013], and may influence the appearance of isolated auroral arc events [*Sakaguchi et al.*, 2008]. Given the crucial role EMIC waves play in the magnetosphere, along with their global distribution [*Anderson et al.*, 1992; *Kasahara et al.*, 1992; *Halford et al.*, 2010; *Min et al.*, 2012; *Allen et al.*, 2015; *Saikin et al.*, 2015], understanding the mechanisms behind their generation remains an important topic of study.

EMIC waves are generated in regions of magnetic field minima when hot (usually 10 – 100 keV) anisotropic ($T_\perp > T_\parallel$) ions overlap with cold (~1eV) dense plasma populations [*Kennel and Petschek*, 1966]. Here, the hot ion populations provide the "free energy" necessary for EMIC wave growth [*Cornwall*, 1965; *Rauch and Roux*, 1982]. Cold heavy ions (He^+ and O^+) contribute by lowering the instability threshold and increasing the wave growth rate [*Young et al.*, 1981; *Rauch and Roux*, 1982; *Kozyra et al.*, 1984; *Horne and Thorne*, 1993]. Since cold plasma enhances EMIC wave generation, the plasmasphere and plasmaspheric

plumes have often been suggested as favorable source region locations [*Fraser et al.*, 1989; *Horne and Thorne*, 1993; *Fraser and Nguyen*, 2001; *Morley et al.*, 2009; *Pickett et al.*, 2010; *Usanova et al.*, 2013]. Hot ring current H^+, during geomagnetic storms, could then be injected into the inner magnetosphere and overlap with these cold dense plasma populations [*Cornwall*, 1965; *Jordanova et al.*, 2001; *Fraser et al.*, 2010; *Halford et al.*, 2010, 2016; *Meredith et al.*, 2014; *Saikin et al.*, 2016]. Post generation, EMIC waves propagate away from their source regions along magnetic field lines to regions of increased magnetic field strength [*Mauk and McPherron*, 1980].

EMIC waves can be categorized by the wave band in which they are observed. Within the Earth's magnetosphere, this gyrofrequency distinction allows us to generally classify EMIC waves as H^+-, He^+-, or O^+-band EMIC waves. H^+-band EMIC waves are defined as non-broadband wave activity observed below the proton gyrofrequency, but above the helium ion gyrofrequency. Similarly, He^+-band EMIC waves are those wave pulsations observed below the helium ion gyrofrequency and above the oxygen gyrofrequency. Finally, O^+-band EMIC waves are those events observed below the oxygen gyrofrequency. The specific ion composition of the cold plasma also directly affects which wave-band EMIC wave activity is excited. For example, the presence of cold He^+ increases the growth rate for He^+-band EMIC waves, while lowering the growth rate for H^+-band EMIC waves [*Kozyra et al.*, 1984]. Furthermore, wave-band specific EMIC waves are not observed equally [*Min et al.*, 2012; *Keika et al.*, 2013; *Saikin et al.*, 2015; *Wang et al.*, 2015; *Yu et al.*, 2015].

Numerous studies have produced models incorporating the impact of the cold plasma (with specific ratios of H^+, He^+, and O^+) and hot ions on EMIC wave generation and propagation [*Rauch and Roux*, 1982; *Kozyra et al.*, 1984; *Horne and Thorne*, 1993; *Jordanova et al.*, 2001, 2007; *Hu et al.*, 2010; *Denton et al.*, 2014; *Gamayunov et al.*, 2014]. Each respective study examines a different region of the Earth's magnetosphere and varies the respective ion populations used in the simulation. However, with respect to data and simulations, portions of the Earth's inner magnetosphere remain underexplored [*Saikin et al.*, 2015]. As previously stated, given the global impact EMIC waves can have on the magnetosphere, using both data and simulations to model the plasma conditions and wave growth associated with their generation remains an ongoing region of focus.

This study focuses on investigating EMIC wave observations, and their associated plasma conditions, taken by the Van Allen Probes and applying those measurements to EMIC wave growth models. This paper is organized as follows: a description of the Van Allen Probes and their instruments (section 2.1), the description of our EMIC wave identification and selection method (section 2.2), the outline of the model and calculations used in this study (section 2.3), the results of our simulations (section 3), and finally our discussion and conclusions (sections 4 and 5, respectively).

2. Instrumentations and Model

2.1 Van Allen Probes

The Van Allen Probes mission [*Kessel et al.*, 2013; *Mauk et al.*, 2013] are two identical spacecraft that orbit around the Earth with an apogee and perigee of 5.8 and 1.1 R_e, respectively. Each probe performs a highly elliptical, low inclination (~10°) orbit with a period of ~9 h. Each probe, denoted as Probe A and Probe B, follow nearly identical orbits at different speeds, causing one probe to lap the other every ~2.5 months. The perigee-apogee lines of each probe precesses in local time at a rate of ~210°/yr.

For this study, two instruments on board both Van Allen Probes have been used to identify EMIC wave activity and measure the plasma conditions during their observations. The Electric and Magnetic Field Instrument Suite and Integrated Science (EMFISIS) [*Kletzing et al.*, 2013] contains a magnetometer instrument that provides high temporal resolution (64 vectors per second) magnetic field measurements. Each EMFISIS has two magnetic field sensors, a triaxial fluxgate magnetometer (MAG), and a triaxial AC magnetic search coil magnetometer. For this study, we have only used magnetic field measurements from MAG.

Plasma data was obtained from the Helium, Oxygen, Proton, and Electron (HOPE) mass spectrometer [*Funsten et al.*, 2013], which is part of the Radiation Belt Storm Probes- Energetic Particle Composition and Thermal Plasma (RBSP-ECT) [*Spence et al.*, 2013]. The HOPE mass spectrometer measures electron and ion flux distributions over 4π sr every spacecraft spin in the energy range of ~1 eV –

52 keV. HOPE also distinguishes between the three major ion species of H^+, He^+, and O^+. Available data from the HOPE instrument begins on 25 October 2012. This EMIC wave survey encompasses the period of 1 November 2012 – 31 August 2014. This 22-month period covers one complete Van Allen Probes MLT precession.

2.2 EMIC wave selection and Linear Theory Proxy

EMIC wave selection follows the same guidelines described in *Saikin et al.* [2015] and *Saikin et al.* [2016]. EMIC wave events were visually identified from daily plots generated from the EMFISIS data set. EMIC wave events must be observed for at least 5 minutes in Universal Time (UT). This time limit was imposed to avoid background noise being considered EMIC wave activity. Furthermore, broadband wave activity was not included in this study (for an example see Figure 1c in *Zhang et al.* [2014] of broadband and EMIC wave activity). A minimum wave power threshold of 0.01 nT^2/Hz was employed, with wave power being calculated by the procedures described in *Allen et al.* [2013] and *Zhang et al.* [2014]. Since EMFISIS provides high fidelity data, H^+-, He^+-, and O^+-band EMIC wave events have been included in this study. Electron density (n_e) was determined following the method used by *Zhelavskaya et al.* [2016].

Not all EMIC wave events observed within this 22-month precession were used in this study. Since the purpose of this study is to use in situ measurements with the model (described in section 2.3), events who had plasma conditions more favorable for EMIC wave generation during their observations were used. This event selection was determined by testing the Van Allen Probes' EMIC wave observations with a Linear Theory proxy. Linear Theory states that if the observational growth parameter, Σ_h, exceeds the theoretical instability threshold, S_h, then the plasma is favorable for EMIC wave excitation [*Gary et al.*, 1994; *Blum et al.*, 2009; *Zhang et al.*, 2014]. Events that satisfied this criterion, $\Sigma_h - S_h > 0$, were included in this study. Here, the observational growth parameter is defined as:

$$\Sigma_h = \left(\frac{T_\perp}{T_\parallel} - 1\right)\beta_{\parallel hp}^{\alpha_h} \quad \textbf{(1)}$$

$$\alpha_h = a_0 - a_1 \ln\left(\frac{n_{hp}}{n_e}\right) - a_2\left[\ln\left(\frac{n_{hp}}{n_e}\right)\right]^2 \quad \textbf{(2)}$$

The observational growth parameter depends explicitly on the hot proton anisotropy, $A_{hp} = T_\perp/T_\parallel - 1$, the parallel hot proton plasma beta, $\beta_{\parallel hp}$, and the ratio of the hot proton to electron density, n_{hp}/n_e. The constants a_0, a_1, and a_2 are derived from *Blum et al.* [2009], and equal 0.409, 0.0145, and 0.00028, respectively.

The theoretical instability threshold is defined as:

$$S_h = \sigma_0 + \sigma_1 \ln\left(\frac{n_{hp}}{n_e}\right) + \sigma_2\left[\ln\left(\frac{n_{hp}}{n_e}\right)\right]^2 \quad \textbf{(3)}$$

Here, $\sigma_0 = 0.429$, $\sigma_1 = 0.124$, and $\sigma_2 = 0.0018$. These values are also derived from *Blum et al.* [2009].

2.3 EMIC wave growth and gain model

To calculate EMIC wave convective growth rates, this study follows the procedures outlined *in Koyzra et al.* [1984] and *Jordanova et al.* [2001]. Given that EMIC wave amplification depends on the time spent within the source region, convective growth rates are more suitable to understand EMIC wave growth. The convective growth rate, S (1/cm), is calculated by taking the ratio of the temporal growth rate, μ (1/s), and the group velocity, V_g (cm/s):

$$S = \frac{\mu}{V_g} \quad \textbf{(4)}$$

The temporal growth rate is determined by:

$$\mu = \frac{\omega_i}{\Omega_p} = \left\{\sum_i \frac{\Omega_p \eta_{lw}\sqrt{\pi}}{M_i^2\,\alpha_{ll} k}\left[[(A_i+1)(1-M_iX)-1] * exp\left[\frac{-\Omega_p^2}{M_i^2}\frac{(M_iX-1)^2}{\alpha_{ll}^2 k^2}\right]\right]\right\} * \left\{\frac{X(\delta+1)(2-X)}{(X-1)^2} + \sum_j (\eta_{jw}+\eta_{jc}) * \frac{M_jX(2-M_jX)}{(M_jX-1)^2}\right\}^{-1} \quad \textbf{(5)}$$

$$M_j = \frac{m_j}{z_j m_p} \quad \textbf{(6)}$$

$$\eta_{jw(c)} = M_j \frac{\omega_{pwj(c)}^2}{\omega_{ppw}^2} \quad \textbf{(7)}$$

,

The temporal growth depends on the plasma frequency for that respective ion and warm (cold) population, $\omega_{pjw(c)}$, the real part of the frequency, ω_r, the mass of the ion species, m_j, the proton gyrofrequency, Ω_p.

The group velocity is determined by:

$$V_g = \frac{\partial\omega}{\partial k} = \left\{\frac{2\Omega_p c}{\omega_{ppw}}\left[\frac{1+\delta}{1-X} + \sum_j \eta_{jw} + \eta_{jc}\frac{M_j}{1+M_jX}\right]^{\frac{1}{2}}\right\} * \left\{\frac{(1+\delta)(2-X)}{(1-X)^2} + \sum_j \frac{(\eta_{jw}+\eta_{jc})M_j(2-M_jX)}{(1-M_jX)^2}\right\}^{-1} \quad \textbf{(8)}$$

Given the inputs, the simulation will calculate growth rates for every frequency, and all three wave-band specific EMIC waves (i.e., H^+-, He^+-, and O^+-band EMIC waves). Effects of the orbit (i.e., MLT, *L* shell) and the location with respect to the plasmasphere are incorporated later in the simulation code as possible EMIC wave amplifiers. The plasmasphere location was determined based off measurements of the electron density taken by the EMFISIS instrument [*Zhelavskaya et al.*, 2016]. Events observed within the plasmasphere were given a plasmasphere enhancement by multiplying the convective growth rate by a factor of 2. The simulation then chooses the highest convective growth rate and displays the respective group velocity, temporal growth rate, and the frequency (normalized to the proton gyrofrequency) where the highest convective growth rate was determined. Measurements from the Van Allen Probes' HOPE instrument inputted into the simulation include: the density, anisotropy, and the parallel temperature of the hot protons, hot helium, and hot oxygen ions. For all parameters, the maximum value measured during the event duration was used. HOPE does not take cold plasma measurements; therefore, the specific ratios of the cold plasma populations was set constant for every model calculation as explained below.

Once the max convective growth rate was determined, the gain [dB] for that convective growth rate was determined. The gain was then used to calculate the simulated max wave amplitude (nT), B_w:

$$B_w = 10 * 10^{\frac{G-G_1}{20}} \quad \textbf{(9)}$$

For best agreement with the data, $G_1 = 40$ [*Jordanova et al.*, 2001].

3. Simulation results

During the period used for this survey, over 600 EMIC wave events were identified and catalogued among the H^+, He^+, and O^+ wave-bands. Each event was tested with Linear Theory. For a sample calculation, please refer to Figure 2 of *Zhang et al.* [2014]. However, only 198 (98 H^+-band, 100 He^+-band, 0 O^+-band) of the EMIC wave events were found to satisfy Linear Theory, indicating that the plasma conditions are

favorable for EMIC wave generation. These events, and their corresponding plasma conditions observed during their event duration, were inputted into the numerical model where their convective growth rates, gain, and wave amplitudes were calculated.

Figure 1 shows the results of the simulation gain (x-axis) versus the observed wave amplitude (y-axis) taken by the Van Allen Probes. The red line marks the relation between B_w and gain. The results for H^+- and He^+-band waves were calculated separately with different cold plasma ratios. Different cold plasma ratios were used since the presence of heavier cold ions damps wave growth of higher wave-band EMIC waves (e.g., cold O^+ would suppress wave growth for the He^+-band EMIC waves) [*Young et al.*, 1981; *Rauch and Roux*, 1982; *Kozyra et al.*, 1984; *Horne and Thorne*, 1993]. H^+-band EMIC simulated waves (Figure 1a) were calculated with a cold plasma ratio of 1.00 H^+, 0 He^+, and 0 O^+. He^+-band EMIC simulated waves (Figure 1b) used a cold plasma ratio of 0.77 H^+, 0.20 He^+, and 0.03 O^+ [*Jordanova et al.*, 2001].

The results are consistent for both H^+- and He^+-band EMIC waves. In both wave-band calculations, the simulated gain based off the observed plasma conditions during the event duration cannot reproduce the observed wave amplitudes. For 82% (80%) of the H^+-band (He^+-band) EMIC waves, the simulation produces gain measurements that are too weak to reproduce observations. This indicates a lack of "free energy" necessary for EMIC wave generation.

Previous work has commented that the Van Allen Probes' HOPE instrument may underestimate the anisotropy [*Fu et al.*, 2014]. Since ring current protons generally supply the free energy used for EMIC wave generation, the simulation was altered to retroactively calculate the needed anisotropy for the respective observations, with a maximum A_{hp} of 1.5. Figure 2 shows histograms for the H^+-band (Figure 2a) and He^+-band (Figure 2b) required changes in proton anisotropy to match the observation. Here, ΔA_{hp} is defined as the retroactive A_{hp} – the observed A_{hp}. The results in Figure 2 show that for 76% and 81% of the H^+- and He^+-band EMIC wave events, respectively, the measured A_{hp} is too low to match observations.

For each event, the convective wave growth rates and gain were recalculated using the retroactive A_{hp}. Figure 3 displays this recalculated gain against the observed wave amplitude. There is an overall agreement of 75% between the observed wave amplitude and the revised gain calculation for both the H^+- and He^+-band EMIC waves. Most events that are not in agreement with the observed wave amplitude still register gain values that are too low to match data. Other variables inputted into the model (e.g., densities, parallel temperatures, and anisotropies of the hot He^+, and hot O^+, etc.) were also retroactively calculated to determine the respective value to match the observations. However, only A_{hp} produced the highest rate of agreement.

4. Summary

In this study, the generation of EMIC wave events were modeled with data inputs taken by the Van Allen Probes' HOPE instrument. EMIC wave events were selected based on criteria specified by *Saikin et al.* [2015]. Events were examined with Linear Theory to determine if the plasma conditions associated with the EMIC wave observation were favorable for EMIC wave growth. These favorable plasma conditions were used to simulate EMIC convective wave growth and gain to match the observed wave amplitudes.

Given the inputs taken by the Van Allen Probes' EMFISIS (electron density) and HOPE (the density, anisotropy, and parallel temperature of H^+, He^+, and O^+) instruments, the model was unable to reproduce observations for most the events. 82% (~80%) of the H^+-band (He^+-band) events yielded convective growth rates too low to match the observed wave amplitude values. The measurements observed during these events lacked the free energy necessary to match the observed wave amplitude. Following *Fu et al.* [2014], A_{hp} was retroactively calculated to determine the necessary values to match the data. This method of altering A_{hp} yielded a ~68% agreement between the simulated wave growth and observations. This implies that upon excitation, the initial anisotropy that caused the EMIC wave instability has decreased to the value the Van Allen Probes measure when the event is observed. Future work on modeling EMIC wave generation should consider adding the contribution of high-energy ion populations measured by the Magnetic Electron Ion Spectrometer instrument onboard the Van Allen Probes. These high-energy ion populations may increase the amount of free energy, A_{hp}, for EMIC wave generation and account for the discrepancies between the HOPE measured A_{hp} during the observation and A_{hp} required to match the observed wave amplitudes.

References

Allen, R. C., J.-C. Zhang, L. M. Kistler, H. E. Spence, R. L. Lin, M. W. Dunlop, and M. André (2013), Multiple bidirectional EMIC waves observed by Cluster at middle magnetic latitudes in the dayside magnetosphere, *J. Geophys. Res. Sp. Phys.*, *118*, 6266–6278, doi:10.1002/jgra.50600.

Allen, R. C., J.-C. Zhang, L. M. Kistler, H. E. Spence, R.-L. Lin, B. Klecker, M. W. Dunlop, M. André, and V. K. Jordanova (2015), A statistical study of EMIC waves observed by Cluster: 1. Wave properties, *J. Geophys. Res. Sp. Phys.*, *120*, 5574–5592, doi:10.1002/2015JA021333.

Anderson, B. J., R. E. Erlandson, and L. J. Zanetti (1992), A statistical study of Pc 1-2 magnetic pulsations in the equatorial magnetosphere I. Equatorial occurrence distributions., *J. Geophys. Res.*, *97*, 3075–3088, doi:10.1029/91JA02706.

Blum, L. W., E. A. MacDonald, S. P. Gary, M. F. Thomsen, and H. E. Spence (2009), Ion observations from geosynchronous orbit as a proxy for ion cyclotron wave growth during storm times, *J. Geophys. Res.*, *114*, A10214–A10223, doi:10.1029/2009JA014396.

Cornwall, J. M. (1965), Cyclotron instabilities and electromagnetic emission in the ultra low frequency and very low frequency ranges, *J. Geophys. Res.*, *70*(1), 61–69, doi:10.1029/JZ070i001p00061.

Denton, R. E., V. K. Jordanova, and B. J. Fraser (2014), Effect of spatial density variation and O + concentration on the growth and evolution of electromagnetic ion cyclotron waves, *J. Geophys. Res.*, *119*, 8372–8395, doi:10.1002/2014JA020384.Received.

Engebretson, M. J. et al. (2013), Multi-instrument observations from Svalbard of a traveling convection vortex, electromagnetic ion cyclotron wave burst, and proton precipitation associated with a bow shock instability, *J. Geophys. Res. Sp. Phys.*, *118*, 2975–2997, doi:10.1002/jgra.50291.

Fraser, B. J., W. J. Kemp, and D. J. Webster (1989), Ground-satellite study of a Pc 1 ion cyclotron wave event, *J. Geophys. Res.*, *94*, 11855–11863.

Fraser, B. J., and T. S. Nguyen (2001), Is the plasmapause a preferred source region of electromagnetic ion cyclotron waves in the magnetosphere?, *J. Atmos. Solar-Terrestrial Phys.*, *63*, 1225–1247, doi:10.1016/S1364-6826(00)00225-X.

Fraser, B. J., R. S. Grew, S. K. Morley, J. C. Green, H. J. Singer, T. M. Loto'aniu, and M. F. Thomsen (2010), Storm time observations of electromagnetic ion cyclotron waves at geosynchronous orbit: GOES results, *J. Geophys. Res.*, *115*, A05208–A05223, doi:10.1029/2009JA014516.

Fu, X. et al. (2014), Whistler anisotropy instabilities as the source of banded chorus: Van Allen Probes observations and particle-in-cell simulations, *J. Geophys. Res. Sp. Phys.*, *119*(10), 8282–8298, doi:10.1002/2014JA020364.

Funsten, H. O. et al. (2013), Helium, oxygen, proton, and electron (HOPE) mass spectrometer for the Radiation Belt Storm Probes mission, *Sp. Sci Rev*, 423–484, doi:10.1007/978-1-4899-7433-4-13.

Gamayunov, K. V, M. J. Engebretson, M. Zhang, and H. K. Rassoul (2014), Model of electromagnetic ion cyclotron waves in the inner magnetosphere, *J. Geophys. Res.*, *119*, 7541–7565, doi:10.1002/2014JA020032.Received.

Gary, S. P., M. B. Moldwin, M. F. Thomsen, D. Winske, and D. J. McComas (1994), Hot proton anisotropies and cool proton temperatures in the outer magnetosphere, *J. Geophys. Res. Sp. Phys.*, *99*, 23603–23615, doi:10.1029/94JA02069.

Halford, A. J., B. J. Fraser, and S. K. Morley (2010), EMIC wave activity during geomagnetic storm and nonstorm periods: CRRES results, *J. Geophys. Res. Sp. Phys.*, *115*, A12248–A12263, doi:10.1029/2010JA015716.

Halford, A. J., B. J. Fraser, S. K. Morley, S. R. Elkington, and A. A. Chan (2016), Dependence of EMIC wave parameters during quiet, geomagnetic storm, and geomagnetic storm phase times, *J. Geophys. Res. A Sp. Phys.*, (121), 6277–6291, doi:10.1002/2016JA022694.

Horne, R. B., and R. M. Thorne (1993), On the preferred source location for the convective amplification of ion cyclotron waves, *J. Geophys. Res.*, *98*, 9233–9247, doi:10.1029/92JA02972.

Hu, Y., R. E. Denton, and J. R. Johnson (2010), Two-dimensional hybrid code simulation of electromagnetic ion cyclotron waves of multi-ion plasmas in a dipole magnetic field, *J. Geophys. Res. Sp. Phys.*, *115*, A09218–A09231, doi:10.1029/2009JA015158.

Jordanova, V. K., C. J. Farrugia, R. M. Thorne, G. V. Khazanov, G. D. Reeves, and M. F. Thomsen (2001), Modeling ring current proton precipitation by electromagnetic ion cyclotron waves during the May 14–16, 1997, storm, *J. Geophys. Res.*, *106*, 7–22, doi:10.1029/2000JA002008.

Jordanova, V. K., M. Spasojevic, and M. F. Thomsen (2007), Modeling the electromagnetic ion cyclotron wave-induced formation of detached subauroral proton arcs, *J. Geophys. Res. Sp. Phys.*, *112*, A08209–A08222, doi:10.1029/2006JA012215.

Jordanova, V. K., J. Albert, and Y. Miyoshi (2008), Relativistic electron precipitation by EMIC waves from self-consistent global simulations, *J. Geophys. Res. Sp. Phys.*, *113*, A00A10-A00A21, doi:10.1029/2008JA013239.

Kasahara, Y., A. Sawada, M. Yamamoto, I. Kimura, S. Kokubun, and K. Hayashi (1992), Ion cyclotron emissions observed by the satellite

Akebono in the vicinity of the magnetic equator, *Radio Sci.*, *27*(2), 347–362.

Keika, K., K. Takahashi, A. Y. Ukhorskiy, and Y. Miyoshi (2013), Global characteristics of electromagnetic ion cyclotron waves: Occurrence rate and its storm dependence, *J. Geophys. Res. Sp. Phys.*, *118*, 4135–4150, doi:10.1002/jgra.50385.

Kennel, C. F., and H. E. Petschek (1966), Limits on stably trapped particle fluxes, *J. Geophys. Res.*, *71*, 1–28, doi:10.1177/1069072705283987.

Kessel, R. L., N. J. Fox, and M. Weiss (2013), The Radiation Belt Storm Probes (RBSP) and Space Weather, *Space Sci. Rev.*, *179*, 531–543, doi:10.1007/s11214-012-9953-6.

Kletzing, C. A. et al. (2013), The Electric and Magnetic Field Instrument Suite and Integrated Science (EMFISIS) on RBSP, *Space Sci. Rev.*, *179*, 127–181, doi:10.1007/s11214-013-9993-6.

Kozyra, J. U., T. E. Cravens, A. F. Nagy, and E. G. Fontheim (1984), Effects of energetic heavy ions on electromagnetic ion cyclotron wave generation in the plasmapause region, *J. Geophys. Res.*, *89*, 2217–2233.

Lockwood, M., S. W. H. Cowley, P. E. Sandholt, and R. P. Lepping (1990), The ionospheric signatures of flux transfer events and solar wind dynamic pressure changes, *J. Geophys. Res.*, *95*(90), 17113–17135, doi:10.1029/JA095iA10p17113;

Lyons, L. R., R. M. Thorne, and C. F. Kennel (1972), Pitch-Angle diffusion of radiation belt electrons within the plasmasphere, *J. Atmos. Solar-Terrestrial Phys.*, *77*(19), 3455–3474, doi:10.1029/JA077i028p05608.

Mauk, B. H., and R. L. McPherron (1980), An experimental test of the electromagnetic ion cyclotron instability within the earth's magnetosphere, *Phys. Fluids*, *23*, 2111–2127, doi:10.1063/1.862873.

Mauk, B. H., N. J. Fox, S. G. Kanekal, R. L. Kessel, D. G. Sibeck, and A. Ukhorskiy (2013), Science objectives and rationale for the radiation belt storm probes mission, *Space Sci. Rev.*, *179*, 3–27, doi:10.1007/s11214-012-9908-y.

Meredith, N. P., R. M. Thorne, R. B. Horne, D. Summers, B. J. Fraser, and R. R. Anderson (2003), Statistical analysis of relativistic electron energies for cyclotron resonance with EMIC waves observed on CRRES, *J. Geophys. Res. Sp. Phys.*, *108*, A6–A20, doi:10.1029/2002JA009700.

Meredith, N. P., R. B. Horne, T. Kersten, B. J. Fraser, and R. S. Grew (2014), Global morphology and spectral properties of EMIC waves derived from CRRES observations, *J. Geophys. Res.*, *119*, 5328–5342, doi:10.1002/2014JA020064.

Min, K., J. Lee, K. Keika, and W. Li (2012), Global distribution of EMIC waves derived from THEMIS observations, *J. Geophys. Res.*, *117*(January), 1–13, doi:10.1029/2012JA017515.

Morley, S. K., S. T. Ables, M. D. Sciffer, and B. J. Fraser (2009), Multipoint observations of Pc1-2 waves in the afternoon sector, *J. Geophys. Res.*, *114*, 1–14, doi:10.1029/2009JA014162.

Pickett, J. S. et al. (2010), Cluster observations of EMIC triggered emissions in association with Pc1 waves near Earth's plasmapause, *Geophys. Res. Lett.*, *37*, 1–5, doi:10.1029/2010GL042648.

Rauch, J. L., and A. Roux (1982), Ray tracing of ULF waves in a multicomponent magnetospheric plasma: Consequences for the generation mechanism of ion cyclotron waves, *J. Geophys. Res.*, *87*(10), 8191–8198, doi:10.1029/JA087iA10p08191.

Saikin, A. A., J.-C. Zhang, R. C. Allen, C. W. Smith, L. M. Kistler, H. E. Spence, R. B. Torbert, C. A. Kletzing, and V. K. Jordanova (2015), The occurrence and wave properties of H+-, He+-, and O+-band EMIC waves observed by the Van Allen Probes, *J. Geophys. Res. Sp. Phys.*, *120*, 1–16, doi:10.1002/2015JA021358.

Saikin, A. A., J.-C. Zhang, C. W. Smith, H. E. Spence, R. B. Torbert, and C. A. Kletzing (2016), The dependence on geomagnetic conditions and solar wind dynamic pressure of the spatial distributions of EMIC waves observed by the Van Allen Probes, *J. Geophys. Res. Sp. Phys.*, *121*, 4362–4377, doi:10.1002/2016JA022606.

Sakaguchi, K., K. Shiokawa, Y. Miyoshi, Y. Otsuka, T. Ogawa, K. Asamura, and M. Connors (2008), Simultaneous appearance of isolated auroral arcs and Pc 1 geomagnetic pulsations at subauroral latitudes, *J. Geophys. Res.*, *113*, 1–12, doi:10.1029/2007JA012888.

Spence, H. E. et al. (2013), Science goals and overview of the Radiation Belt Storm Probes (RBSP) Energetic Particle, Composition, and Thermal Plasma (ECT) suite on NASA's Van Allen Probes mission, *Sp. Sci Rev*, 311–336, doi:10.1007/978-1-4899-7433-4-10.

Summers, D., B. Ni, and N. P. Meredith (2007), Timescales for radiation belt electron acceleration and loss due to resonant wave-particle interactions: 2. Evaluation for VLF chorus, ELF hiss, and electromagnetic ion cyclotron waves, *J. Geophys. Res.*, *112*, 1–21, doi:10.1029/2006JA011993.

Thorne, R. M., and C. F. Kennel (1971), Relativistic electron precipitation during magnetic storm main phase, *J. Geophys. Res.*, *76*(19), 4446–4453.

Usanova, M. E., F. Darrouzet, I. R. Mann, and J. Bortnik (2013), Statistical analysis of EMIC waves in plasmaspheric plumes from Cluster observations, *J. Geophys. Res.*, *118*, 4946–4951, doi:10.1002/jgra.50464.

Wang, D., Z. Yuan, X. Yu, X. Deng, M. Zhou, S. Huang, H. Li, Z. Wang, C. A. Kletzing, and J. R. Wygant (2015), Statistical characteristics of EMIC waves: Van Allen Probe observations, *J. Geophys. Res. Sp. Phys.*, *120*(6), 6199–6206, doi:10.1002/2015JA021354.Received.

Young, D. T., S. Perraut, A. Roux, C. de Villedary, R. Gendrin, A. Korth, G. Kremser, and D. Jones (1981), Wave-Particle Interactions Near Observed on GEOS 1 and 2 of Ion Cyclotron Waves in He + -Rich Plasma Max-Planck-Institut far Katlenburg-Lindau 3 , made with the ESA / GEOS 1 and 2 spacecraft which give an purpose, *J. Geophys. Res.*, *86*, 6755–6772, doi:10.1029/JA086iA08p06755.

Yu, X., Z. Yuan, D. Wang, H. Li, S. Huang, Z. Wang, Q. Zheng, M. Zhou, C. a. Kletzing, and J. R. Wygant (2015), In situ observations of EMIC waves in O + band by the Van Allen Probe A, *Geophys. Res. Lett.*, doi:10.1002/2015GL063250.

Zhang, J.-C., L. M. Kistler, C. G. Mouikis, M. W. Dunlop, B. Klecker, and J.-A. Sauvaud (2010), A case study of EMIC wave-associated He+ energization in the outer magnetosphere: Cluster and Double Star 1 observations, *J. Geophys. Res.*, *115*, 1–17, doi:10.1029/2009JA014784.

Zhang, J.-C., L. M. Kistler, C. G. Mouikis, B. Klecker, J. A. Sauvaud, and M. W. Dunlop (2011), A statistical study of EMIC wave-associated He+ energization in the outer magnetosphere: Cluster/CODIF observations, *J. Geophys. Res.*, *116*, 1–14, doi:10.1029/2011JA016690.

Zhang, J.-C. et al. (2014), Excitation of EMIC waves detected by the Van Allen Probes on 28 April 2013, *Geophys. Res. Lett.*, *41*, 4101–4108, doi:10.1002/2014GL060621.

Zhelavskaya, I. S., M. Spasojevic, Y. Y. Shprits, and W. S. Kurth (2016), Automated determination of electron density from electric field measurements on the Van Allen Probes spacecraft, *J. Geophys. Res. A Sp. Phys.*, *121*(5), 4611–4625, doi:10.1002/2015JA022132.

Figures:

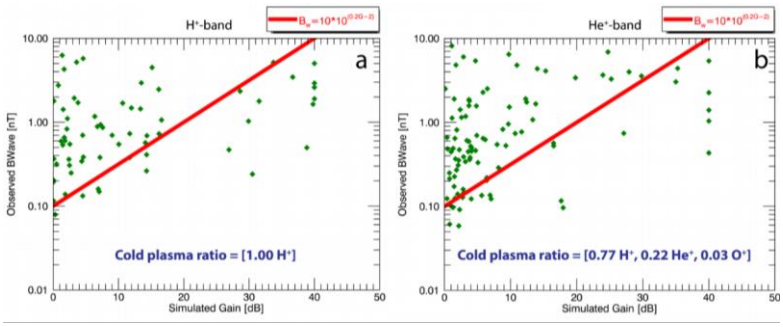

Figure 1: The simulated gain (x-axis) and the observed wave amplitude (y-axis) for the H^+-band (Figure 1a) and He^+-band (Figure 1b) EMIC wave events. The red line denotes the wave amplitude equation as a function of the gain. The assumed cold plasma ratios used for that respective band are listed in blue.

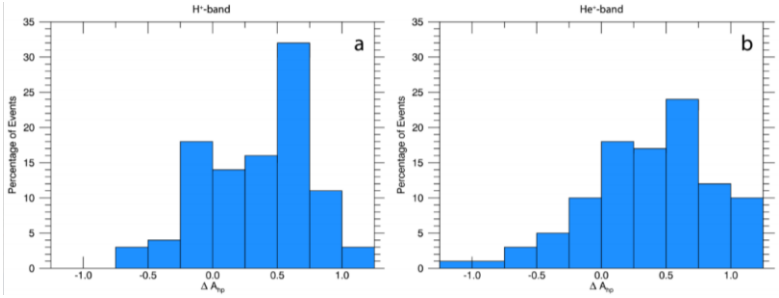

Figure 2: Histograms marking the ΔA_{hp}, the retroactively determined A_{hp} – the observed A_{hp}, needed for the model to reproduce the observed EMIC wave amplitude. The results for the H^+-band (He^+-band) are featured in Figure 2a (Figure 2b).

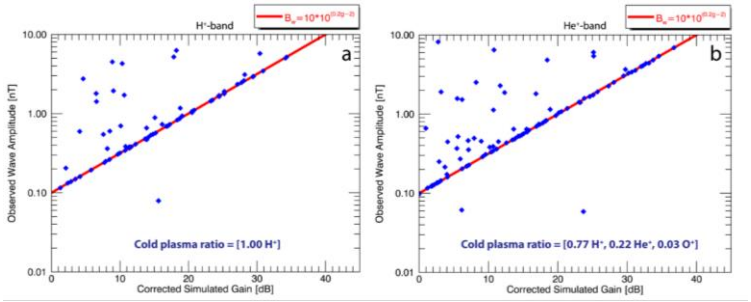

Figure 3: Same format as Figure 1. Displays the newly calculated simulated gain after altering A_{hp}.

Using ACE-Earth magnetic connection events to measure wandering length scale of interplanetary magnetic field in the solar wind

Yuguang Tong

Department of Physics and Space Sciences Laboratory, University of California at Berkeley, Berkeley, CA 94720, USA

Joseph E. Borovsky

Space Science Institute, Boulder, CO 80301, USA and CSSE, University of Michigan, Ann Arbor, MI 48109, USA

John T. Steinberg

Los Alamos National Laboratory, Los Alamos, NM 87545, USA

Abstract

It has long been challenging to use a single spacecraft to measure lengths along the mean magnetic field directions. In this letter, we show that occasional magnetic connection between a spacecraft and Earth's bow shock allow an estimation of the length scales. We report novel estimations of the length scales associated with the wandering heliospheric magnetic field at 1 AU, using a large set of ACE-Earth magnetic-connection events. We estimate that the local radius of curvature is 0.005 – 0.02 AU, and that the global length scale along the Parker spiral is 0.07 – 0.27 AU. The global length scale estimated here roughly agrees with estimations of field-aligned mean-free-path for cosmic ray scattering, braiding lengths associated with granule/supergranule motion on photosphere/ corona, and lengths associated with the wandering of the open flux at the sun enabled by reconnection in the low corona. The estimated length scale gives information about the parallel wavelength of solar wind turbulence and affects scatter-free transport of energetic charged particles in the solar wind.

Keywords: interplanetary magnetic field, IMF, parallel wavelength

1. Introduction

The wandering of the solar wind magnetic-field lines along the Parker-spiral direction is a factor for the scatter-free transport of energetic charged particles in the solar wind (Mazur et al., 2000; Chollet and Giacalone, 2011; Trenchi et al., 2013) as well as for cosmic-ray diffusive transport (Kóta and Jokipii, 2000; Webb et al., 2006; Ruffolo et al., 2008). The wandering is also a factor in the lengthening of magnetic field lines (Reames and Stone, 1986; Kahler and Ragot, 2006; Ragot, 2006). Field-line random-walk theoretical calculations for the solar wind have been performed to study particle transport (Jokipii and Parker, 1969; Giacalone et al., 2000; Pommois et al., 2001), field-line transport (Pommois et al., 2002; Weinhorst and Shalchi, 2010a; Ragot, 2011) , field-line lengths (Ragot, 2006), and structure evolution (Zimbardo et al., 2004; Kaghashvili et al., 2006). The wandering length scale compared with perpendicular length scales may provide information about the nature of anisotropy in turbulence that may be useful for testing and comparing various turbulence models (e.g. the Maltese cross (Matthaeus et al., 1990; Ruffolo et al., 2008; Weinhorst and Shalchi, 2010b), Goldreich-Sridhar (Goldreich and Sridhar, 1995, 1997; Lithwick et al., 2007), or Boldyrev (Boldyrev, 2005, 2006; Perez and Boldyrev, 2010)). Further it might provide information about intermittency in the turbulence (Kaghashvili et al., 2006; Zimbardo et al., 2008; Ragot, 2010).

Email addresses: ygtong@berkeley.edu (Yuguang Tong), jborovsky@spacescience.org (Joseph E. Borovsky), jsteinberg@lanl.gov (John T. Steinberg)

At times observation of backstreaming suprathermal electrons or energetic ions can indicate that a spacecraft is magnetically connected to Earth's bow shock (Feldman et al., 1982; Stansberry et al., 1988; Haggerty et al., 2000); such connections provide opportunities to study the behavior of magnetic field lines in the solar wind. ISEE3 observations first established that the backstreaming electrons (Scholer et al., 1980; Feldman et al., 1982) and ions (Anderson, 1981; Mitchell et al., 1983) can be observed as far as 1.5×10^6km upstream Earth at the L1 point. Since anti-sunward electron beams, also known as strahl electrons are almost always present, the backstreaming electrons from Earth's bow shock give rise to counterstreaming electron beams.

For the ACE spacecraft near the L1 Lagrangian point (see Figure 1) this connection can be seen in the suprathermal electron measurements. Figure 2 shows an example of counterstreaming in electron pitch angle distributions (PADs) measured by ACE SWEPAM instrument (McComas et al., 1998). In this example PAD, Strahl electrons are continuously present at 180° pitch angle, i.e., are anti-parallel to local magnetic field, while backstreaming electrons appear in sporadic bursts at 0° pitch angle which is opposite to the direction of Strahl electrons.

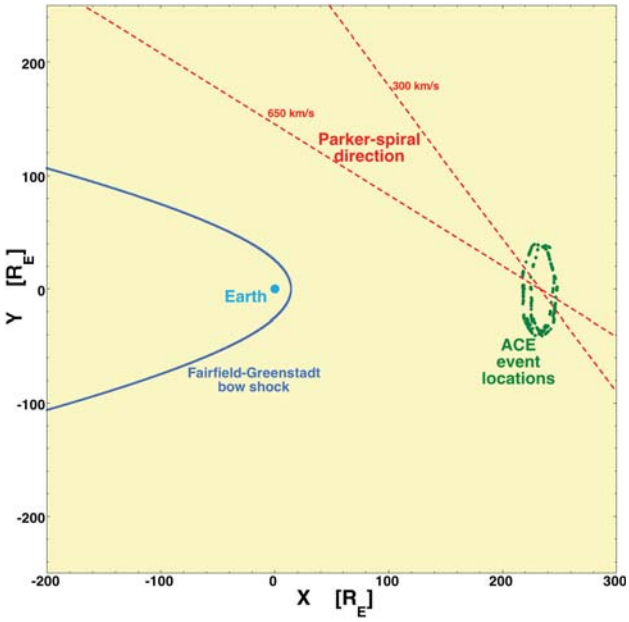

Figure 1: In the GSE X-Y plane, the green points indicate the locations of ACE around L1 at the times when magnetic connection to the bow shock occurred. The approximate shape of the bow shock is indicated in blue using the Fairfield-Greenstadt model [Fairfield, 1971; Greenstadt et al., 1990].

The occurrence of counterstreaming electrons does not exclusively imply magnetic connections to Earth's bow shock. It is well known that counterstreaming often appears upstream and downstream of interplanetary shocks, in coronal mass ejections (CMEs) (Gosling et al., 1987), and downstream of corotating interaction regions (CIRs) (Gosling et al., 1993; Steinberg et al., 2005). In addition counterstreaming can appear due to the depletion of halo particles around 90° degree pitch angle (Gosling et al., 2001, 2002; Skoug et al., 2006). The authors also observe that counterstreaming electrons are commonly present near the sector reversal regions where interplanetary magnetic field reverses its polarity.

In this study we identifed counterstreaming electrons not associated with any of the plasma conditions listed above, and we attribute that counterstreaming to terrestrial origin. A large set of ACE-Earth magnetic connection events is collected and used to uniquely estimate (1) the local radius of curvature of solar-wind magnetic-field lines and (2) the more-global wandering length scale (i.e. braiding length scale) along the Parker spiral.

2. Event selection and description

We inspected counterstreaming electrons observed by ACE in 16 months, namely, 1998 May-Nov, 2006 Oct-Dec and 2007 Jan-June. To remove counterstreaming associated with other sources, we excluded intervals when ACE observed interplanetary CMEs (Jian et al., 2006; Richardson and Cane, 2010), CIRs (Jian et al., 2011) and sector reversal regions, and 12 hours before entering and after leaving the above plasma regions. We also excluded 24 hours before and after the interplanetary shocks in the CFA Interplanetary Shock Database (Kasper). To pick out counterstreaming associated with backstreaming electrons from Earth's bow shock, we applied the following selection criteria:

1. Strahl electrons are present continuously 12 hours before and after events.
2. Enhancement of electron flux at 0° or 180° by backscattering electrons are clearly identifiable visually on ACE 272eV electron pitch angle distribution plots.
3. Similar enhancements are seen in ACE electron pitch angle distributions at energies between 100 to 500 eV.

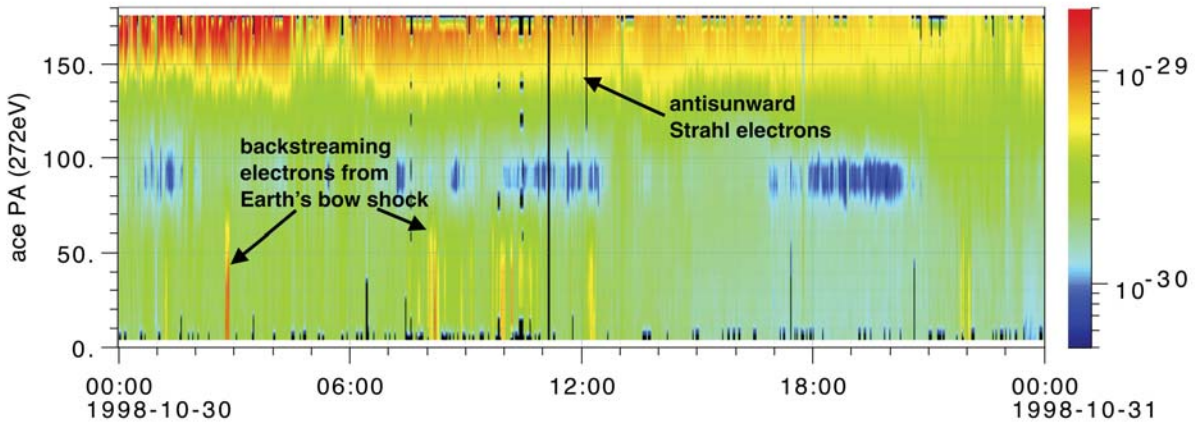

Figure 2: Example of an ACE electron pitch angle distribution plot. The color bar is in unit s^3cm^{-6}

We obtained 1135 events which covers 15274 min or 0.03% of all solar wind intervals we inspected. The majority of events are shorter than 10 min, which is consistent with the common perception that spacecraft-Earth connections are often short and bursty. But a small fraction of events are as long as one or two hours. We divided events into 14335 intervals of 64s, which is the temporal resolution of electron PAD. About half of the intervals come from events longer 30 min.

It is well known that when spacecraft-Earth connection events happen, ψ, the angle between instantaneous $\vec{B}$ and the spacecraft-Earth line is often small (Feldman et al., 1982; Stansberry et al., 1988). Figure 3 shows the relative frequency of ψ for both ambient solar wind (red) and ACE-Earth connection events (blue). We used all ACE observations from 1998, 2006 and 2007 to obtain the statistics for ambient solar wind, and we averaged magnetic field over 64s to reduce fluctuations. In ambient solar wind, ψ has small probability for small angles and large probability for large oblique angles. However, 70% of samples in connection events have $\psi < 30°$. The statistics of the ψ of our events are qualitatively consistent with the earlier study of another spacecraft at L1, namely, ISEE3 (Stansberry et al., 1988). It is worthwhile pointing out that in ambient solar wind, ψ peaks at about 60°, which can be explained by a combined effect of turbulently random fluctuations of $\vec{B}$ and a tendency to approach Parker spiral directions (Stansberry et al., 1988).

3. Estimation of local radius of curvature

To estimate the local curvature of the interplanetary magnetic field IMF in connection events, we approximated the magnetic field line shapes as circular arcs. Admittedly there is no a priori reason that field lines should take circular shapes. In fact, wandering spaghetti-shaped field lines are probably a better model for the geometric complexity of IMF. But without further assumptions, the information a magnetic connection event offers is the distance between two points (ACE and Earth) on threaded by the same field line, and the directions of $\vec{B}$ at one of those points (ACE). A circular arc is the simplest geometry that we can uniquely parametrize from measurement. In this and the next section, we also simplify the source region of backstreaming terrestrial bow shock electrons to a point target, which coincide with Earth. This simplification is discussed in detail in Section 5.1.

With the above assumptions, we fit circles to all samples in connection events to obtain radii. Figure 4 shows the frequency of histogram of the fitted radius. The most probable, medium, and mean values are 120Re (0.005AU), 370Re (0.016AU) and 480Re (0.02AU) respectively.

4. Wandering length scale along the Parker spiral

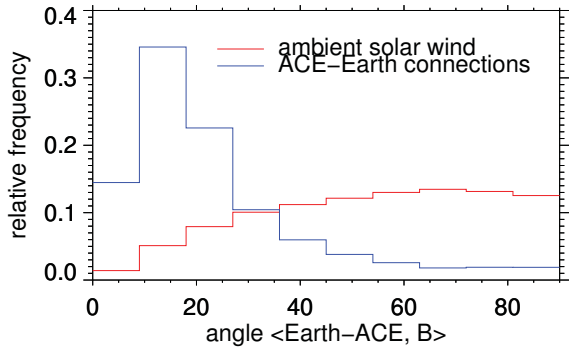

Figure 3: Relative frequency of the angle ψ between instantaneous magnetic field direction (64s average) and Earth-ACE line for both the ambient solar wind (red) and ACE-Earth connection events (blue).

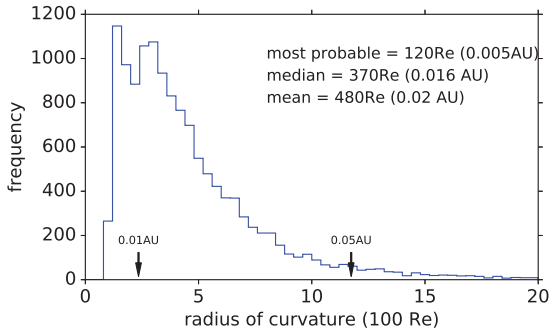

Figure 4: Frequency histogram of fitted radius, assuming magnetic field lines connect ACE and Earth through circular arcs.

To estimate the large-scale global wandering behavior of the interplanetary magnetic field (IMF), we consider an IMF aligned on the Parker spiral, but with a sinusoidally shaped perturbation that is propagating along that spiral while simultaneously being convected with the solar wind flow. The amplitude of the sinusoidal structures must be sufficiently large so that both ACE and Earth can fall on the same field line resulting in magnetic connection. Figure 5 illustrates possible geometry of sinusoidal magnetic field lines (red) connecting ACE and Earth. Wavelengths of the sine curves can be determined from magnetic field directions and spacecraft locations.

In the vicinity of Earth, including near the L1 Lagrangian point, the Parker spiral direction is given by $\vec{p} \equiv -\hat{x} + 405/|v_x|\hat{y}$, where $\hat{x}$ and $\hat{y}$ are basis vectors in GSE coordinate, and v_x is the solar wind radial velocity. The displacement vector from ACE to Earth is denoted by $\vec{d}$. To describe the sine curve conveniently, we introduce the following coordinate system. Let $\vec{n} \equiv \vec{p} \times \vec{d}$ be the normal to the plane define by $\vec{p}$ and $\vec{d}$. Define unit vecotors $\hat{n} \equiv \vec{n}/|\vec{n}|$ and $\hat{p} = \vec{p}/|\vec{p}|$, $\hat{q} \equiv \hat{n} \times \hat{p}$. Then $\hat{p}$, $\hat{q}$ and $\hat{n}$ together form a right-hand cooridinate. It is easily seen in this coordinate system that a sine curve passing through ACE and Earth, lying in a plane defined by $\vec{p}$ and $\vec{q}$, and having its axis parallel to the Parker spiral direction would take the form:

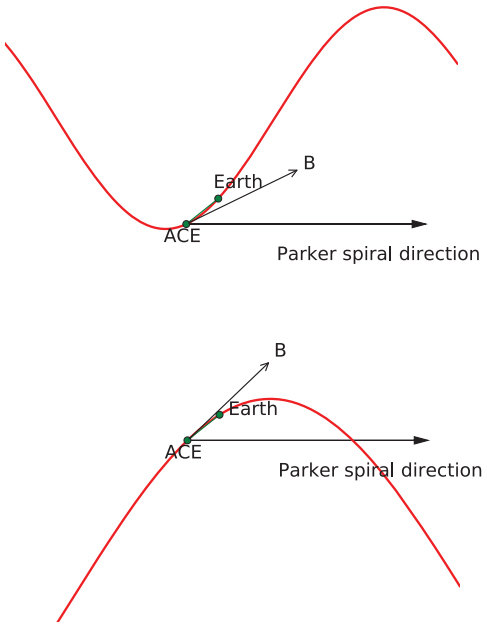

Figure 5: Two example sketches of ACE-Earth magnetic connections by large amplitude sinusoidal magnetic field lines. Different magnetic field directions and spacecraft locations correspond to different-wavelength sine waves.

$$q = A \sin\left(\frac{2\pi p}{\lambda} + \delta\right) + C \qquad (1)$$

where p and q denote displacement along $\hat{p}$ and $\hat{q}$. A denotes the amplitude of the sine wave and should be comparable to the wavelength λ. δ and C give the phase shift and the offset respectively of the sine curve. Therefore, there are four free parameters in the sine-curve: A,λ,δ, and C. The independently known or measured parameters are $\vec{d}$, $\vec{B}$ and $\vec{p}$. In the context of our simple model the known independent parameters are reduced to 3 scalars, namely d, α = cos-1($\vec{B}$ *$\vec{p}$/(|B||p|) the angle between $\vec{B}$ and $\vec{p}$, and γ=cos-1($\vec{d}$*$\vec{p}$/(|d||p||) the angle between $\vec{d}$ and $\vec{p}$. In order to solve for a length scale (λ) we eliminate one degree of freedom by fixing the amplitude as follows: $A = \lambda/\pi$. This choice of A makes the amplitude of the wave comparable to its wavelength, and effectively constrains $|\alpha|$ and $|\gamma|$ to both be $\leq \arctan 2 \sim 60°$.

Fitting a sine curve is a matter of solving the following equations:

$$0 = A\sin\delta + C \quad (2)$$

$$\tan\alpha = 2\pi A/\lambda\cos\delta \quad (3)$$

$$d\sin\gamma = A\sin(2\pi d\cos\gamma/\lambda) + C \quad (4)$$

where $d = |\vec{d}|$. Eq. (2) results from placing ACE at the origin of $p - q - n$ coordinate system, which assures that ACE lies on the sine curve. Eq. (3) expresses the requirement that the magnetic field vector at ACE is tangent to the field line. Eq. (4) utilizes the fact that the Earth is also on the field line and that its distance from ACE is d. Given α, γ and d, we can solve for the wavelength of the sine curve. In case of multiple solutions of λ, we keep the biggest wavelength, allowing us to estimate the upper bound of λ.

Note that by assuming planar sine wave in Eq. (1), we have excluded from the model plausible geometries in which the field line tilts out of the plane defined by ACE, Earth and the Parker spiral direction. Therefore, we selected data points whose $\vec{B}$ are almost in the plane by requiring that the tilt angles should be smaller than 9°, which is the angular resolution of ACE electron PAD. This reduced the data from 14335 to 5889 64s intervals. Figure 6 presents the frequency histograms of the wavelength obtained by the aforementioned fitting procedure. We find the most probable, median and mean values of λ are 1600 R_E (0.07 AU), 1700 R_E (0.07 AU) and 6400 R_E (0.27 AU).

Fitting to the ACE-Earth connection events was also performed using a hyperbolic-secant functional form representing a displacement of the magnetic-field line away from the Parker spiral: $\mathrm{sech}(p/\chi)$ instead of $\sin(2\pi p/\lambda)$. Similar λ values were obtained with the hyperbolic-secant fits as were obtained with the sine fits, which is not surprising given that χ for the hyperbolic secant is equivalent to $\lambda/4$ for a sine wave.

5. Discussion

In this section we discuss the spatial extent of the Earth's bow shock and where on the shock the observed backstreaming-electrons may originate. We include remarks on possibilities for automation of the survey of energetic-electron spacecraft measurements to find additional backstreaming events.

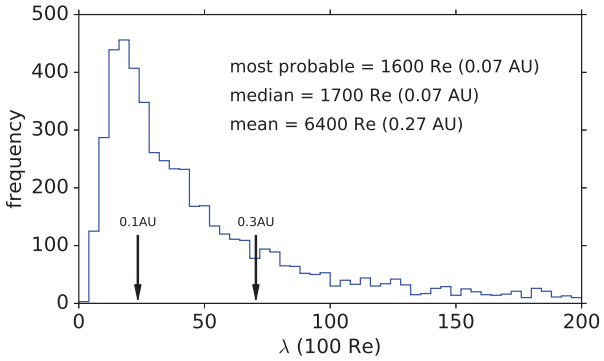

Figure 6: Frequency histogram of fitted wavelength, assuming that magnetic field lines are large sinusoidal structures flowing in the solar wind down the Parker spiral.

5.1. Bow shock consideration

To estimate the local radii of curvature and to estimate the more-global wandering lengthscales, the angle ψ between the measured magnetic field at ACE and the ACE-Earth line was used with the assumption that the magnetic-field line would bend to connect to the Earth a distance d from ACE. These calculations did not account for the fact that the bow shock is not a localized target for the field line. Examining the sketch in Figure 1, the Fairfield-Greenstadt (Fairfield, 1971; Greenstadt et al., 1990) nominal bow shock has a radius of about 25 R_E at $X = 0$ and a radius of about 120 R_E at $X = -250$ R_E. As viewed from L1 (at about 235 R_E) the $X = 0$ disk of the bow shock is about 6° in radius and the $X = -250$ R_E disk of the bow shock is about 14° in radius. (Note that at low Mach number the bow shock is broader, but weaker.) Hence, an ACE magnetic-field line with < 14° does not really need to bend to hit the bow shock, so estimates of the radii of curvature in Section 3 and estimates of the wandering lengthscales in section 4 may be underestimates.

An important question to ask is: Where on the global bow shock do the backstreaming-event electrons originate? One might speculate that regions of the bow shock that have higher compression ratios might be more likely to produce energetic foreshock electrons, with the compression ratio being an indicator of the amount of energy dissipated at the shock. In Figure 7 the measured density compression ratio of the bow shock in a global MHD simulation of the solar-wind-driven magnetosphere of Earth is plotted as a function of the GSE X location on the shock. The simulation (Joseph_Borovsky_021312_1) was run using the LFM (CMIT LFM-MIX) simulation code (Lyon et al., 2004; Merkin and Lyon, 2010) at the Community Coordinated Modeling Center (Rastätter et al., 2012). The code was run with the solar-wind flow vector coming in at an angle of 9.5° to the X axis to push the dawn-flank bow shock toward the center of the cylindrical simulation grid where the gridpoint resolution is highest. For the MA = 6.8 solar wind in the simulation, the density compression ratio (the plasma number density downstream of the shcok divided by the plasma number density upstream) of the bow shock at the nose ($X = +14.5\ R_E$) is 3.95. As seen in Figure 7, the bow-shock compression ratio drops strongly going downtail: at $X = -75\ R_E$ the compression ratio is 2.0 and $X = -200\ R_E$ the ratio is only 1.6. Certainly the production of foreshock energetic electrons will be reduced for magnetic-field lines contacting the bow shock much beyond the Earth's terminator. However, without a survey of the production of foreshock electrons from the actual bow shock, the spatial extent of the electron production region will remain unknown.

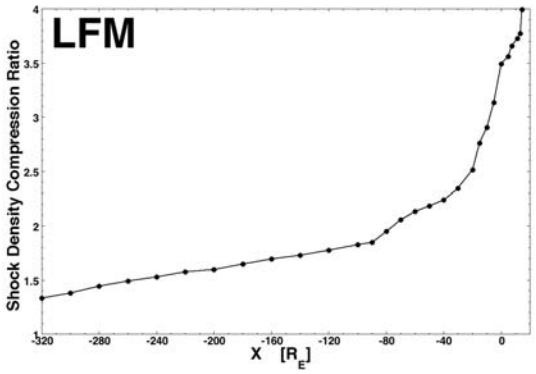

Figure 7: Density compression ratio at locations with different GSE X coordinate on Earth's bow shock in a global MHD simulation.

5.2. Automation of event selection

For this study, we selected ACE-Earth magnetic connections manually by visually searching color-coded electron pitch-angle distribution spectrograms for counterstreaming electrons. The event selection can be automated with some care. The basic characteristics of algorithm would be (1) select intervals where electron PAD flux is enhanced by say 50% at $\sim 0°$ or $\sim 180°$ and (2) verify the anisotropy of PAD in the interval selected in (1), i.e., electron flux should be smaller at intermediate pitch angles ($\sim 90°$) than at 0° and 180°. Additional conditional testing would be applied to exclude the cases where the spacecraft enters a hotter plasma. An algorithmic method to identify counterstreaming intervals was previously employed on ACE electron data in a study by (Anderson et al., 2012). It is likely that an automated algorithm could be further optimized for selecting Earth bow shock-related counterstreaming distinct from counterstreaming produced by other causes. Automated event selection would allow us to investigate ACE-Earth magnetic connection over longer time than that of 16 months in the present study. Moreover, more magnetic connection intervals would enable a study of length scales within different characteristic solar wind flow regimes.

6. Summary

We performed a study of the behaviors of solar wind magnetic field lines during 1135 solar wind ACE-Earth magnetic connection events comprising 15274 64s intervals. The quasi-local radius of curvature of the magnetic field lines was calculated, yielding values of 370-480 R_E. The quasi-global wandering scale of the magnetic field lines along the Parker spiral direction was estimated, yielding values of 0.07-0.27 AU.

References

Anderson, B.R., Skoug, R.M., Steinberg, J.T., McComas, D.J., 2012. Variability of the solar wind suprathermal electron strahl. Journal of Geophysical Research (Space Physics) 117, A04107.

Anderson, K.A., 1981. Measurements of bow shock particles far upstream from the earth. J. Geophys. Res. 86, 4445–4454.

Boldyrev, S., 2005. On the Spectrum of Magnetohydrodynamic Turbulence. ApJ 626, L37–L40. astro-ph/0503053.

Boldyrev, S., 2006. Spectrum of Magnetohydrodynamic Turbulence. Physical Review Letters 96, 115002. astro-ph/0511290.

Chollet, E.E., Giacalone, J., 2011. Evidence of Confinement of Solar-energetic Particles to Interplanetary Magnetic Field Lines. ApJ 728, 64.
Fairfield, D.H., 1971. Average and unusual locations of the Earth's magnetopause and bow shock. J. Geophys. Res. 76, 6700.
Feldman, W.C., Anderson, R.C., Asbridge, J.R., Bame, S.J., Gosling, J.T., Zwickl, R.D., 1982. Plasma electron signature of magnetic connection to the earth's bow shock - ISEE 3. J. Geophys. Res. 87, 632–642.
Giacalone, J., Jokipii, J.R., Mazur, J.E., 2000. Small-scale Gradients and Large-scale Diffusion of Charged Particles in the Heliospheric Magnetic Field. ApJ 532, L75–L78.
Goldreich, P., Sridhar, S., 1995. Toward a theory of interstellar turbulence. 2: Strong alfvenic turbulence. ApJ 438, 763–775.
Goldreich, P., Sridhar, S., 1997. Magnetohydrodynamic Turbulence Revisited. ApJ 485, 680–688. astro-ph/9612243.
Gosling, J.T., Baker, D.N., Bame, S.J., Feldman, W.C., Zwickl, R.D., Smith, E.J., 1987. Bidirectional solar wind electron heat flux events. J. Geophys. Res. 92, 8519–8535.
Gosling, J.T., Bame, S.J., Feldman, W.C., McComas, D.J., Phillips, J.L., Goldstein, B.E., 1993. Counterstreaming suprathermal electron events upstream of corotating shocks in the solar wind beyond approximately 2 AU: ULYSSES. Geophys. Res. Lett. 20, 2335–2338.
Gosling, J.T., Skoug, R.M., Feldman, W.C., 2001. Solar wind electron halo depletions at 90° pitch angle. Geophys. Res. Lett. 28, 4155–4158.
Gosling, J.T., Skoug, R.M., Feldman, W.C., McComas, D.J., 2002. Symmetric suprathermal electron depletions on closed field lines in the solar wind. Geophys. Res. Lett. 29, 14–1.
Greenstadt, E.W., Traver, D.P., Coroniti, F.V., Smith, E.J., Slavin, J.A., 1990. Observations of the flank of earth's bow shock to 110 re by isee 3/ice. Geophysical Research Letters 17, 753–756.
Haggerty, D.K., Roelof, E.C., Smith, C.W., Ness, N.F., Tokar, R.L., Skoug, R.M., 2000. Interplanetary magnetic field connection to the L1 Lagrangian orbit during upstream energetic ion events. J. Geophys. Res. 105, 25123–25132.
Jian, L., Russell, C.T., Luhmann, J.G., Skoug, R.M., 2006. Properties of interplanetary coronal mass ejections at one au during 1995 – 2004. Solar Physics 239, 393–436.
Jian, L.K., Russell, C.T., Luhmann, J.G., MacNeice, P.J., Odstrcil, D., Riley, P., Linker, J.A., Skoug, R.M., Steinberg, J.T., 2011. Comparison of Observations at ACE and Ulysses with Enlil Model Results: Stream Interaction Regions During Carrington Rotations 2016 - 2018. Sol. Phys. 273, 179–203.
Jokipii, J.R., Parker, E.N., 1969. Stochastic Aspects of Magnetic Lines of Force with Application to Cosmic-Ray Propagation. ApJ 155, 777.
Kaghashvili, E.K., Zank, G.P., Webb, G.M., 2006. Propagation of Energetic Charged Particles in the Solar Wind: Effects of Intermittency in the Medium. ApJ 636, 1145–1150.
Kahler, S., Ragot, B.R., 2006. Near-relativistic Electron c/v Onset Plots. ApJ 646, 634–641.
Kasper, J.C., . Cfa interplanetary shock database.
Kóta, J., Jokipii, J.R., 2000. Velocity Correlation and the Spatial Diffusion Coefficients of Cosmic Rays: Compound Diffusion. ApJ 531, 1067–1070.
Lithwick, Y., Goldreich, P., Sridhar, S., 2007. Imbalanced Strong MHD Turbulence. ApJ 655, 269–274. astro-ph/0607243.
Lyon, J.G., Fedder, J.A., Mobarry, C.M., 2004. The Lyon-Fedder-Mobarry (LFM) global MHD magnetospheric simulation code. Journal of Atmospheric and Solar-Terrestrial Physics 66, 1333–1350.
Matthaeus, W.H., Goldstein, M.L., Roberts, D.A., 1990. Evidence for the presence of quasi-two-dimensional nearly incompressible fluctuations in the solar wind. J. Geophys. Res. 95, 20673–20683.
Mazur, J.E., Mason, G.M., Dwyer, J.R., Giacalone, J., Jokipii, J.R., Stone, E.C., 2000. Interplanetary Magnetic Field Line Mixing Deduced from Impulsive Solar Flare Particles. ApJ 532, L79–L82.
McComas, D.J., Bame, S.J., Barker, P., Feldman, W.C., Phillips, J.L., Riley, P., Griffee, J.W., 1998. Solar Wind Electron Proton Alpha Monitor (SWEPAM) for the Advanced Composition Explorer. Space Sci. Rev. 86, 563–612.
Merkin, V.G., Lyon, J.G., 2010. Effects of the low-latitude ionospheric boundary condition on the global magnetosphere. Journal of Geophysical Research (Space Physics) 115, A10202.
Mitchell, D.G., Roelof, E.C., Sanderson, T.R., Reinhard, R., Wenzel, K.P., 1983. ISEE/IMP observations of simultaneous upstream ion events. J. Geophys. Res. 88, 5635–5644.
Perez, J.C., Boldyrev, S., 2010. Strong magnetohydrodynamic turbulence with cross helicity. Physics of Plasmas 17, 055903–055903. 1004.3798.
Pommois, P., Veltri, P., Zimbardo, G., 2001. Field line diffusion in solar wind magnetic turbulence and energetic particle propagation across heliographic latitudes. J. Geophys. Res. 106, 24965–24978.
Pommois, P., Veltri, P., Zimbardo, G., 2002. Diffusive and anomalous magnetic field lines transport in anisotropic turbulence. Fractals 10, 313–319. http://www.worldscientific.com/doi/pdf/10.1142/S0218348X0200121X.
Ragot, B.R., 2006. Lengths of Wandering Magnetic Field Lines in the Turbulent Solar Wind. ApJ 653, 1493–1498.
Ragot, B.R., 2010. Nonlinear Simulation of Turbulent Field Lines: Dispersal Statistics. ApJ 723, 1787–1798.
Ragot, B.R., 2011. Statistics of Field-line Dispersal: Random-walk Characterization and Supradiffusive Regime. ApJ 728, 50.
Rastätter, L., Kuznetsova, M.M., Sibeck, D.G., Berrios, D.H., 2012. Scientific visualization to study Flux Transfer Events at the Community Coordinated Modeling Center. Advances in Space Research 49, 1623–1632.
Reames, D.V., Stone, R.G., 1986. The identification of solar He-3-rich events and the study of particle acceleration at the sun. ApJ 308, 902–911.
Richardson, I.G., Cane, H.V., 2010. Near-Earth Interplanetary Coronal Mass Ejections During Solar Cycle 23 (1996 - 2009): Catalog and Summary of Properties. Sol. Phys. 264, 189–237.
Ruffolo, D., Chuychai, P., Wongpan, P., Minnie, J., Bieber, J.W., Matthaeus, W.H., 2008. Perpendicular Transport of Energetic Charged Particles in Nonaxisymmetric Two-Component Magnetic Turbulence. ApJ 686, 1231–1244.
Scholer, M., Ipavich, F.M., Gloeckler, G., Hovestadt, D., Klecker, B., 1980. Upstream particle events close to the bow shock and 200 re upstream: Isee-1 and isee-3 observations. Geophys. Res. Lett. 7, 73–76.
Skoug, R.M., Gosling, J.T., McComas, D.J., Smith, C.W., Hu, Q., 2006. Suprathermal electron 90° pitch angle depletions at reverse shocks in the solar wind. Journal of Geophysical Research (Space Physics) 111, A01101.
Stansberry, J.A., Gosling, J.T., Thomsen, M.F., Bame, S.J., Smith, E.J., 1988. Interplanetary magnetic field orientations associated with bidirectional electron heat fluxes detected at ISEE 3. J. Geophys. Res. 93, 1975–1980.

Steinberg, J.T., Gosling, J.T., Skoug, R.M., Wiens, R.C., 2005. Suprathermal electrons in high-speed streams from coronal holes: Counterstreaming on open field lines at 1 AU. Journal of Geophysical Research (Space Physics) 110, A06103.

Trenchi, L., Bruno, R., Telloni, D., D'amicis, R., Marcucci, M.F., Zurbuchen, T.H., Weberg, M., 2013. Solar Energetic Particle Modulations Associated with Coherent Magnetic Structures. ApJ 770, 11.

Webb, G.M., Zank, G.P., Kaghashvili, E.K., le Roux, J.A., 2006. Compound and perpendicular diffusion of cosmic rays and random walk of the field lines. i. parallel particle transport models. The Astrophysical Journal 651, 211.

Weinhorst, B., Shalchi, A., 2010a. Influence of spectral anisotropy on the random walk of magnetic field lines. MNRAS 406, 634–643.

Weinhorst, B., Shalchi, A., 2010b. Reproducing spacecraft measurements of magnetic correlations in the solar wind. MNRAS 403, 287–294.

Zimbardo, G., Pommois, P., Veltri, P., 2004. Magnetic flux tube evolution in solar wind anisotropic magnetic turbulence. Journal of Geophysical Research (Space Physics) 109, A02113.

Zimbardo, G., Pommois, P., Veltri, P., 2008. Visualizing Particle Transport Across Magnetic Flux Tubes in Anisotropic Magnetic Turbulence. IEEE Transactions on Plasma Science 36, 1114–1115.

Substorm Occurrence Rates as Determined by Various Data Sets

Kateryna Yakymenko

Department of Physics and Engineering Physics, University of Saskatchewan, Saskatoon, Saskatchewan

Joseph E. Borovsky

[a] *Space Science Institute. Boulder, Colorado*
[b] *CSSE, University of Michigan, Ann Arbor, Michigan*

Abstract

A comprehensive study of the occurrence rate of magnetospheric substorms is performed using five sets of events: 16765 geosynchronous electron injection events, 6732 spacecraft optical auroral events, 18804 jumps in the SML (SuperMag Lower) index, 57695 SOPHIE (Substorm Onsets and Phases from Indicies of the Electrojet) events, and 121541 MPB (Midlatitude Positive Bay) events. The different data sets yield different types of events: SML events, injection events, and optical events are substorm onsets whereas MPB events and SOPHIE events are predominantly substorm activations. The substorm occurrence rate was investigated versus the type of solar-wind plasma passing the Earth, versus the level of geomagnetic activity, versus the solar wind speed, and with time through three solar cycles. The recurrence rate distribution of substorms differs in the various types of plasma: periodic substorms occur predominantly in coronal-hole plasma and in ejecta. Substorm occurrence rates were studied in 70 high-speed-stream-driven storms: the rate is anomalously low in the calms before the storms, the rate increases rapidly at storm onset, and the rate is sustained at high levels for days through the high speed streams and into the trailing edges. Substorm occurrence rates were studied in 47 CME-sheath-driven storms wherein the rate jumps up as the interplanetary shock passes the Earth and is sustained into the sheath. The passage of an interplanetary shock does not itself produce a substorm.

Keywords: substorms, magnetic storms, geomagnetic indices, electron injections

1. Introduction

A substorm is an interval wherein magnetic energy that has built up in the Earth's magnetotail is released (McPherron et al., 1973; McPherron, 2016). The stored energy accumulates during an interval of enhanced coupling of the solar wind to the magnetosphere. The substorm is manifested by strong Earthward flow in the magnetotail (Birn et al., 1996), by auroral intensifications (Akasofu, 1964), by dipolarization of the near-Earth magnetotail (Nagai, 2013), by injection of energetic electrons and energetic protons into the dipolar magnetosphere (Konradi, 1967), and by Pi-2 pulsations (Rostoker and Olson, 1979). In temporally isolated substorms three distinct temporal phases can be identified (cf. Weimer, 1994): a growth phase, an expansion phase with a distinct expansion-phase onset, and a recovery phase. Often a substorm undergoes enhancements or activations after the initial expansion-phase onset (Kisabeth and Rostoker, 1974; Rostoker, 1996).

Substorms and substorm occurrence rates are important to understand. A substorm results in a morphological transition of the magnetosphere, changing the magnetic-field configuration of the near-Earth magnetotail and ejecting a portion of the magnetotail and its plasma downtail (Hones, 1977). A substorm produces a substantial energy transfer from the magnetotail to the ionosphere (Baumjohann and Kamide, 1984) and to magnetospheric plasma populations (Baumjohann et al., 1991). Substorm occurrence is important for the evolution of the outer electron radiation belt: (1) substorm-injected electrons are probably the seed population for the radiation belt (Summers et al., 1998; Friedel

Email addresses: kay431@usask.mail.ca (Kateryna Yakymenko), jborovsky@SpaceScience.org (Joseph E. Borovsky)

et al., 2002), (2) plasma waves in the dipolar magnetosphere that are driven by the injected-particle populations may resonantly energize radiation-belt electrons to relativistic energies (Meredith et al., 2001; He et al., 2014), and (3) the induction electric fields of repeated substorms may directly energize radiation-belt electrons as the electrons drift across the nightside of the dipole during substorm expansion phases (Kim et al., 2000; Fok et al., 2001; Dai et al., 2014). Under special circumstances substorms can also directly produce MeV electrons and protons (Ingraham et al., 2001; Borovsky et al., 2016). Substorm injections may also produce ULF waves in the dipolar magnetosphere (Southwood, 1976; Anderson et al., 1990; Zolotukhina et al., 2008), and substorm injections have been suspected to produce outward transport of the plasmasphere (Spiro et al., 1981; Borovsky et al., 2014). Periodically occurring substorms represent a distinct mode of operation of the solar-wind-driven magnetosphere-ionosphere system and there is undoubtedly a relationship between periodic substorms and global sawtooth oscillations of the magnetosphere (Borovsky, 2004; Noah and Burke, 2013).

Studies of the substorm occurrence rate (number of substorms per day) are quite limited (Borovsky et al., 1993; Borovsky and Nemzek, 1994; Lee and Min, 2002; Tanskanen et al., 2005, 2011; Tanskanen, 2009; Wang and Lhr, 2007; Guo et al., 2014). Substorms are known to be associated with intervals of southward IMF (Fairfield and Cahill Jr, 1966; Morley and Freeman, 2007; Newell and Liou, 2011). But in general the substorm occurrence rate is not well known, particularly the rate versus the strength of the solar-wind driving, the rate versus the type of solar-wind plasma, the rate through the phases of the solar cycle, or the rate in the different phases of geomagnetic storms.

Substorms are known to occur in two fashions, randomly in time during intervals of weak solar-wind driving and periodically in time during intervals of stronger solar-wind driving (Borovsky et al., 1993; Belian et al., 2013; Prichard et al., 1996). The recurrence period of substorms has been found to be invariant to the driving strength of the solar wind (Belian et al., 1994). Indeed the origin of the $\sim$ 3-hour periodicity of the magnetosphere is an outstanding question in magnetospheric physics (Belian et al., 1994; Borovsky, 2004; Freeman and Morley, 2004; Cai and Clauer, 2009; Brambles et al., 2013; Ouellette et al., 2013; Welling et al., 2015).

In this report we investigate the occurrence rates of substorms. Four distinct data sets are used to determine the onset times of substorms: the SML index, the MPB index, geosynchronous energetic-electron measurements, and optical auroral observations. Five different methodologies are employed in the four data sets to identify substorm-onset times. Analysis of the events from the various data sets will find that the different data sets and different selection methods yield different types of events. This relates to the historical dilemma arising from the lack of a universal definition of a substorm: the definition is unsettled both as to the defining signatures of a substorm (e.g., Akasofu, 1968, 1979; Rostoker et al., 1980) and as to the critical amplitude of the event (e.g., Kamide, 1993; Rostoker, 1993). In the four data sets some methods find onsets at the beginnings of expansion phases and some methods find activations during ongoing substorms.

2. Data Sets and Event Selection

For this study we created 3 lists of substorm onsets from ground-based magnetic data from both the auroral oval and the midlatitude regions. The forth list of substorms examined in this paper is based on another ionospheric manifestation of a substorm – auroral breakup – the sudden brightening and poleward expansion of the aurora near midnight. Finally, specific morphological changes in particle characteristics at geosynchronous orbit allow us to create a fifth list of substorm onsets. The first list of substorm onsets from the SML index was obtained with the use of the SOPHIE algorithm proposed recently by Forsyth et al. (2015). 97, 123 events were identified by the SOPHIE-80% algorithm for the period from January 1981 to December 2015.

For the second list of events we used a scheme that locates regions where the SML index decreases by at least 200 nT in 15 mins, then locates potential onset times within those time intervals where the 3-min change of SML decreases by more than 40 nT (which is a slope of more than -200 nT in 15 min). Then, for each potential onset time, the time integral of the magnitude of the SML index for the 45 mins after the onset time is compared with the time integral of the magnitude of the SML index for the 45 mins prior to the onset time: if the "after" integral is less than 1.5 times the "before" integral, that onset time is rejected as not representing the onset of a substantial change in geomagnetic activity. The first surviving onset time in each interval where SML decreases by 200 nT or more in 15 mins is taken to be the onset of the substorm. Finally, if a 200 nT-in-15 min interval occurs within 15 min of a prior 200 nT-in-15 min interval, the second interval is voided and the onset time in that second interval is not used. In this robust-event scheme, the minimum time between substorm onsets in the 1981 – 2015 SML data set is 37 mins. Total number of

18, 804 events was selected by the algorithm covering interval from 1981 to 2016.

To create the third list of substorm onsets we used so-called midlatitude positive bay (MPB) index developed by Chu et al. (2015). Magnetic field measurements from 41 midlatitude stations in both hemispheres were used to create a database of the MPB index covering 31 years of observations (from 1982 to 2012). We used the database to create a list of "positive bay" events that are believed to be signatures of substorms. To identify a positive bay event from the data we used the threshold of 25 nT^2 proposed by Chu et al. (2015) and for the onset time, we used time of the maximum of the second derivative of the MPB index. The data was initially smoothed to eliminate high-frequency oscillations in the same way that the SML index was smoothed in the SOPHIE algorithm. Unlike Chu et al. (2015), we did not restrict our database to isolated events only; our aim was to examine the whole set of positive bay events. We also did not exclude any near events in favour of others and did not use any criteria other than the 25 nT^2 threshold rule. As a result, we obtained a very large database of 121, 541 events (in comparison, the list of isolated events by Chu et al. (2015) consists of 40, 562 events).

The optical substorm onset database used in this study consists of two well-known lists: the IMAGE list (Frey et al., 2004; Frey and Mende, 2006) and the Polar list (Liou, 2010). Both lists are based on global auroral observations from satellites. The Polar list covers observations between 1996 and 2000 with total number of 2003 auroral substorms identified during this period. The list is extended by an additional 536 events of auroral substorms identified in the Southern Hemisphere in 2007. The IMAGE database covers events from 2000 to 2006, resulting in 4193 auroral breakups that occurred in the Northern and Southern Hemisphere.

The injection of energetic electrons into geosynchronous orbit is temporally associated with the onset of a substorm. An automated method to identify substorm electron injections into geosynchronous orbit was developed based on the observation that the specific entropy $S = T/n^{2/3}$ (cf. Borovsky and Cayton, 2011) of the hot-electron population at geosynchronous orbit decreases significantly when a fresh injection of electrons occurs. Multispacecraft measurements of energetic electrons from the SOPA (Synchronous Orbit Particle Analyzer) instruments in geosynchronous orbit are used to determine the specific entropy of the substorm-injected electron population.

An example of SML and MPB data for one day of observations on 15 July 2007 and the results of the event selection for this day are shown in Figure 1. Geomagnetic activity changed throughout the day from active ($Kp = 4+$) at the beginning of the day to low ($Kp = 1+$) by the end of the day and thus the event demonstrates how indices vary for quiet and moderately disturbed conditions. Dashed lines in the Figure 1 indicate 5 types of events: green lines are SOPHIE events, purple lines are the "200-nT-in-15-mins" events (subsequently the events will be referred to as simply "SML events"), brown lines are Polar onsets, blue lines are MPB events, and pink bands represent the time intervals of the injection events. 9 MPB events, 7 SOPHIE events, 2 SML events, 4 Polar events, and 4 injection events were identified for the day.

3. Results

In Figure 2 the distribution of recurrence times (waiting times) of substorms is plotted for four sets of events: MPB events (blue curve), SOPHIE events (green curve), SML events (purple curve), and injection events (pink curve). The recurrence time t is defined as the time interval between the occurrence of subsequent substorm onsets. Note that the recurrence-time distributions of MPB events and SOPHIE events are very different from the recurrence-time distributions of SML events and injection events. Finer-resolution binning of the t values finds that the recurrence-time distributions of MPB and SOPHIE events both peak at about 45 min whereas the recurrence-time distributions of SML and injection events both peak at about 3 hr. Clearly, MPB events and SOPHIE events are different events from SML events and injection events. An interpretation used in this study is that (1) SML events and injection events are substorm onsets (where a substorm onset is the beginning of an interval of enhanced geomagnetic activity) and (2) MPB and SOPHIE events are dominantly substorm intensifications. In Table 1 the minimum t value and median t value for the distributions of Figure 2 are listed.

We performed extensive statistical analysis of substorm occurrence rates for different geomagnetic conditions, different phases of solar cycle and different upstream solar wind conditions. One of the results is shown in Figure 3; the substorm occurrence rate (number of substorms per day) versus the type of solar-wind plasma is plotted for the four collections of substorm events. The left panel of Figure 3 depicts the occurrence rate as determined with SOPHIE events (green) and MPB events (blue) and the right panel of Figure 3 depicts the occurrence rate as determined with SML events (purple) and injection events (pink). In the left panel of Figure 3 it is seen that the occurrence rate of

SOPHIE and MPB events is much higher in ejecta and in coronal-hole solar wind than it is in sector-reversal and streamer-belt solar wind.

In Figure 4 the solar wind driving of the Earth's magnetosphere is examined around the time of substorm onset using superposed epoch analysis of the 1-min-resolution OMNI2 solar wind data set. In the left panel of Figure 4 the superposed median of the reconnection function R_{quick} (Borovsky, 2014) is plotted; the median value of R_{quick} in the full OMNI2 data set is indicated by the horizontal black dashed line in the left panel. The superposed median of R_{quick} shows a peak for each of the five sets of event triggers: for MPB events (blue) and SML (purple) events the peak in the superposed median is near the time of onset and for injection events (pink), MPB events (blue), and optical events (yellow) the peak in the superposed median is prior to the time of onset. Newell and Liou (2011) have an extensive analysis of the reason why this driver function and others have maxima in the superposed averages about 20 min prior to substorm onset; their conclusion is that the requirement for above-average strengths of solar-wind driving prior to substorm onset leads to a peak prior to onset that is offset by a time corresponding to the sum of the solar-wind advection time through the magnetosheath to the nose of the magnetosphere and the internal reaction time of the magnetosphere to dayside reconnection [see also Bargatze et al. (1985)]. In Figure 4 the peak in the superposed median of R_{quick} is earlier than this 20 min for the injection events (pink), which is expected since the method of determining substorm injection onsets with the SOPA electron entropy uses half-hour resolution measurements of the specific entropy and these electrons may require some time to drift from the nightside to an operating geosynchronous spacecraft (i.e. the injection triggers are delayed). For SOPHIE events (green) and SML events (purple) the peak of the superposed median of R_{quick} is very near to the time of substorm onset, and for MPB events (blue) the peak is about 10min prior to onset; the reason for the peaks in the superposed medians near the time of onset is not known. The SOPHIE events also show a secondary maximum at about 40 mins prior to onset.

Substorm occurrence during high-speed-stream(HSS)-driven storms is believed to be an important factor for providing a seed population of electrons for the radiation belt and for driving plasma waves that energize radiation-belt electrons. The occurrence rate of substorm during HSS-driven storms is studied here with a collection of 70 storms in the years 1993-2005. In the two panels of Figure 5 the superposed probability density of the SML and MPB indices is plotted for 70 HSS-driven storms. Dark blue lines are the median values of the indices, the horizontal axis is time in days since zero epoch, insertions are enlarged plots for 5-hr window. About two days before storm onset, the probability of the small-magnitude values of SML and MPB indices increases noticeably (the calm before storm). A few hours before zero epoch time the magnitudes of the indices increase steadily reaching maximum values at about storm onset time. The magnitude of the indices stays elevated for four or more days after storm onset. During this time, the probability density is almost uniform throughout whole spectrum of values indicating significant variations in the values of the indices.

To study the substorm occurrence rate in CME-sheath-driven geomagnetic storms, a collection of 47 shock-sheath intervals is created. Superposed epoch analysis of substorm occurrence rates centered on the time of arrival of the shock at Earth (not shown here) shows that substorm occurrence rate increases immediately upon arrival of the shock. We argue, however, that more time needs to pass since the shock's initial arrival to produce substorm. The changes in the indices most probably are caused by a compression of the magnetosphere. We investigated this question deeper by looking at the reaction of the energetic-particle population at geosynchronous orbit.

In Figure 6 superposed electron fluxes from the three lowest energy channels of the LANL SOPA instrument are centered on the time of the shock arrival at Earth (panels (a) and (b)) and on the occurrence times of SML events (panels (c) and (d)). We considered separately changes in the fluxes as detected by satellites located at the time of an event in the midnight-to-dawn (23 to 5 LT) and in the noon-to-dusk (10 to 20 LT) sectors. When reaction of the fluxes in the noon LT sector was analysed, care was taken to exclude times when geosynchronous satellites left magnetosphere and entered the magnetosheath as determined by examining plasma data from the same spacecraft. Considered SML events span time interval from September 1989 to September 1993. Note the differences between reaction of the fluxes on the shock at Earth and SML events. First of all, as seen from Figure 6 (panels (a) and (b)), changes in the fluxes triggered on the shock happen simultaneously in both LT sectors. For SML substorm events, in contrast, fluxes begin to rise at the zero epoch time in the midnight-to-dawn LT sector (Figure 6 (c) and show up to 30 min delay in the noon-to-dusk LT sector. This is expected as substorm-associated electron injections occur close to the midnight sector and then electrons drift eastward, so satellites located in the noon-to-dusk sector will detect changes in fluxes later in time than satellites in the midnight-to-dawn sector. Another important difference is that changes in fluxes associated with the SML events happen nearly simultaneously when observed with satellites in the midnight-to-dawn

sector (panel (c)) and electron fluxes show dispersion when observed in the noon-to-dusk sector. This is expected as lower-energy electrons have lower drift velocities and require more time for then to drift away from the injection region. Increases of electron fluxes centered on the shock at Earth events, on the other hand, are dispersionless in both LT sectors. Note also that jumps of fluxes at the time of the shock at Earth are more sharp than jumps of fluxes at the time of SML events. All these observations support the argument that changes in the SML and MPB index at time of the shock at Earth are not caused by the occurrence of a substorm.

4. Conclusion

A comprehensive study of the occurrence rate of substorms was performed using five sets of substorm onsets: (a) 121541 MPB events in 1982-2012, (b) 57695 SOPHIE events in 1981-2015, (c) 18804 SML events in 1981-2015, (d) 16765 injection events in 1989-2007, and (e) 6732 optical events in 1996-2007.

1. Four algorithms for determining the onset times of substorms in the SML index, the MPB index, and the geosynchronous-orbit energetic-electron data set were explored and refined.
2. Analysis of event-recurrence times (waiting times) indicates that SML events and injection events are onsets of substorm (i.e. they are the sudden beginning of an interval of enhanced geomagnetic activity and the sudden appearance of a fresh energetic-particle population at geosynchronous orbit) and that the MPB events and SOPHIE events are dominated by substorm activations.
3. Commensurate with the above interpretation, the average occurrence rate of the four types of events are 10.7 per day for MPB events, 7.6 per day for SOPHIE events, 2.7 per day for injection events, and 1.3 per day for SML events.
4. The event recurrence time distributions show a peak at about three hours for SML events and for injection events, commensurate with the $\sim$ 3-hour periodicity of substorm occurrence. The recurrence time distributions for MPB events and SOPHIE events peak at about 45 min.
5. The substorm occurrence rates are highest during the declining phase of the solar cycle and the occurrence rates where very low during the weak solar wind of the most-recent solar minimum.
6. Superposed epoch analysis of the solar wind triggered on the time of substorm onset shows a peak in the superposed average of the solar wind driving just before onset.
7. Categorizing the type of solar wind plasma at Earth at the time of substorm occurrence, the substorm occurrence rate is found to be highest in coronal-hole-origin plasma, second highest in eject, lower in streamer-belt plasma, and lowest in sector-reversal-region plasma.
8. The distribution of substorm recurrence times differs in the four categories of solar-wind plasma: periodic substorms occur predominantly in coronal-hole-origin plasma and in ejecta.
9. The substorm occurrence rate is higher on average when geomagnetic activity (as measured by the Kp index) is higher.
10. Relatedly, the substorm occurrence rate is higher on average when the solar wind velocity is higher.
11. The substorm occurrence rate was studied during 70 high-speed stream-driven storms: it was found that the occurrence rate is anomalously low in the calms before the storms, it suddenly increases to a high rate at storm onset, and the occurrence rate stays high well into the trailing edge of the high-speed stream where the solar-wind velocity is declining but the electron-radiation belt is still intensifying.
12. The substorm occurrence rate was studied during 47 CME-sheath-driven storms: occurrence rates in CME-sheath storms are at a similar level as they are in high-speed-stream-driven storms.
13. Although the algorithms for fining substorm-onset times trigger when an interplanetary shock passes the Earth, analysis indicates that the triggering is caused by compression of the magnetosphere rather than by the actual occurrence of a substorm.

References

Akasofu, S.I., 1964. The development of the auroral substorm. Planet. Space Sci. 12, 273–282.

Akasofu, S.I., 1968. Auroral observations by the constant local time flight. Planet. Space Sci. 16, 1365 – 1368.

Akasofu, S.I., 1979. Dynamics of the Magnetosphere. chapter What is a magnetospheric substorm? p. 447.

Anderson, B.J., Engebretson, M.J., Rounds, S.P., Zanetti, L.J., Potemra, T.A., 1990. A statistical study of Pc 35 pulsations observed by the AMPTE/CCE Magnetic Fields Experiment, 1. Occurrence distributions. J. Geophys. Res. 95, 10495–10523.

Bargatze, L.F., Baker, D.N., McPherron, R.L., Hones, E.W., 1985. Magnetospheric impulse response for many levels of geomagnetic activity. J. Geophys. Res. 90, 6387–6394.

Baumjohann, W., Kamide, Y., 1984. Hemispherical Joule heating and the AE indices. J. Geophys. Res. 89, 383–388.

Baumjohann, W., Paschmann, G., Nagai, T., Lhr, H., 1991. Superposed epoch analysis of the substorm plasma sheet. J. Geophys. Res. 96, 11605–11608.

Belian, R.D., Borovsky, J.E., Nemzek, R.J., W., S.C., 1994. Random and periodic substorms and their origins in the solar wind, in: Proceedings of the Second International Conference on Substorms, University of Alaska. p. 463.

Belian, R.D., Cayton, T.E., Reeves, G.D., 2013. Quasi-Periodic Global Substorm Generated Flux Variations Observed at Geosynchronous Orbit. American Geophysical Union. pp. 143–148.

Birn, J., Hesse, M., Schindler, K., 1996. MHD simulations of magnetotail dynamics. J. Geophys. Res. 101, 12939–12954.

Borovsky, J., 2004. Global sawtooth oscillations of the magnetosphere. Eos, Transactions American Geophysical Union 85, 525–525.

Borovsky, J.E., 2014. Canonical correlation analysis of the combined solar wind and geomagnetic index data sets. J. Geophys. Res. 119, 5364–5381. 2013JA019607.

Borovsky, J.E., Cayton, T.E., 2011. Entropy mapping of the outer electron radiation belt between the magnetotail and geosynchronous orbit. J. Geophys. Res. , 116A06216.

Borovsky, J.E., Cayton, T.E., Denton, M.H., Belian, R.D., Christensen, R.A., Ingraham, J.C., 2016. The proton and electron radiation belts at geosynchronous orbit: Statistics and behavior during high-speed stream-driven storms. J. Geophys. Res. 121, 5449–5488. 2016JA022520.

Borovsky, J.E., Nemzek, R.J., 1994. Substorm statistics: Occurrences and amplitudes. Technical Report.

Borovsky, J.E., Nemzek, R.J., Belian, R.D., 1993. The occurrence rate of magnetospheric-substorm onsets: Random and periodic substorms. J. Geophys. Res. 98, 3807–3813.

Borovsky, J.E., Welling, D.T., Thomsen, M.F., Denton, M.H., 2014. Long-lived plasmaspheric drainage plumes: Where does the plasma come from? J. Geophys. Res. 119, 6496–6520. 2014JA020228.

Brambles, O.J., Lotko, W., Zhang, B., Ouellette, J., Lyon, J., Wiltberger, M., 2013. The effects of ionospheric outflow on ICME and SIR driven sawtoothevents. J. Geophys. Res. 118, 6026–6041.

Cai, X., Clauer, C.R., 2009. Investigation of the period of sawtooth events. J. Geophys. Res. 114, n/a–n/a. A06201.

Chu, X., McPherron, R.L., Hsu, T.S., Angelopoulos, V., 2015. Solar cycle dependence of substorm occurrence and duration: Implications for onset. J. Geophys. Res. 120, 2808–2818. 2015JA021104.

Dai, L., Wygant, J.R., Cattell, C.A., Thaller, S., Kersten, K., Breneman, A., Tang, X., Friedel, R.H., Claudepierre, S.G., Tao, X., 2014. Evidence for injection of relativistic electrons into the Earth's outer radiation belt via intense substorm electric fields. Geophys. Res. Lett. 41, 1133–1141.

Fairfield, D.H., Cahill Jr, L.J., 1966. Transition region magnetic field and polar magnetic disturbances. J. Geophys. Res. 71, 155.

Fok, M.C., Moore, T.E., Spjeldvik, W.N., 2001. Rapid enhancement of radiation belt electron fluxes due to substorm dipolarization of the geomagnetic field. J. Geophys. Res. 106, 3873–3881.

Forsyth, C., Rae, I.J., Coxon, J.C., Freeman, M.P., Jackman, C.M., Gjerloev, J., Fazakerley, A.N., 2015. A new technique for determining Substorm Onsets and Phases from Indices of the Electrojet (SOPHIE). J. Geophys. Res. 120, 10,592–10,606. 2015JA021343.

Freeman, M.P., Morley, S.K., 2004. A minimal substorm model that explains the observed statistical distribution of times between substorms. Geophys. Res. Lett. 31, n/a–n/a. L12807.

Frey, H.U., Mende, S.B., 2006. Substorm onsets as observed by IMAGE-FUV, in: Syrjsuo, M., Donovan, E. (Eds.), Proceedings of Eighth International Substorm Conference,, Univ. of Calgary, Banff Centre, Canada. p. 7176.

Frey, H.U., Mende, S.B., Angelopoulos, V., Donovan, E.F., 2004. Substorm onset observations by IMAGE-FUV. J. Geophys. Res. 109, n/a–n/a. A10304.

Friedel, R.H.W., Reeves, G.D., Obara, T., 2002. Relativistic electron dynamics in the inner magnetosphere - a review. J. Atmos. Sol. Terr. Phys. 64, 265–282.

Guo, J., Pulkkinen, T.I., Tanskanen, E.I., Feng, X., Emery, B.A., Liu, H., Liu, C., Zhong, D., 2014. Annual variations in westward auroral electrojet and substorm occurrence rate during solar cycle 23. J. Geophys. Res. 119, 2061–2068.

He, Z., Zhu, H., Liu, S., Zong, Q., Wang, Y., Lin, R., Shi, L., Gong, J., 2014. Correlated observations and simulations on the buildup of radiation belt electron fluxes driven by substorm injections and chorus waves. Astrophys. Space Sci. 355, 245–251.

Hones, E.W., 1977. Substorm processes in the magnetotail: Comments on On hot tenuous plasmas, fireballs, and boundary layers in the Earth's magnetotail by L. A. Frank, K. L. Ackerson, and R. P. Lepping. J. Geophys. Res. 82, 5633–5640.

Ingraham, J.C., Cayton, T.E., Belian, R.D., Christensen, R.A., Friedel, R.H.W., Meier, M.M., Reeves, G.D., Tuszewski, M., 2001. Substorm injection of relativistic electrons to geosynchronous orbit during the great magnetic storm of March 24, 1991. J. Geophys. Res. 106, 25759–25776.

Kamide, Y., 1993. Key questions on magnetospheric physics and substorms. J. Atmos. Terr. Phys. 55.

Kim, H.J., Chan, A.A., Wolf, R.A., Birn, J., 2000. Can substorms produce relativistic outer belt electrons? J. Geophys. Res. 105, 7721–7735.

Kisabeth, J.L., Rostoker, G., 1974. The expansive phase of magnetospheric substorms: 1. Development of the auroral electrojets and auroral arc configuration during a substorm. J. Geophys. Res. 79, 972–984.

Konradi, A., 1967. Proton events in the magnetosphere associated with magnetic bays. J. Geophys. Res. 72, 3829–3841.

Lee, D.Y., Min, K.W., 2002. Statistical features of substorm indicators during geomagnetic storms. J. Geophys. Res. 107, SMP 16–1–SMP 16–12. 1371.

Liou, K., 2010. Polar Ultraviolet Imager observation of auroral breakup. J. Geophys. Res. 115, n/a–n/a. A12219.

McPherron, R.L., 2016. Where and when does reconnection occur in the tail? J. Geophys. Res. 121, 4607–4610. 2015JA022258.

McPherron, R.L., Russell, C.T., Aubry, M.P., 1973. Satellite studies of magnetospheric substorms on August 15, 1968: 9. Phenomenological model

for substorms. J. Geophys. Res. 78, 3131–3149.
Meredith, N.P., Horne, R.B., Anderson, R.R., 2001. Substorm dependence of chorus amplitudes: Implications for the acceleration of electrons to relativistic energies. J. Geophys. Res. 106, 13165–13178.
Morley, S.K., Freeman, M.P., 2007. On the association between northward turnings of the interplanetary magnetic field and substorm onsets. Geophys. Res. Lett. 34, n/a–n/a. L08104.
Nagai, T., 2013. An empirical model of substorm-related magnetic field variations at synchronous orbit, in: Kan, J.R., Potemra, T.A., Kokubun, S., Iijima, T. (Eds.), Magnetospheric Substorms, American Geophysical Union. pp. 91–95.
Newell, P.T., Liou, K., 2011. Solar wind driving and substorm triggering. J. Geophys. Res. 116, n/a–n/a. A03229.
Noah, M.A., Burke, W.J., 2013. Sawtooth-substorm connections: A closer look. J. Geophys. Res. 118, 5136–5148.
Ouellette, J.E., Brambles, O.J., Lyon, J.G., Lotko, W., Rogers, B.N., 2013. Properties of outflow-driven sawtooth substorms. J. Geophys. Res. 118, 3223–3232.
Prichard, D., Borovsky, J.E., Lemons, P.M., Price, C.P., 1996. Time dependence of substorm recurrence: An information-theoretic analysis. J. Geophys. Res. 101, 15359–15369.
Rostoker, G., 1993. A question of substorm size – How large must a magnetic disturbance be before it can be called a substorm. J. Geomag. Geoelectr. 45, 439.
Rostoker, G., 1996. Phenomenology and physics of magnetospheric substorms. J. Geophys. Res. 101, 12955–12973.
Rostoker, G., Akasofu, S.I., Foster, J., Greenwald, R., Kamide, Y., Kawasaki, K., Lui, A., McPherron, R., Russell, C., 1980. Magnetospheric substormsdefinition and signatures. J. Geophys. Res. 85, 1663–1668.
Rostoker, G., Olson, J.V., 1979. Pi 2 micropulsations as indicators of substorm onsets and intensifications, in: Russell, C.T. (Ed.), Auroral Processes, Japan Scientific Societies Press, Tokyo. p. 3.
Southwood, D.J., 1976. A general approach to low-frequency instability in the ring current plasma. J. Geophys. Res. 81, 3340–3348.
Spiro, R.W., Harel, M., Wolf, R.A., Reiff, P.H., 1981. Quantitative simulation of a magnetospheric substorm 3. Plasmaspheric electric fields and evolution of the plasmapause. J. Geophys. Res. 86, 2261–2272.
Summers, D., Thorne, R.M., Xiao, F., 1998. Relativistic theory of wave-particle resonant diffusion with application to electron acceleration in the magnetosphere. J. Geophys. Res. 103, 20487–20500.
Tanskanen, E.I., 2009. A comprehensive high-throughput analysis of substorms observed by IMAGE magnetometer network: Years 19932003 examined. J. Geophys. Res. 114, n/a–n/a. A05204.
Tanskanen, E.I., Pulkkinen, T.I., Viljanen, A., Mursula, K., Partamies, N., Slavin, J.A., 2011. From space weather toward space climate time scales: Substorm analysis from 1993 to 2008. J. Geophys. Res. 116, n/a–n/a. A00I34.
Tanskanen, E.I., Slavin, J.A., Fairfield, D.H., Sibeck, D.G., Gjerloev, J., Mukai, T., Ieda, A., Nagai, T., 2005. Magnetotail response to prolonged southward IMF Bz intervals: Loading, unloading, and continuous magnetospheric dissipation. J. Geophys. Res. 110, n/a–n/a. A03216.
Wang, H., Lhr, H., 2007. Seasonal-longitudinal variation of substorm occurrence frequency: Evidence for ionospheric control. Geophys. Res. Lett. 34, n/a–n/a. L07104.
Weimer, D.R., 1994. Substorm time constants. J. Geophys. Res. 99, 11005–11015.
Welling, D.T., André, M., Dandouras, I., Delcourt, D., Fazakerley, A., Fontaine, D., Foster, J., Ilie, R., Kistler, L., Lee, J.H., Liemohn, M.W., Slavin, J.A., Wang, C.P., Wiltberger, M., Yau, A., 2015. The Earth: Plasma Sources, Losses, and Transport Processes. Space Sci. Rev. 192, 145–208.
Zolotukhina, N.A., Mager, P.N., Klimushkin, D.Y., 2008. Pc5 waves generated by substorm injection: a case study. Ann. Geophys. 26, 2053–2059.

Table 1: Properties of the substorm recurrence times t for events in four different data sets.

	SOPHIE Events	MPB Events	SML Events	Injection Events
minimum t	12 min	6 min	27 min	60 min
median t	1.5 hr	0.94 hr	6.1 hr	5.0 hr
average occurrence rate	7.6 per day	10.7 per day	1.5 per day	2.7 per day

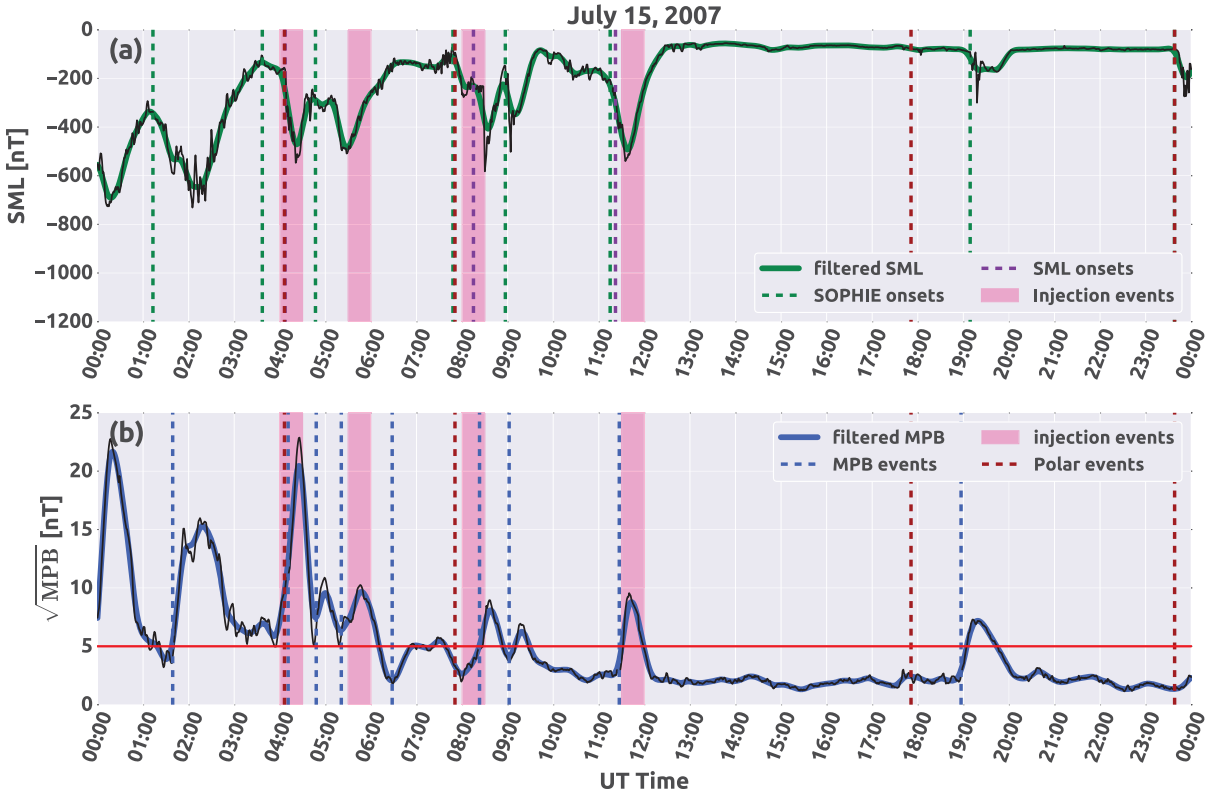

Figure 1: Example of data and event selection: (a) Variations of SML index are plotted in black, green line is filtered with 30-min low-pass filter SML index. Vertical dashed green lines are onsets identified by SOPHIE algorithm, purple vertical lines are events identified by the "200 nT in 15 min" algorithm; (b) variations of the 30-min low-pass filtered MPB index (blue line) overplotted on top of unfiltered MPB index (black line). Pink stripes show time intervals of electron injection events; yellow lines mark substorm onsets identified from Polar UVI.

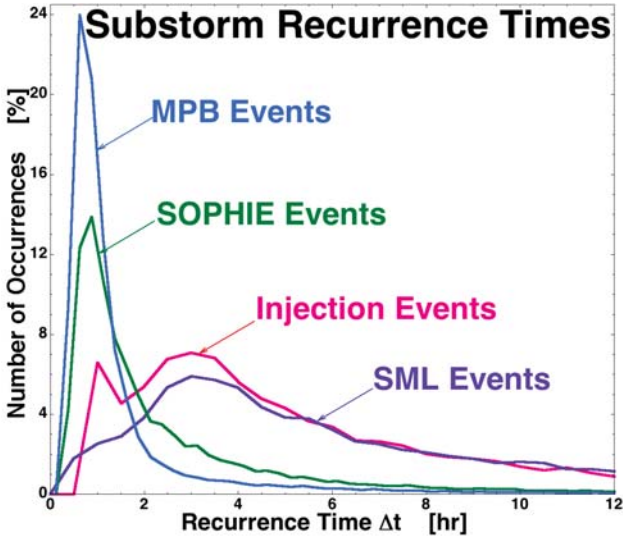

Figure 2: Substorm recurrence times t are binned for events in four different data sets. Note that the binning resolution in this plot is finer by a factor of two for the MPB events and the SOPHIE events than it is for the injection events and SML events.

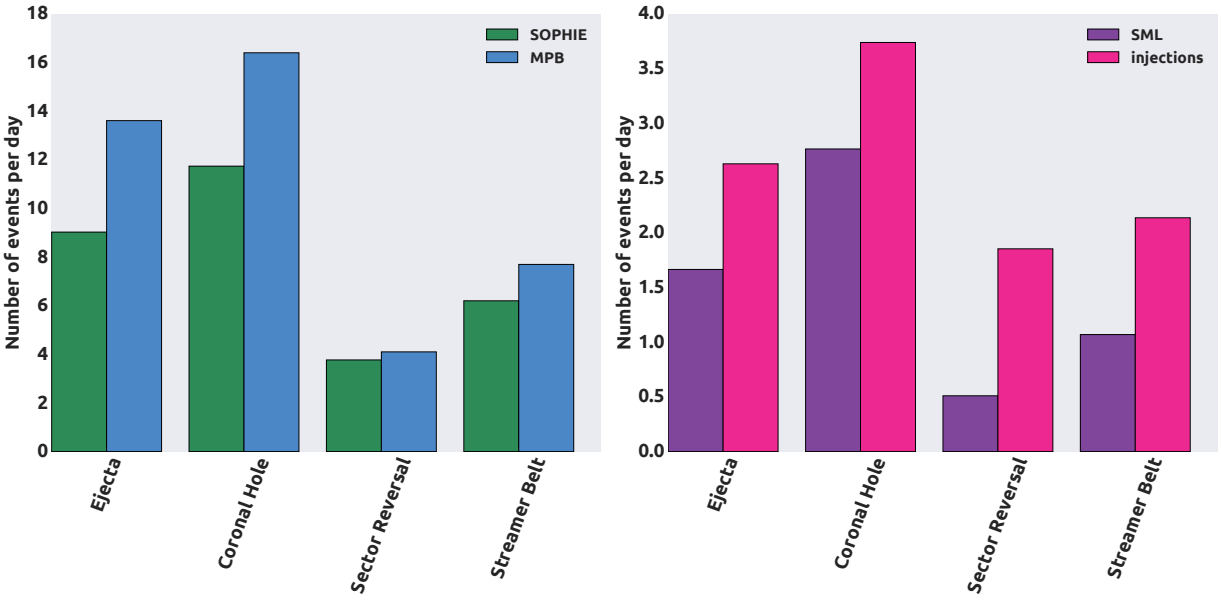

Figure 3: Occurrence of four types of events for different types of solar-wind plasma.

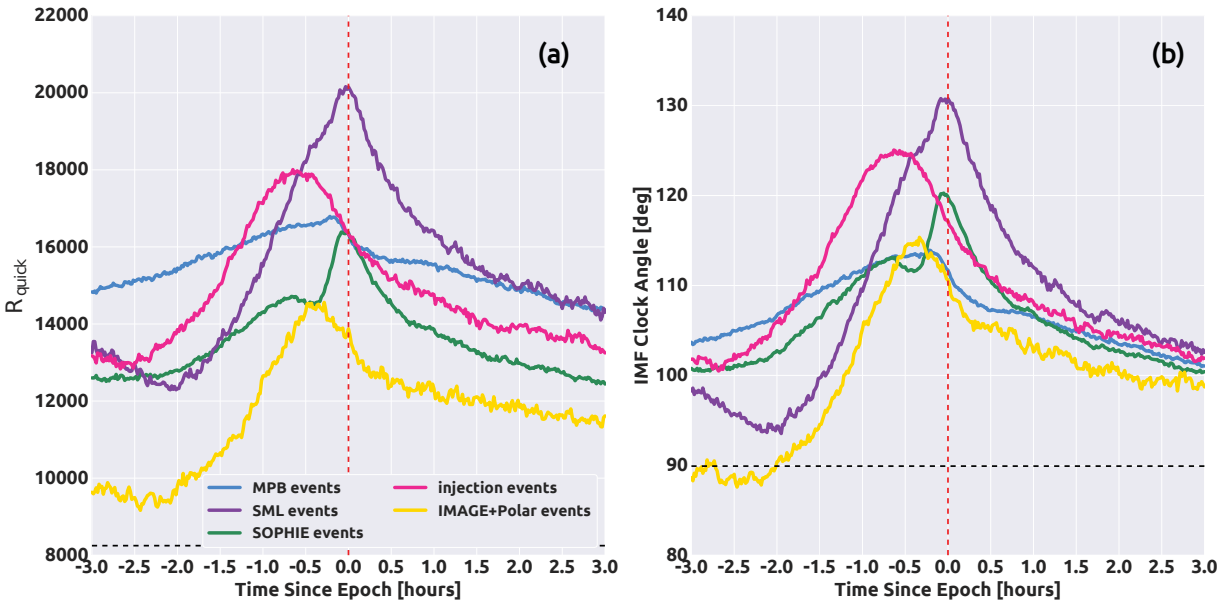

Figure 4: Superposed (a)R_{quick} centered on five collections of events (see legend) and (b) IMF clock angle centered on the same events.

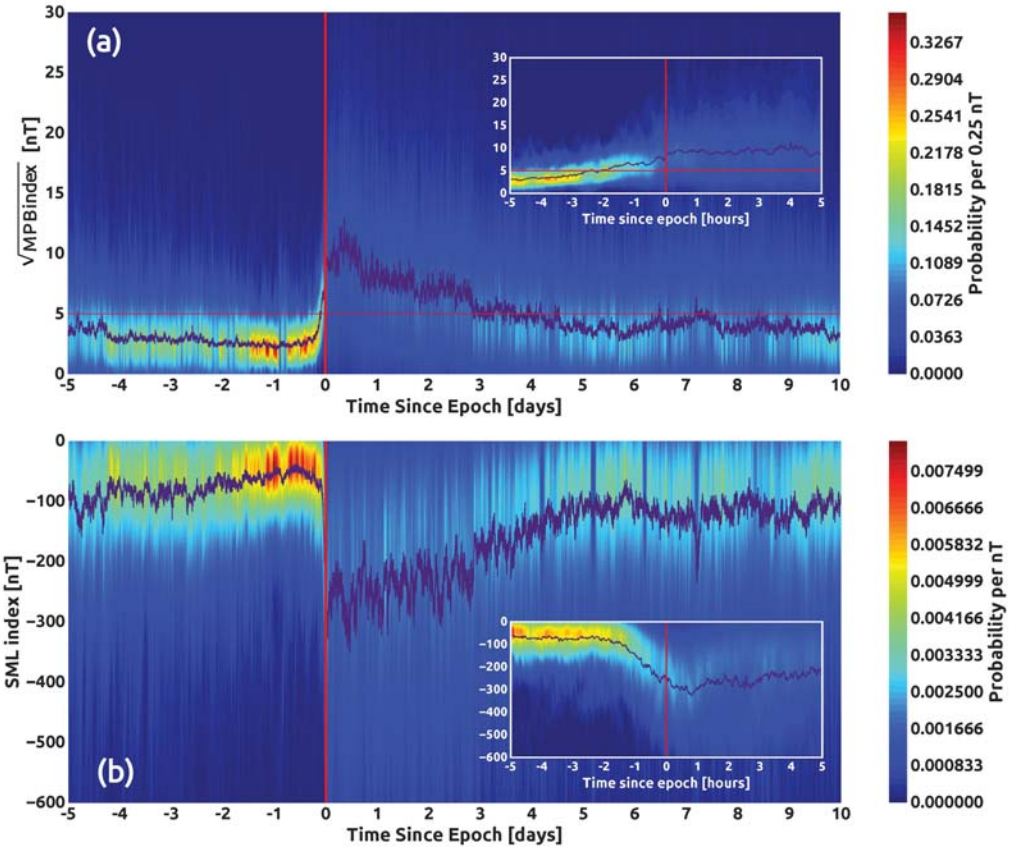

Figure 5: Superposed probability density of (a) MPB and (b) SML indices (color-coded from red at maxima to dark-blue at zero) centered on onset time of HSS-driven storms.

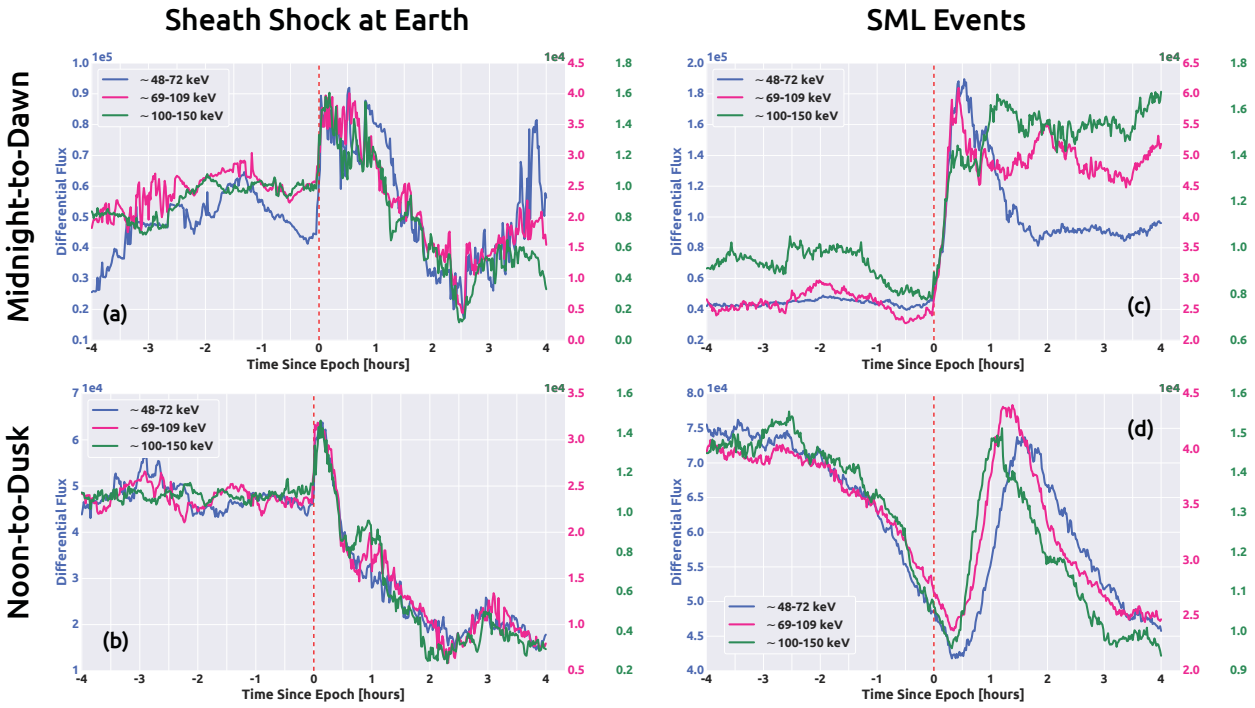

Figure 6: Superposed electron fluxes from low-energy channels (see legend) of the LANL SOPA instrument. Panels (a) and (b) correspond to the shock at Earth zero epoch time, panels (c) and (d) – to the onset time of SML events. Observations divided into "Midnight-to-Dawn" (23-5 LT sector) and "Noon-to-Dusk"(10-20 LT sector) groups depending on the position of satellite at the time of event.

Los Alamos Space Weather Summer School
30 Bikini Atoll Rd, ISR-1, MS D466
Los Alamos, NM 87545

http://swx-school.lanl.gov